Droplet Dynamics on Superhydrophobic Surfaces

Lisa Moevius
St Hugh's College



The Rudolf Peierls Centre For Theoretical Physics
University of Oxford

A thesis submitted for the degree of
Doctor of Philosophy
· Trinity Term 2013 ·

Abstract

Millions of years of evolution have led to a wealth of highly adapted functional surfaces in nature. Among the most fascinating are superhydrophobic surfaces which are highly water-repellent and shed drops very easily owing to their chemical hydrophobicity combined with micropatterning. Superhydrophobic materials have attracted a lot of attention due to their practical applications as ultra-low friction surfaces for ships and pipes, water harvesters, de-humidifiers and cooling systems. At small length scales, where surface tension dominates over gravity, these surfaces show a wealth of phenomena interesting to physicists, such as directional flow, rolling, and drop bouncing.

This thesis focuses on two examples of dynamic drop interactions with micropatterned surfaces and studies them by means of a lattice Boltzmann simulation approach. Inspired by recent experiments, we investigate the phenomenon of the self-propelled bouncing of coalescing droplets. On highly hydrophobic patterned surfaces drop coalescence can lead to an out-of-plane jump of the composite drop. We discuss the importance of energy dissipation to the jumping process and identify an anisotropy of the jumping ability with respect to surface features. We show that Gibbs' pinning is the source of this anisotropy and explain how it leads to the inhibition of coalescence-induced jumping.

The second example we study is the novel phenomenon of pancake bouncing. Conventionally, a drop falling onto a superhydrophobic surface spreads due to its inertia, retracts due to its surface tension, and bounces off the surface. Here we explain a different pathway to bouncing that has been observed in recent experiments: A drop may spread upon impact, but leave the surface whilst still in an elongated shape. This new behaviour, which occurs transiently for certain impact and surface parameters, is due to reversible liquid imbibition into the superhydrophobic substrate. We develop a theoretical model and test it on data from experiments and simulations. The theoretical model is used to explain pancake bouncing in detail.

Publications

Part of the work presented in chapters 4 and 5 has been submitted for publication or is currently being prepared for publication:

- Y. Liu, L. Moevius (shared authorship), X. Xu, T. Qian, J. Yeomans Yeomans, and Z. Wang: "Pancake bouncing on superhydrophobic surfaces", submitted
- L. Moevius and J. Yeomans: "Pancake bouncing effect on superhydrophobic surfaces in lattice Boltzmann simulations", in preparation

The work presented in chapter 3 is currently being prepared for publication:

- L. Moevius and J. Yeomans: "Effects of surface topology on coalescence-induced droplet jumping", in preparation

Acknowledgements

I would like to express my gratitude to my supervisor, Professor Julia Yeomans, for sharing her experience and providing support and guidance during the research that lead to this thesis, as well as helping me to improve my writing style.
I would also like to thank Zuankai Wang and Yahua Liu at the City University of Hong Kong for bringing pancake bouncing to my attention, collaborating on the research that led to Chapters 4 and 5, and for discussions that helped structuring Chapters 4 and 5.
I also benefited greatly from the help of Matthew Blow and Bortolo Mognetti who shared their experience with lattice Boltzmann. Rodrigo Ledesmar Aguilar's and Sumesh Thampi's advice on lattice Boltzmann and hydrodynamics was also very helpful. My understanding of various topics also benefitted from discussions with Bob Cohen, Miha Ravnik, and Mitya Pushkin. I would like to thank Marco Scigliuzzo and Andrea Cavalli for fruitful discussion on the lattice Boltzmann method.
I would like to express my gratitude to Tim Bartley, Neil Robinson, and Fenner Harper for their helpful comments on this thesis. I thank Irwin Zaid for helpful comments as well as nutritional and moral support and encouraging me to start using Python, together with Jack Cohen who took the bait of teaching me the basics. I would also like to thank Professor John Chalker and Don Grainger for giving me the opportunity to teach at St Hugh's College, and Thomas Whitehead, Elizabeth Parrott, Lee Stothert, Matthew Lowdon, Andrew Wilson, and Civaram Sivakumaran for making teaching such a pleasant experience, whereby special thanks must be directed to Lee Stothert for also encouraging me to publish my results.
I would like to thank Alison Lutton, Tim Bartley, Bridget Randolph, Marcella Orwick, Susanne Leist, and Sue Ellis for their friendship and support during these past four years, going through the ups and downs of an Oxford degree together with me.
Finally I would like to thank my family and especially Alexander DH Büchner for encouraging me to get things done.

Contents

Contents i

List of Figures v

Nomenclature vii

1 Introduction 1

1.1 Basics of the Physics of Wetting 1

1.2 Topographically Patterned Surfaces 3

1.2.1 Superhydrophobic States 5

1.2.2 Pinning and Contact Angle Hysteresis 6

1.3 Hydrodynamic Regimes 7

1.4 Droplet Impact on Surfaces 9

1.4.1 Impact Process 11

1.4.2 Drop Shape During Spreading 12

1.4.3 Superhydrophobicity for Rebound 13

1.5 Outline of the Thesis 15

2 The Lattice Boltzmann Method 17

2.1 Thermodynamics of the Binary Fluid 18

2.2 Hydrodynamics of the Binary Fluid 20

2.3 The lattice Boltzmann Algorithm 21

2.3.1 Spurious Velocities and the Multiple Relaxation Time Approach 25

2.3.2 Boundary Conditions 26
2.3.3 Energy and Dissipation in Lattice Boltzmann 26

3 Jumping Drops **29**

3.1 Self-Propelled Droplet Jumping in Experiments 29
3.1.1 Experiments by Boreyko et al. 29
3.1.2 Subsequent Studies 32
3.1.3 Motivation and Outline of the Chapter 34
3.2 Drop Coalescence: a Summary of the Literature 36
3.3 Lattice-Boltzmann Simulations 40
3.3.1 Geometry 41
3.3.2 Initial Conditions 42
3.3.3 Simulation Parameters 43
3.3.3.1 Free Coalescence 44
3.3.3.2 Comparison of Surface Geometries 44
3.3.3.3 Size Dependence 45
3.4 Free Coalescence in Two Dimensions 45
3.4.1 Viscous or Inertial Regime in Simulations 45
3.4.2 Coalescence Process 48
3.5 Coalescence on Solid Substrates 53
3.5.1 Detachment Process and Jumping Velocity 55
3.5.2 Size Dependence and Dissipation 56
3.5.3 Drop Shape at Detachment 60
3.6 Comparison of Surface Geometries 62
3.6.1 Examples 63
3.6.2 Intuitive Explanation of the Effects of Substrate Anisotropy . . . 64
3.6.3 Effect of Pinning on Coalescence-Induced Jumping 66
3.6.3.1 Local Pinning During Receding Motion 66
3.6.3.2 Global Pinning at Lift-Off 67

3.7 Discussion 68
3.8 Summary and Outlook 70

4 Pancake Bouncing **73**
4.1 Motivation 73
4.1.1 Initial Experiments 74
4.1.2 Simplified Surfaces 76
4.1.3 Experimental Observations 77
4.1.4 Summary of Experiments and Outline of the Chapter 79
4.2 Relevant Aspects of Bouncing 80
4.2.1 Contact Time 80
4.2.2 Maximum Spreading 83
4.2.3 Bouncing Conditions 84
4.2.3.1 Substrate Related Conditions 86
4.2.3.2 Water-Hammer Pressure 87
4.2.3.3 Further Thoughts 89
4.3 Simulations 90
4.3.1 Geometry 90
4.3.2 Simulation Parameters 92
4.3.3 Initial Conditions 93
4.4 Simulation Results 94
4.4.1 Examples 94
4.4.2 General idea of bouncing mechanism 96
4.4.2.1 A Few Definitions 97
4.4.2.2 Two Criteria 98
4.4.2.3 Independence of Criteria 101

5 Theory of Pancake Bouncing **105**
5.1 Theoretical Model 105
5.1.1 Derivation of the Time Scale Criterion 105

5.1.2 Derivation of the Energy Criterion 111
5.2 Theory Results 114
5.2.1 Design Diagram 120
5.3 Discussion of Assumptions Used 126
5.3.1 Laplace Pressure 127
5.3.2 Crashing Time Scale vs Oscillation Time Scale 129
5.3.3 Dissipation Between Posts 131
5.3.4 Effects on $a_{\downarrow}$, $a_{\uparrow}$ 134
5.3.5 Vortical Flow 136
5.4 Summary and Outlook 138

6 Conclusions **143**

References **147**

*

List of Figures

1.1 Definition of the contact angle 2

1.2 Possible wetting states on a smooth substrate 2

1.3 Cassie-Baxter and Wenzel states 4

1.4 Diagram of Gibbs' pinning 6

1.5 Selected figures illustrating drop impact phenomena 10

1.6 Disc-shaped deformation of a droplet impacting on a surface at $We = 12$ 12

1.7 Small deformation of a of a droplet impacting on a surface at $We = 0.07$. 12

2.1 The 19 velocity directions of the lattice Boltzmann algorithm 21

3.1 Superhydrophobic surface with two-tier roughness used for condensation experiments showing coalescence-induced jumping 30

3.2 Side-view of the droplet merge-and-jump process observed by Boreyko et al. 30

3.3 Experimental results from Boreyko et al. 31

3.4 Quasi-2D simulation geometry 40

3.5 Initial conditions and the duplicated simulation box 43

3.6 Streamline plot of the velocity field of coalescing free drops 46

3.7 Evolution of the drop shape starting from the coalescence of two single drops 48

3.8 Variation of the bridge ridge radius b with time 49

3.9 Dimensionless bridge radius b/R for drop radii $R_0 = 40 \ldots 200$ 50

3.10 Coalescence and bouncing process of quasi-2D drop on ridges, order parameter and velocity field 54

3.11 Simulation results for the size dependence of the jumping process 57

3.12 Local dissipation rate for drops of $R_0 = 50$ coalescing on a ridge 58
3.13 Shape of the droplet as it detaches 61
3.14 Evolution of the drop contour with time during coalescence on different surface geometries 64
3.15 Pinning during the receding motion of the contact line 67

4.1 Time sequence of a bouncing process on MTS substrate showing pancake bouncing at $We = 19.6$ 74
4.2 (a) SEM Micrograph of the MTS substrate, (b) Sudden decrease of contact time with increased Weber number for drops bouncing on the MTS surface 75
4.3 Time sequence of a bouncing process on an MTS substrate showing a conventional rebound at $We = 7.8$ 75
4.4 Impact on superhydrophobic posts showing pancake bouncing 76
4.5 Contact time as a function of We for different post substrates and drop sizes 77
4.6 Sketch of the vortical motion revealed by the presence of tracers inside a balloon 85
4.7 Quasi-2D simulation geometry 91
4.8 Evolution of the drop shape during impact on a post surface 94
4.9 Time sequences of the bouncing process in lattice Boltzmann simulations 95
4.10 Diagram to clarify $D(t)$, $l(t)$, and the meaning of f_D 97
4.11 Evolution of drop width $D(t)$ and penetration depth $l(t)$ at two different impact velocities 98
4.12 Simulation and experimental results for the pancake effect 102

5.1 Dependence of l on time and on the squared time, normalised by $t_{l_{max}}$ . . 106
5.2 Fitting the scaling parameters for simulations 115
5.3 Fitting the scaling parameters for experiments 116
5.4 Design diagram for pancake bouncing 120
5.5 Linear fit for the recoil time $t_\uparrow$ with included Laplace force 127
5.6 Linear fits for $\xi_{H,\tau}$, $\xi_{D,\tau}$, and f_K 129

5.7 Time sequences of the local dissipation rate for drop impact 132
5.8 Total dissipation rate within the liquid phase with time 133
5.9 Time sequences of the velocity field for drop impact 134
5.10 Velocity field at approximately the time of lift-off 136
5.11 Evolution of the kinetic energy of centre-of-mass motion and of the internal motion 137
5.12 Snapshots showing the evolution of the velocity field for impact on a substrate of square cells 141
5.13 Snapshots showing the evolution of the velocity field for impact on a substrate of horizontal bars 142

Chapter 1

Introduction

1.1 Basics of the Physics of Wetting

When a liquid, such as water, is deposited on a smooth surface, it can either spread on the surface or form drops in the shape of a spherical cap if effects of gravity can be neglected. For an idealised smooth surface the wetting behaviour depends entirely on the interplay between the interfacial energies of the solid, liquid and gas, i.e. the surface chemistry. At the boundary between two components there is a positive free energy associated with the disruption to bulk molecular interactions. This free energy is proportional to the area of the interface. The constant of proportionality, called the surface tension and denoted σ, is defined as the rate of change of surface energy with respect to the surface area, $\sigma = \mathrm{d}E_S/\mathrm{d}A$. For the current situation of a liquid drop on a surface there are therefore three relevant surface tensions: liquid-gas σ, liquid-solid σ_{LS} and solid-gas σ_{SG}. These surface tensions determine the shape of the liquid drop by controlling the angle the liquid-gas boundary forms with the solid. Consider a liquid wedge, touching a surface at an angle θ (see Fig. 1.1). A displacement of the liquid-solid-gas contact line by a horizontal distance $\mathrm{d}x$ across the surface results in an increase $\mathrm{d}x\cos\theta$ per unit length in the area of the liquid-gas interface. The associated change in energy is therefore

$$\mathrm{d}E = (\sigma_{LS} - \sigma_{SG})\mathrm{d}x + \sigma \mathrm{d}x\cos\theta. \tag{1.1}$$

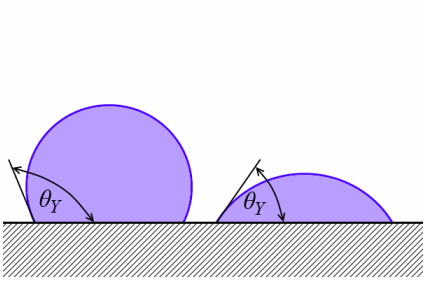


Figure 1.1: Definition of the contact angle.

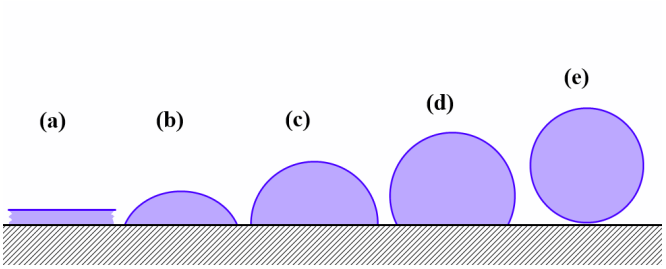


Figure 1.2: Possible wetting states on a smooth substrate: (a) completely wetting, (b) hydrophilic, (c) neutrally wetting, (d) hydrophobic, and (e) completely drying.

In equilibrium, the energy is minimised and therefore $\mathrm{d}E/\mathrm{d}x = 0$, which yields the well-known Young's law [1]

$$\cos\theta_Y = \frac{\sigma_{SG} - \sigma_{LS}}{\sigma}. \tag{1.2}$$

A material is called hydrophilic if $\theta_Y < 90°$ and hydrophobic if $\theta_Y > 90°$. For cases where the right-hand side of Eqn. (1.2) is > 1 the surface is completely wetting, and the liquid will spread out indefinitely as a thin film. For $\frac{\sigma_{SG}-\sigma_{LS}}{\sigma} < -1$ however, the surface is completely drying and the drop will detach. The different wetting states are depicted in Fig. 1.2.

So far we have neglected the influence of gravity in comparison to the influence of surface tension. The energy associated with surface tension scales with the surface area of the drop, $\sim \sigma R^2$. The gravitational energy scales with the mass of the drop, $\sim \rho g R^3 R$, where R denotes the radius of the drop and g is the gravitational acceleration. Gravitational distortions are negligible if $\sigma R^2 \gg \rho g R^4$, i.e. when the drop size obeys

$$R \ll \lambda_c := \sqrt{\frac{\sigma}{\rho g}}. \tag{1.3}$$

λ_c is called the capillary length. For water, λ_c is of order 3 mm. For $R \ll \lambda_c$, and for partially wetting conditions on a smooth surface, a drop forms a spherical cap of constant curvature. This can be understood from Laplace's law, which states that the pressure

difference Δp across a curved interface is

$$\Delta p = \sigma \left(\frac{1}{R_1} + \frac{1}{R_2} \right), \tag{1.4}$$

with the higher pressure located on the concave side of the interface. $\frac{1}{R_1}$ and $\frac{1}{R_2}$ are the principal local curvatures of a curved two-dimensional interface. For a uniform cap, $\frac{1}{R_1} = \frac{1}{R_2} = \frac{1}{R}$ and Eqn. (1.4) reduces to

$$\Delta p = 2\sigma \frac{1}{R}. \tag{1.5}$$

In two dimensions, where $\frac{1}{R_1} = \frac{1}{R}$ and $\frac{1}{R_2} = 0$, the Laplace pressure is given by $\Delta p = \sigma \frac{1}{R}$.

In equilibrium situations the pressure within the drop is necessarily uniform which, according to Laplace's law, is only possible for a constant curvature. Therefore an undisturbed drop assumes a spherical shape, and a drop on a surface, subject to a fixed wetting angle, forms a truncated sphere, or spherical cap, for any $0° < \theta_Y < 180°$.

1.2 Topographically Patterned Surfaces

For conventional surfaces, i.e. chemically treated smooth surfaces, contact angles up to $\approx 120°$ are possible [2, 3]. Higher contact angles can only be achieved when topographical patterning, i.e. surface roughness, comes into play. When surface roughness on a micrometre scale exists in addition to chemical hydrophobicity, much higher contact angles of close to 180° [3, 4, 5] can be observed. Moreover, these surfaces often show very small friction to the motion of water droplets.

Surface roughness is exploited by many plants [5, 6, 7]. The most prominent example is the lotus, famous for its self-cleaning abilities, but more common plants such as the Lady's Mantle, cabbage or pea leaves [8] show such strong water repellency that droplets roll or bounce off upon impact.

Surfaces with roughness features that show high contact angles and very high mobilities with respect to water droplets are called superhydrophobic. Inspired by the examples

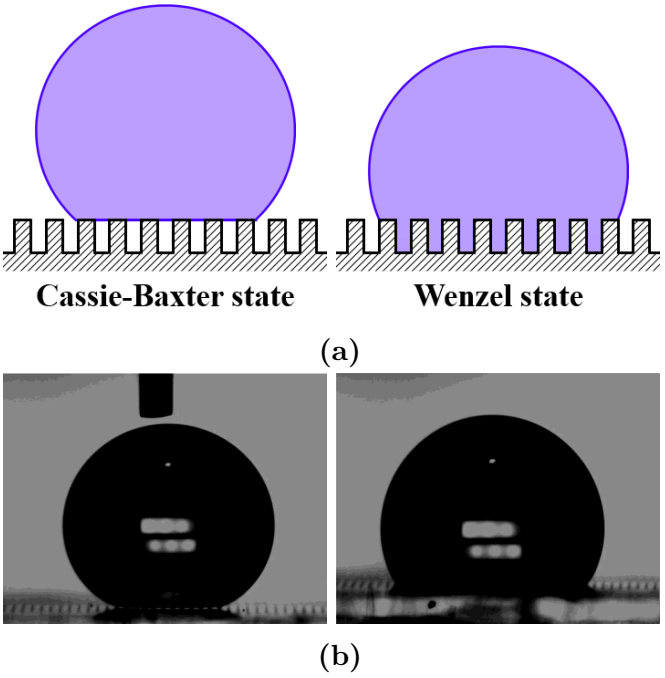


Figure 1.3: Suspendended Cassie-Baxter and collapsed Wenzel state. (a) Schematic illustration, (b) Examples of the Cassie-Baxter and Wenzel states on an artificial superhydrophobic surface. Reprinted with permission from [16]. Copyright (2003) American Chemical Society.

from nature, many different surfaces have been fabricated in recent years to try to exploit applications of superhydrophobicity. Potential uses range from self-cleaning [9] and friction reduction [10, 11] to water harvesting [12, 13] and cooling applications [14]. A simple technical realisation of superhydrophobicity is by patterning a surface with hydrophobic pillars [15, 16], but a wide range of topological structures, such as porous media [17, 18] or carbon-nanotubes [19, 20], coated such that they become hydrophobic, have been studied for their superhydrophobic properties as well.

In this thesis, we are interested in dynamic interactions between superhydrophobic micropatterned surfaces and water droplets. Therefore we will now review the main aspects of the physics of superhydrophobicity.

1.2.1 Superhydrophobic States

Drops on a surface with a topographical pattern can either sit on top of the surface features in the suspended or Cassie-Baxter state [21], with air pockets underneath the drop, or be in a collapsed or Wenzel state [22], where the drop fills the grooves and sits between the features [3], as shown schematically in Fig. 1.3.

For the collapsed state the derivation of Young's law, Eqn. (1.1), is modified to account for the roughness of the surface. When the contact line is displaced by a distance dx the change in the liquid-solid interface per unit length of the contact line is $r\mathrm{d}x$, where r is the roughness factor, the ratio between the true surface area and the projected one. This assumes that the contact line can freely move across surface features, and that it is affected only by the averaged surface features. This assumption requires that the length scale of the surface features be much smaller than the size of the drop itself. The angle formed by the sides of the drop is therefore given by [22]

$$\cos\theta_W = r\cos\theta_Y. \tag{1.6}$$

Drops in this collapsed state, sunken into the structure, are largely immobile: they stick to their position and do not easily roll off the surface when, for example, the substrate is tilted. This is due to pinning, which will be further explained in Sec. 1.2.2.

The state with the striking superhydrophobic properties of high contact angle and easy roll-off is the Cassie-Baxter or suspended state. Similarly to the derivation of the contact angle in the Wenzel state, in the Cassie-Baxter state a displacement dx of the contact line results in a change of $r_\phi\phi_a\mathrm{d}x$ in the liquid-solid interface, together with an additional contribution in the $(1-\phi_a)\mathrm{d}x$ of liquid-gas interface resulting from the air pockets between the roughness features. ϕ_a is the solid fraction in contact with water, projected onto the substrate, and r_ϕ is the area of the surface in contact with water, per unit area of a corresponding smooth surface. Therefore Young's Equation is modified to give [21]

$$\cos\theta_{CB} = r_\phi\phi_a\cos\theta_Y - (1-\phi_a). \tag{1.7}$$

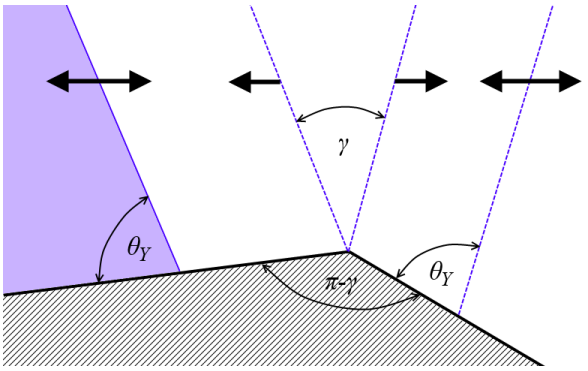


Figure 1.4: Diagram of the Gibbs' pinning effect associated with convex surface features.

For surface features with flat tops, like those we will consider throughout this thesis, $r_\phi = 1$. Suspended drops can have a very high contact angle of up to 160° [23]; they move across the surface very easily, bounce, and roll off [24, 25, 26].

Both Wenzel and Cassie-Baxter states can be thermodynamically stable [27, 28], with a free energy barrier between them depending on surface tension and substrate geometry. The transition from the Cassie-Baxter to the Wenzel state has been shown to be facilitated by applying an external force [3, 29], vibration [30], drop impact [23], or to result from shrinking during evaporation [31, 32].

1.2.2 Pinning and Contact Angle Hysteresis

For the equilibrium contact angle in Young's equation Eqn. (1.2) we have considered only perfectly smooth surfaces. However, in reality, even supposedly smooth surfaces are in most cases neither perfectly smooth nor chemically pure, but can exhibit chemical and topographical defects. Such defects lead to the phenomenon that the contact line can be distorted by a certain angle before it begins to slide. For an advancing and receding motion of the contact line there are two distinct angles, the advancing contact angle θ_a and the receding contact angle θ_r. Between these two the interface remains stable upon deformation and does not move across the surface [33].

Distinct θ_a and θ_r are a manifestation of pinning, first described in 1878 [34]. J.W.Gibbs' seminal paper gave a criterion for the thermodynamic equilibrium of the phase boundary

at a solid corner. It can be formulated as

$$\theta_Y < \theta_{pin} < \theta_Y + \gamma, \tag{1.8}$$

for a dihedral angle γ of the corner, defined as positive for convex and negative for concave corners, as shown in Fig. 1.4. The contact line is thermodynamically stable and does not move for angles between θ_Y and $\theta_Y + \gamma$. From Fig. 1.4 one can see that thermodynamically stable contact angles are only possible for convex corners, while for concave corners no θ_{pin} exists and the contact line jumps around the corner rather than being pinned. The pinning condition Eqn. (1.8) is called the Gibbs criterion in the literature, and has been verified experimentally, for example in [35].

Gibbs' pinning affects the motion of contact lines on patterned surfaces differently for the two wetting states. Let us consider a receding contact line. In the Cassie-Baxter state, the contact line has to de-pin from the posterior edge of a feature, whereas in the Wenzel state de-pinning must occur for both the posterior and the anterior edge of a feature. De-pinning from the anterior edge requires very small angles $\theta \ll \theta_W$, which means the contact line must be strongly distorted from the equilibrium. As a result, the contact line is effectively pinned for a Wenzel drop, resulting in a very low mobility, i.e. sticking of the drop. More generally, the 'stickiness' of a given surface is quantified by the difference between the advancing and the receding contact angle $\Delta\theta = \theta_r - \theta_a$, referred to as the contact angle hysteresis. A surface with high drop mobility typically shows a contact angle hysteresis of $\Delta\theta \lessapprox 5^\circ$ [36].

1.3 Hydrodynamic Regimes

Hydrodynamic processes involving interfaces are subject to different forces: capillary forces arising from the surface tension σ, viscous forces as a result of liquid shear with a viscosity η, and inertial forces as a result of the liquid's density ρ. Moreover, external forces such as gravity can be relevant. Often, hydrodynamic processes happen in parameter regimes

where only a few of these forces govern the process. It has proved useful to describe such regimes with the help of certain dimensionless numbers. For the problems discussed in this thesis, gravity will be neglected, but surface tension, viscosity, and inertia will be relevant to the physics we discuss.

The dimensionless numbers associated with these three forces are

$$We = \frac{\rho v^2 L}{\sigma}, \quad Ca = \frac{\eta v}{\sigma}, \quad Re = \frac{\rho v L}{\eta}, \quad Oh = \frac{\eta}{\sqrt{\rho \sigma L}}, \tag{1.9}$$

the Weber number We, which describes the balance between inertia and surface tension, the capillary number Ca, which balances viscous forces and surface tension, the Reynolds number Re conveying the relative importance of inertia and viscous forces, and the Ohnesorge number Oh, which describes the balance of viscous forces and the combined effect of inertia and surface tension. v and L are characteristic velocity and length scales of the given physical problem, respectively. Estimating v and L for a given physical situation and checking if the respective dimensionless numbers are $\gg 1$ or $\ll 1$ indicates if one of the forces dominates the process.

In turn, if the respective dimensionless number is close to unity, it means that both forces contribute to the physical process and their balance governs the hydrodynamic behaviour. Furthermore, if we know a process to be governed by the balance of certain forces, we can make estimates about typical velocities and time scales for a given L. For example, if we expect a process to be governed by, say, inertia and surface tension, setting $We = 1$ results in $v = \sqrt{\sigma/(\rho L)} =: \nu_{ci}$, the characteristic velocity for capillary-inertial processes. A typical time over which such processes happen is given by $t = L/v = \sqrt{\rho R^3/\sigma} =: \tau_{ci}$, the characteristic time scale for capillary-inertial processes. In the same spirit, $Re = 1$ leads to the typical velocity and length scale for viscous-inertial processes, and $Ca = 1$ yields the respective quantities for viscous-capillary processes.

Listing these parameters:

$$\nu_{ci} = \sqrt{\frac{\sigma}{\rho L}}, \qquad \tau_{ci} = \sqrt{\frac{\rho L^3}{\sigma}}, \tag{1.10}$$

$$\nu_{vi} = \frac{\eta}{\rho L}, \qquad \tau_{vi} = \frac{\rho L^2}{\eta}, \tag{1.11}$$

$$\nu_{vc} = \frac{\sigma}{\eta}, \qquad \tau_{vc} = \frac{\eta L}{\sigma}, \tag{1.12}$$

where the subscripts ci, vi, and vc denote capillary-inertial, viscous-inertial, and viscous-capillary processes, respectively. We shall make use of these scales to understand the dynamic effects considered in this thesis. Finally, we note that setting $Oh = 1$ gives an estimate of the length scale

$$L = \frac{\eta^2}{\rho\sigma} =: \ell_v, \tag{1.13}$$

below which viscous forces dominate over capillary and inertial effects.

1.4 Droplet Impact on Surfaces

The impact of single droplets on surfaces has been of interest to the scientific community for over a century, from description of splash patterns [37, 38] and their photography [39] to the study of the intricate patterns formed by drops rebounding from micropatterned surfaces [40]. The behaviour of drops landing on a surface is relevant to a great number of applications, ranging from drop impact on gas turbine engine blades, spray cooling [41], water harvesting [12, 13, 42, 43], and spraying of plants to inkjet printing, spray painting, spray coating, and anti-icing.

When a drop hits a solid surface it can spread, splash, or rebound, depending on the substrate and drop properties. Relevant parameters of the surface are its surface energy, i.e. the equilibrium contact angle a droplet forms on the substrate, the contact angle hysteresis, roughness properties, and temperature. In this overview we limit ourselves to the cases where the droplet impact is normal, i.e. where the droplet's trajectory prior to impact is parallel to the surface normal, to hard surfaces that are not deformed by

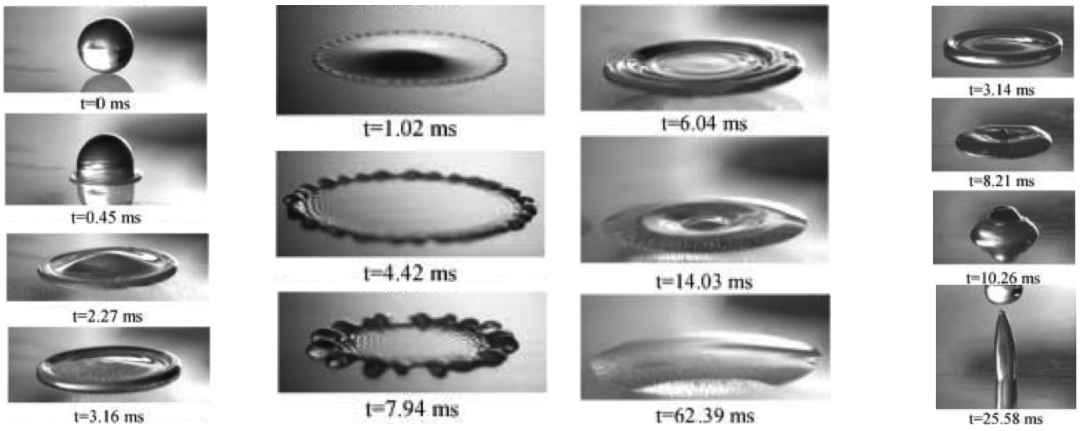


Figure 1.5: Selected figures from [44], Fig. 13 to illustrate the phenomena described in the text. (a) Protruding lamella and rim formation, glass substrate. (b) Distortions of rim, wax substrate. (c) Relaxation of rim, glass substrate. (d) Receding drop and partial rebound, wax substrate. Reprinted with kind permission from Springer Science+Business Media B.V.

the impact, and to dry surfaces, on which no liquid film is present. The drop size is assumed to be smaller than the capillary length, implying that the effects of gravity on the shape and spreading dynamics of the drop are negligible. Besides the features of the surface, the droplet's physical parameters influence the outcome of an impact event. Relevant parameters are impact velocity, drop size, surface tension, the liquid's density and viscosity. For inviscid impact processes, the dimensionless number characterising drop impacts is, following from Eqn. (1.9), $We = \frac{\rho R_0 v_0^2}{\sigma}$, where R_0 denotes the undisturbed drop radius and v_0 the drop's velocity at the moment of impact.

In the following parts of this section we present an overview of the literature concerning drop impact phenomena. In Sec. 1.4.1 we will describe the way in which drops spread, indicating the substrate and impact parameters that determine the physics of each stage of the process. This is followed in Sec. 1.4.2 by a more detailed discussion of the drop shape during spreading and how it depends on the Weber number of the impact. In Sec. 1.4.3 we discuss the necessary surface features to allow a complete rebound of drops falling onto a surface.

1.4.1 Impact Process

A systematic and comprehensive study of the effects of different impact parameters for drops landing on a solid surface was conducted in [44]. Some of their results are discussed here as they give a good overview of the different phenomena that are possible in droplet impact events. In [44] Rioboo et al. study the impact onto hard surfaces, varying droplet diameter, impact velocity, fluid viscosity, surface wettability, and surface roughness. Rioboo and co-workers' observations are described quantitatively and phenomenologically, but without proposing any theoretical models for their observations. Plotting the dimensionless spreading diameter d/D_0, where d is the contact diameter and D_0 is the diameter of the unperturbed drop, against the dimensionless time $t^* = tv_0/D_0$, the authors find that for all impacts they can identify four universal stages: Initially the drop undergoes a kinematic stage, where the shape of the spreading drop depends only on the initial drop diameter and impact velocity, but not on the other parameters including the surface wettability. In the kinematic phase, it is found that the diameter of the contact area of the drop with the solid spreads as $t^{*1/2}$ [44, 45]. The kinematic stage is followed by a spreading phase, where all parameters begin to play a role, a relaxation phase, in which the magnuitude of the receding contact angle is the governing parameter, and finally a wetting/equilibrium phase [44].

Initially, the drop spreads in the shape of a truncated sphere. As the spreading phase sets in, a lamella of liquid protrudes from the truncated sphere, spreading radially, as shown in Fig. 1.5a. In the range of Weber numbers $We = 36 \ldots 390$ considered in [44], the authors observe that the advancing edge of the drop forms a rim, with a thin lamella of liquid in the centre, as depicted in the lower panels of the sequence in Fig. 1.5a. This effect is more pronounced for higher We. The rim can show distortions and the formation of radial liquid filaments for higher impact velocities, or rougher surfaces, up to the ejection of separate drops ('splashing'). These distortions are shown in Fig. 1.5b.

During the spreading phase, part of the kinetic energy of the liquid is dissipated by viscous forces, and part of it is turned into surface energy, as the free-surface area is

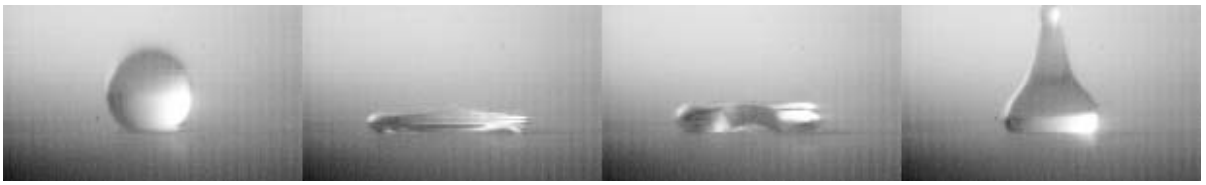


Figure 1.6: Disc-shaped deformation of a droplet impacting on a surface at $We = 12$, sequence reproduced from [50] with permission.

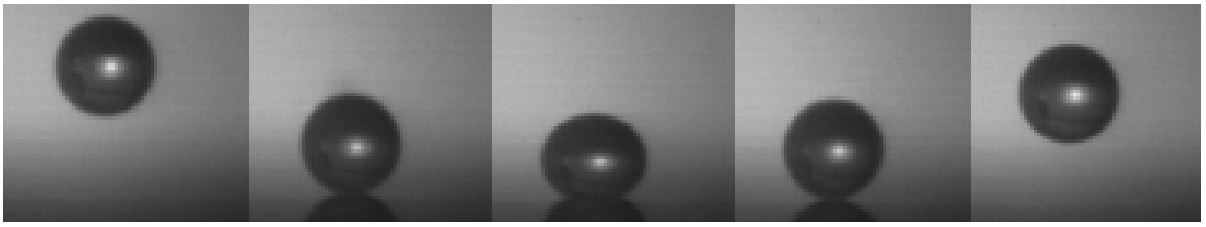


Figure 1.7: Small deformation of a of a droplet impacting on a surface at $We = 0.07$, sequence reproduced from [26] with permission.

greatly increased [46, 47], as is the area of liquid-solid contact. As such, the behaviour during the spreading phase and relaxation phase should depend mainly on the surface wettability [47]. Rioboo et al. indeed find that the rim may relax to form a flat spherical cap as shown in Fig. 1.5c, or recede, if the liquid and surface form a receding contact angle that is not too small. In the process of receding the liquid rises vertically and detachment of a part of the liquid ('partial rebound') may even occur for higher Weber numbers. This process is shown in Fig. 1.5d. For lower impact energies oscillations of the drop are observed [48]. During the last phase the drop attains a constant diameter or continues to slowly wet the surface, for highly wettable surfaces. This process follows the well-known Tanner's law [49], which states that for capillary-driven spreading the drop contact radius grows with time t according to a $t^{1/10}$ power law.

1.4.2 Drop Shape During Spreading

Since later in this thesis in Sec. 5.1.2 we need to make certain assumptions about the shape of the drop as it is spreading, it is worth discussing briefly what drop shapes to expect for different *We*. In the previous subsection we stated that in the experiments described in [44] the authors observed drops spreading in the shape of a lamella bounded by a pronounced toroidal rim, in experiments performed at $We = 36 \ldots 390$. A more

detailed study including theoretical predictions is presented in [51]. In this paper the spreading and receding dynamics of droplet impact are modeled taking the fluid geometry during the process into account. Rim formation was included for $We \geq 10$.

For smaller impact velocities the deformation of the drop must be less. Experiments have been reported [8, 50, 52, 53] in which the spreading drop assumes a disc-like shape showing no rim, as shown in Fig. 1.6. For very low impact velocities $We \ll 1$, on surfaces with a high contact angle, the drop's shape must deviate very little from spherical, as shown in Fig. 1.7. This limit has been considered in a number of studies and addressed both experimentally and theoretically [53, 54, 55, 56].

The condition for a pronounced rim to form has been addressed in [46] by Rein and in [57] by Fedorchenko. The respective authors argue in the following way: the formation of a rim is associated with an increase in surface energy, so surface tension forces would act against its build-up. However, the signal of the shape distortion travels at the speed of capillary waves, $\nu_{ci} = \sqrt{\sigma/(\rho h_r)}$, where h_r here denotes the height of the rim, so if the rim travels faster than ν_{ci}, it remains undisturbed. Assuming that the propagation speed of the rim is $\sim v_0$ the ratio of these two velocities scales as $\sim (D_0/h)^{1/2} We^{-1/2}$. This expression becomes small for large Weber numbers, so a rim only forms for $We \gg 1$.

To conclude, in the range of Weber numbers of $1 \lessapprox We \lessapprox 10$ we expect the impacting drop to assume a disc-like shape when spread maximally. Below this, for $We \ll 1$, deformations are small such that the drop is still approximately spherical, whereas for $We \gtrapprox 10$ higher-order distortions set in and the drop forms a pronounced rim when spreading. In Sec. 4.2.2 and Sec. 5.1.2 we will encounter impact processes of medium Weber numbers $1 \lessapprox We \lessapprox 10$, so we can assume that the drop shape is well approximated by a disc.

1.4.3 Superhydrophobicity for Rebound

In Ch. 4 and Ch. 5 we will be interested in the process of total rebound, that is, the entire drop leaving the surface after impact. Hence we briefly explain here on what types

of surfaces total rebound of droplets can be observed.

To be able to leave the surface after impact a drop needs to retain a large proportion of its initial kinetic energy, i.e. not too much of its energy should be dissipated during the process of spreading and receding. Hartley and Brunskill were the first to claim that surface roughness together with hydrophobicity is necessary for rebound, which they observed for drops impacting on the leaves of certain plants, for example pea leaves, or on carbon black [8, 58]. Today, such surfaces are collectively called superhydrophobic.

This corresponds to the opinion of other researchers [26] that it is the low contact angle hysteresis, which is found on superhydrophobic surfaces, that is necessary to observe full rebound. In fact, in their 1958 paper [8], Hartley and Brunskill correctly identified low contact angle hysteresis as the necessary condition but dismissed the idea at the time thinking that micro-rough surfaces had a *high* contact angle hysteresis. Low contact angle hysteresis is expected to be important because, for inviscid processes, it allows little dissipation during the spreading process, as the dissipation of liquid flowing along a surface scales as $\sim \sigma R_0^2 \Delta \cos\theta$ [59], where $\Delta \cos\theta = \cos\theta_r - \cos\theta_a$. On the other hand, Schiaffino et al. report a mercury drop completely rebounding off a smooth glass surface of $\theta_Y = 123^\circ$ [54], which seems to contradict the necessity of a superhydrophobic surface. However, in [54] nothing is said about the contact angle hysteresis on the surface used, but [60] quote a low contact angle hysteresis of $\Delta\theta = 6^\circ$ for mercury on glass.

Therefore, we can draw the conclusion that surfaces with a low contact angle hysteresis are necessary for drops to completely rebound upon impact. Superhydrophobic surfaces can show such a low contact angle hysteresis. An example of how well superhydrophobic surfaces are able to prevent viscous losses is given in Richard and Quéré's paper from 2000 [26], in which they report a restitution coefficient, the ratio of outgoing to incoming velocity, of up to 0.91 in the limit of small deformations. The example in Fig. 1.7 taken from this paper shows an impact process with a restitution coefficient of 0.88.

Therefore, when in Ch. 4 we need to review literature on the physics of complete drop rebound, we will restrict ourselves to impacts on superhydrophobis surfaces, or Leidenfrost surfaces [53], which provide contact angles of 180° and zero contact angle

hysteresis because the liquid floats on a layer of gas [61].

1.5 Outline of the Thesis

In this thesis we study examples of dynamic drop interaction with topographically patterned surfaces. We focus on two scenarios: the coalescence between two stationary drops placed on a solid surface and the impact of drops on surfaces patterned with posts.

In Ch. 2 the theoretical framework for our numerical simulations is laid out. We describe the thermodynamic and hydrodynamic equations we use to model our system, which we describe as a two-component fluid interacting with a solid surface. Subsequently, the numerical method used to solve these equations, the lattice Boltzmann algorithm, is introduced. We outline how dissipation can be calculated within the framework of the lattice Boltzmann method.

In Ch. 3 we use these numerical simulations to study the phenomenon of coalescence-induced jumping of droplets on superhydrophobic surfaces, motivated by the experimental observation of the effect. We do so by first reviewing coalescence processes in general and performing simulations in two dimensions for drops in free space. We confirm that our simulations recover experimental and analytical results. We proceed by studying the coalescence of drops when placed on a surface, and use our results for the free coalescence to explain how the symmetry breaking due to the surface leads to jumping and to a universal drop shape when the drop is detaching. We also study the interaction with solid substrates of different surface parameters. We discover that in addition to the intrinsic contact angle, the direction of surface features plays an important role as pinning effects may prevent a merged drop from leaving the surface after jumping.

In Ch. 4 we motivate our work on drop impact processes by describing in detail the peculiar experimental observation of pancake bouncing. When falling onto a surface with particular features, a drop may spread and detach in a pancake shape, which we show using our own simulations and experimental results inspired by our simulations. To explain the phenomenon, we review the relevant literature and proceed by explaining in

what respect pancake bouncing provides a departure from previous work. The idea of the physics of pancake bouncing is explained phenomenologically using the simulations, and two distinct criteria are identified which are necessary to permit pancake bouncing. Thereafter, in Ch. 5 we develop a theoretical model for both criteria, and apply it to explain experimental and simulation results in detail. Our theoretical model allows us to identify what surface parameters lead to pancake bouncing.

Chapter 2

The Lattice Boltzmann Method

In this chapter we describe the numerical algorithm used to study two different problems of fluid dynamics involving fluid interaction with a superhydrophobic surface: drops coalescing whilst sitting on a surface and drop impact onto a micropatterned substrate.

Fluid hydrodynamics is described by the Navier-Stokes equations, which are based on the local conservation of mass and momentum [62]. If an algorithm represents these conservation laws correctly, and the discretisation of space is performed in a sufficiently symmetric way, the appropriate hydrodynamic equations will be obtained in the continuum limit [63].

However, for the physical phenomena addressed in this thesis, where a liquid drop and a surrounding gas are present, a fluid description representing the physical liquid and gas phases is needed, and it is necessary to include a surface energy related to their interface. Moreover, the interaction with a solid wall in the presence of such an interface must be represented correctly.

We use a lattice Boltzmann algorithm in the binary model [64], based on that which was developed in the group of Julia Yeomans at Oxford University. In this model, the coexistence of two fluids A and B of densities ρ_A and ρ_B is described by their total fluid density $\rho = \rho_A + \rho_B$ and the order parameter $\phi = \rho_A - \rho_B$ corresponding to the concentration of the two liquids. The binary model allows one to ascribe different viscosities $\eta_{l,g}$ to the fluid components. As the physics we are interested in does not

involve phase changes between the fluid and the surrounding gas, but we expect viscous effects to be important, we represent a physical liquid-gas system by a model for a binary fluid.

We will proceed by describing the physics of the binary fluid and then introduce the lattice Boltzmann algorithm that solves the hydrodynamic equations. Thereafter we will show how our method can be used to calculate dissipation rates within the fluid.

2.1 Thermodynamics of the Binary Fluid

In this section we describe the equilibrium properties of the fluid and introduce a model that embodies the coexistence of two fluids and a surface tension energy associated with the interface between them. We also explain how to describe surface interactions and how these lead to a given a contact angle.

The physics we are interested in is mesoscopic, hence a description of the liquid and the surrounding gas on a molecular scale is not necessary [65].

We use a continuum model to describe the binary fluid system, in the form of a Landau free energy functional that is minimised in equilibrium [66]. The Landau free energy of a binary fluid interacting with a surface is

$$\Psi = \int_V \left(\psi_b + \frac{\kappa}{2} \left(\nabla \phi \right)^2 \right) \mathrm{d}V + \int_S \psi_S \, \mathrm{d}S, \tag{2.1}$$

with

$$\psi_b = \frac{c^2}{3} \rho \ln \rho + A \left(-\frac{1}{2} \phi^2 + \frac{1}{4} \phi^4 \right), \tag{2.2}$$

representing the free energy in the bulk of either fluid. The total density ρ in the first term of Eqn. (2.2) is chosen to be unity everywhere in system. Separation into the two fluid phases is realised by the second term in Eqn. (2.2) which represents a double well potential that gives rise to phase separation into two coexisting bulk phases 1 and 2 with $\phi_1 = 1$ and $\phi_2 = -1$. $c = \Delta x / \Delta t$ is the lattice speed, where Δx and Δt denote the discretisation in time and space. The relation of c to a physical velocity, the speed of

sound, will become clear later. In the computational implementation of our algorithm we use $\Delta x = \Delta t = 1$.

The second term in Eqn. (2.1), involving κ, gives rise to a surface tension associated with the interface between the phases 1 and 2 by penalizing non-uniformities in ϕ [64]. The third term in Eqn. (2.1) is an integral over the surface S of any solid surface. It accounts for the liquid-solid surface tension of either phase with the wall [67].

The chemical potential of the equilibrium system is found by minimising the free energy functional with respect to ϕ. Minimising the bulk terms leads to the chemical potential

$$\mu = -A\phi + A\phi^3 - \kappa \frac{\mathrm{d}^2\phi}{\mathrm{d}x^2}, \tag{2.3}$$

which, for simplicity, is written down in the one-dimensional case. In equilibrium μ is constant, we chose this constant as zero. Setting $\mu = 0$ gives an interface profile

$$\phi = \tanh\left(\frac{2x}{\xi}\right), \tag{2.4}$$

where $\xi = \sqrt{8\kappa/A}$ is the interface width. An expression for the excess free energy arising from the interface can be found by applying Noether's theorem to the volume terms in Eqn. (2.1). Integrating over this contribution together with the κ-term from Eqn. (2.1) gives the surface tension energy associated with the liquid gas interface, $\sigma = \sqrt{\frac{8}{9}\kappa A}$.[65]

Interaction with the solid surface is accounted for by the surface term in Eqn. (2.1), where ψ_S denotes the surface energy density. Following Cahn, this is taken to be of the form $\psi_S = -h\phi_S$, where ϕ_S is the value of the order parameter at the surface [67]. Minimising the free energy at the solid surface leads to an equilibrium boundary condition

$$\kappa \partial_\perp \phi|_S = -h, \tag{2.5}$$

where h is a parameter that is related to the equilibrium contact angle θ_Y of the system via

$$h = \sqrt{2\kappa A}\ \mathrm{sign}\left(\frac{\pi}{2} - \theta_Y\right) \sqrt{\cos\left(\frac{\alpha}{3}\right)\left(1 - \cos\left(\frac{\alpha}{3}\right)\right)}, \tag{2.6}$$

where $\alpha = \cos^{-1}(\sin^2\theta_Y)$ and sign(•) returns the sign of its argument [65]. Eqn. (2.5) is imposed on the system to yield a chosen contact angle, hence h can be chosen to impose a given contact angle on a surface. It was shown in [68] that the correct contact angle is obtained numerically in the range $\theta_Y = 30° \ldots 150°$ for a flat surface.

2.2 Hydrodynamics of the Binary Fluid

The hydrodynamics of the two-phase fluid are governed by

$$\partial_t(\rho v_\alpha) + \partial_\beta(\rho v_\alpha v_\beta) = -\partial_\beta P_{\alpha\beta} + \partial_\beta[\rho\nu(\partial_\beta v_\alpha + \partial_\alpha v_\beta) + \rho\lambda\delta_{\alpha\beta}\partial_\gamma v_\gamma] + \rho a_\alpha, \tag{2.7}$$

$$\partial_t\rho + \partial_\alpha(\rho v_\alpha) = 0, \tag{2.8}$$

$$\partial_t\phi + \partial_\alpha(\phi v_\alpha) = M\nabla^2\mu, \tag{2.9}$$

the Navier-Stokes equation, the continuity equation, and the advection-diffusion equation, respectively. The subscripts α, β, γ denote summation indices for the Cartesian coordinates and $\delta_{\alpha\beta}$ stands for the Kronecker-δ. $\mathbf{v}$ and $\underline{\underline{\mathbf{P}}}$ are the local velocity vector and pressure tensor, respectively, and $\mathbf{a}$ denotes an acceleration provided by an external body force. λ, $\nu = \eta/\rho$, and M are the bulk viscosity, the shear kinematic viscosity, and the mobility describing diffusion, respectively. The pressure tensor can be obtained from the free energy [65] and its components are given by given by [64]

$$P_{\alpha\beta} = (p_b - \kappa\phi\partial_{\gamma\gamma}\phi - \frac{\kappa}{2}(\partial_\gamma\phi)^2)\delta_{\delta_{\alpha\beta}} + \kappa(\partial_\alpha\phi)(\partial_\beta\phi), \tag{2.10}$$

with p_b denoting the bulk pressure

$$p_b = \frac{c^2}{3}\rho + A\left(-\frac{1}{2}\phi^2 + \frac{3}{4}\phi^4\right). \tag{2.11}$$

The bulk pressure is related to the speed of sound c_s in this model via $c_s^2 = \frac{\mathrm{d}p_b}{\mathrm{d}n} = \frac{c^2}{3}$.

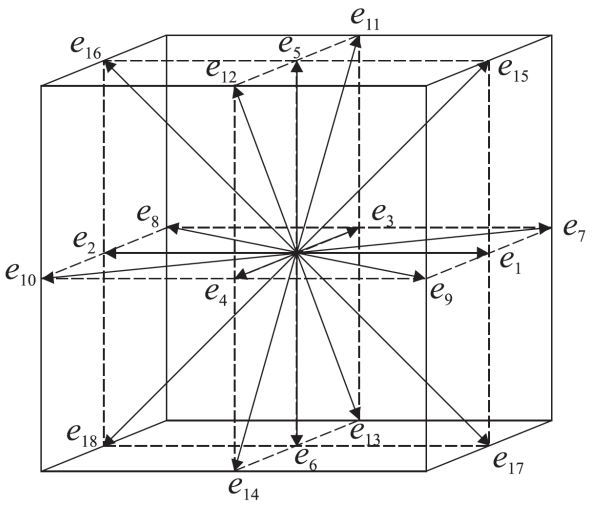


Figure 2.1: The 19 velocity directions of the lattice Boltzmann algorithm. e_0 corresponds to the vector of length zero. Reproduced from [65], Fig. 11.3, with kind permission from Springer Science+Business Media B.V.

2.3 The lattice Boltzmann Algorithm

In this section we outline an algorithm which solves the hydrodynamic equations Eqn. (2.7), Eqn. (2.8), and Eqn. (2.9) governing the hydrodynamics of a binary fluid with a diffuse interface. The lattice Boltzmann method does not solve these equations directly, but evolves a discretised version of the Boltzmann equation [69]. The Boltzmann equation is given by

$$\partial_t f(\mathbf{v}) + \mathbf{v}.\nabla f(\mathbf{v}) = \Upsilon[\{f\}, \mathbf{v}], \tag{2.12}$$

where $f(\mathbf{v}, \mathbf{x}, t)$ is a continuous distribution function and Υ is the rate of collision operator. In the Boltzmann equation, advection of the distribution function f and redistribution of velocities through collision events allow the evolution of the fluid with time. In the so-called Bhatnagar-Gross-Krook approximation [70] the distribution function evolves towards a local equilibrium distribution $\bar{f}$ with a single relaxation time τ according to

$$\partial_t f(\mathbf{v}) + \mathbf{v}.\nabla f(\mathbf{v}) = \frac{1}{\tau}(\bar{f} - f). \tag{2.13}$$

This approach is taken by the single relaxation time lattice Boltzmann algorithm, where time, space, and a set of velocities $\{\mathbf{e}_i\}$ are discretised such that Eqn. (2.13) can be solved

numerically. In our binary model both the fluid density ρ and the order parameter field ϕ have to be advected, which necessitates the introduction of two distribution functions, $\{f_i\}$ for ρ and $\{g_i\}$ for ϕ. Eqn. (2.13) then becomes

$$\begin{aligned} \text{collision}: f_i'(\mathbf{x},t) &= f_i(\mathbf{x},t) - \frac{1}{\tau_\rho}(f_i(\mathbf{x},t) - \bar{f}_i(\mathbf{x},t)) + \mathbf{F}_i, \\ g_i'(\mathbf{x},t) &= g_i(\mathbf{x},t) - \frac{1}{\tau_\phi}(g_i(\mathbf{x},t) - \bar{g}_i(\mathbf{x},t)), \end{aligned} \tag{2.14a}$$

$$\begin{aligned} \text{propagation}: f_i(\mathbf{x}+\mathbf{e}_i\Delta t, t+\Delta t) &= f_i'(\mathbf{x},t), \\ g_i(\mathbf{x}+\mathbf{e}_i\Delta t, t+\Delta t) &= g_i'(\mathbf{x},t), \end{aligned} \tag{2.14b}$$

where the addition of $\mathbf{F}_i$ allows for a local external force. The distribution functions $\{f_i\}$ and $\{g_i\}$ and the set of velocity directions $\{\mathbf{e}_i\}$ discretise space in a certain way. In our model in three dimensions they correspond to the 19 discrete vectors shown in Fig. 2.1. Their components are either zero or $c = \Delta x/\Delta t$, the lattice velocity.

The discretised distribution functions $\{f_i\}$ and $\{g_i\}$ are related to the physical variables of the system according to

$$\rho = \sum_i f_i, \quad \rho u_\alpha = \sum_i f_i e_{i\alpha}, \quad \phi = \sum_i g_i. \tag{2.15}$$

$\mathbf{u}$ is related to $\mathbf{v}$ and the body force $\mathbf{a}$, as $\mathbf{u} = \mathbf{v} - \mathbf{a}\Delta t/2$, but in practice the distinctions between $\mathbf{u}$ and $\mathbf{v}$ can usually be neglected [65]. Eqns. (2.14) recover the laws describing the physical continuum, Eqn. (2.7), Eqn. (2.8), and Eqn. (2.9) if the following set of constraints on the equilibrium distribution functions $\{\bar{f}_i\}$ and $\{\bar{g}_i\}$, derived for example

in [69, 71], is fulfilled:

$$\sum_i \bar{f}_i = \rho, \quad \sum_i \bar{f}_i e_{i\alpha} = \rho v_\alpha, \tag{2.16a}$$

$$\sum_i \bar{g}_i = \phi, \quad \sum_i \bar{g}_i e_{i\alpha} = \phi v_\alpha, \tag{2.16b}$$

$$\sum_i \bar{f}_i e_{i\alpha} e_{i,\beta} = P_{\alpha\beta} + \rho v_\alpha v_\beta, \tag{2.16c}$$

$$\sum_i \bar{g}_i e_{i\alpha} e_{i,\beta} = \Gamma\mu\delta_{\alpha\beta} + \phi v_\alpha v_\beta, \tag{2.16d}$$

$$\sum_i \bar{f}_i e_{i\alpha} e_{i,\beta} e_{i,\gamma} = \frac{\rho c^2}{3}(v_\alpha\delta_{\beta\gamma} + v_\beta\delta_{\alpha\gamma} + v_\gamma\delta_{\beta\alpha}), \tag{2.16e}$$

$$\sum_i F_i = 0, \quad \sum_i F_i e_{i,\alpha} = \Delta t\left(1 - \frac{1}{2\tau_\rho}\right)\rho v_\alpha, \tag{2.16f}$$

$$\sum_i F_i e_{i\alpha} e_{i\beta} = \Delta t\left(1 - \frac{1}{2\tau_\rho}\right)\rho(v_\alpha a_\beta + a_\alpha v_\beta). \tag{2.16g}$$

It can be shown [72] that these constraints are satisfied by choosing $\bar{f}_i$, $\bar{g}_i$, and F_i in the form of a power series expansion in $\mathbf{v}$:

$$\begin{aligned}
\bar{f}_i =& \frac{w_i}{c^2}\Bigg\{p_b - \kappa\phi\nabla^2\phi + e_{i\alpha}\rho v_\alpha + \frac{3}{2c^2}\left(e_{i\alpha}e_{i\beta} - \frac{c^2}{3}\delta_{\alpha\beta}\right) \\
&\times\left(\rho v_\alpha v_\beta + \lambda\left[v_\alpha\partial_\beta + v_\beta\partial_\alpha + \delta_{\alpha\beta}v_\gamma\partial_\gamma\right]\rho\right)\Bigg\} \\
&+ \frac{\kappa}{c^2}\left(w_i^{xx}\partial_x\phi\partial_x\phi + w_i^{yy}\partial_y\phi\partial_y\phi + w_i^{zz}\partial_z\phi\partial_z\phi\right) \\
&+ \frac{\kappa}{c^2}\left(w_i^{xy}\partial_x\phi\partial_y\phi + w_i^{yz}\partial_y\phi\partial_z\phi + w_i^{zx}\partial_z\phi\partial_x\phi\right),
\end{aligned} \tag{2.17}$$

$$\bar{g}_i = \frac{w_i}{c^2}\left\{\Gamma\mu + e_{i\alpha}\phi v_\alpha + \frac{3}{2c^2}\left(e_{i\alpha}e_{i\beta} - \frac{c^2}{3}\delta_{\alpha\beta}\right)\phi v_\alpha v_\beta\right\}, \tag{2.18}$$

$$F_i = \frac{w_i}{c^2}\left(1 - \frac{1}{2\tau_\rho}\right)\left\{e_{i\alpha}\rho a_\alpha + \frac{3}{2c^2}\left(e_{i\alpha}e_{i\beta} - \frac{c^2}{3}\delta_{\alpha\beta}\right)\rho(v_\alpha a_\beta + a_\alpha v_\beta)\right\}. \tag{2.19}$$

The coefficients w can be chosen such that spurious velocities in the binary fluid interface, small velocities which arise even in equilibrium due to discretisation errors [73], can be

minimised. Such a choice, given in [72] is

$$
\begin{aligned}
& w_{1-6} = \frac{1}{6}, \quad w_{7-18} = \frac{1}{12}, \\
& w^{xx}_{1,2} = w^{yy}_{3,4} = w^{zz}_{5,6} = \frac{5}{12}, \\
& w^{xx}_{3-6} = w^{yy}_{1,2,5,6} = w^{zz}_{1-4} = -\frac{1}{3}, \\
& w^{xx}_{7-10} = w^{xx}_{15-18} = w^{yy}_{7-14} = w^{zz}_{11-18} = -\frac{1}{24}, \\
& w^{xx}_{11-14} = w^{yy}_{15-18} = w^{zz}_{7-10} = \frac{1}{12}, \\
& w^{xy}_{1-6} = w^{yz}_{1-6} = w^{zx}_{1-6} = 0, \\
& w^{xy}_{7,10} = w^{yz}_{11,14} = w^{zx}_{15,18} = \frac{1}{4}, \\
& w^{xy}_{8,9} = w^{yz}_{12,13} = w^{zx}_{16,17} = -\frac{1}{4}, \\
& w^{xy}_{11-18} = w^{yz}_{7-10} = w^{yz}_{15-18} = w^{zx}_{7-14} = 0.
\end{aligned} \tag{2.20}
$$

The hydrodynamic parameters in Eqn. (2.7), Eqn. (2.8), and Eqn. (2.9) are related to the lattice Boltzmann algorithm by the relaxation times τ_ρ and τ_ϕ:

$$\nu = \frac{c^2 \Delta t}{3}\left(\tau_\rho - \frac{1}{2}\right), \tag{2.21}$$

$$\lambda = \nu\left(1 - \frac{3c_s^2}{c^2}\right), \tag{2.22}$$

$$M = \Delta t \Gamma \left(\tau_\phi - \frac{1}{2}\right). \tag{2.23}$$

The relaxation times therefore have to be $> \frac{1}{2}$ to give positive quantities M and ν. In our algorithm $\Delta t = \Delta x = 1$, which results in $\lambda = 0$ and incompressibility of the fluid. Γ is a tunable parameter of the system which determines the diffusion strength. In all our simulations we use a fixed $\Gamma = \frac{1}{2}$.

2.3.1 Spurious Velocities and the Multiple Relaxation Time Approach

Spurious velocities can be a problem in lattice Boltzmann simulations. These are unphysical currents near a curved interface, arising from discretisation errors. The discretisation errors lead to gradients in μ which drive the system locally out of equilibrium and hence lead to velocity currents. Our choice of the coefficients w, Eqn. (2.20), aims to minimise these currents near the interface [72].

In the binary system where the interface is in contact with a solid wall a second class of spurious velocities arises due to long-range interactions in the presence of a wall, or from the bounce-back boundary conditions [74]. These spurious currents lead to the system assuming the wrong contact angle. Spurious velocities related to the presence of a wall are damped out if $\tau_\rho = 1$ is chosen. However, this choice limits the accessible physical parameters as it means that both fluid components of the binary mixture would have to have the same kinematic viscosity $\nu = \frac{c^2\Delta t}{3}\left(\tau_\rho - \frac{1}{2}\right)$, whereas we would like to assign different τ_ρ to each phase.

The spurious velocities arising from $\tau_\rho \neq 1$ can be minimised if the term $\frac{1}{\tau_\rho}(f_i(\mathbf{x},t) - \bar{f}_i(\mathbf{x},t))$ on the right hand side of Eqn. (2.14) is replaced by [74]

$$\underline{\underline{\mathbf{M}}}^{-1}\underline{\underline{\mathbf{S}}}\underline{\underline{\mathbf{M}}}(\mathbf{f} - \bar{\mathbf{f}}), \tag{2.24}$$

where $\mathbf{f}$ are the $\{f_i\}$ written as a column vector. $\underline{\underline{\mathbf{M}}}$ and $\underline{\underline{\mathbf{S}}}$ are the matrices given in [74], $\underline{\underline{\mathbf{S}}}$ contains τ_ρ in relevant entries. This approach allows different relaxation parameters to be used for different linear combinations of the f_i. $\underline{\underline{\mathbf{M}}}^{-1}\underline{\underline{\mathbf{S}}}\underline{\underline{\mathbf{M}}}$ affects a change of basis to more physically relevant variables, ρ, the conserved moments ρu_α and the components of the viscous stress tensor $\underline{\underline{\sigma}}$ [65], and thus allows a more correct relaxation of these variables. In practice $\underline{\underline{\mathbf{M}}}^{-1}\underline{\underline{\mathbf{S}}}\underline{\underline{\mathbf{M}}}$ is not calculated at every time step, but a lookup table for various values of τ_ρ is created.

2.3.2 Boundary Conditions

Two boundary conditions are important in drop dynamic problems: the correct wetting angle, and the no-slip boundary condition which states that the fluid velocity at the fluid-wall boundary has to be zero.

The wetting boundary condition is implemented by fixing the perpendicular derivative of ϕ at the wall, Eqn. (2.5). Since the problems studied in this thesis involve only solid walls parallel to the lattice directions setting the derivative is done in a simple manner. At the second node within the solid we set the order parameter to the value of the first node outside the solid minus twice the derivative that we want to impose.

The no-slip condition is implemented by using a link bounce back rule first used for lattice Boltzmann algorithms by Ladd [75]. The fluid flow at the surface is arrested by reversing the populations g_i and f_i entering the wall during the propagation step, Eqn. (2.14b). Details of the implementation are given in [74, 75].

2.3.3 Energy and Dissipation in Lattice Boltzmann

In our research we will study the physics of drop jumping induced by coalescence and drop bouncing. For these processes an understanding of energy dissipation is crucial; we expect it to be an important factor in experimental observations. In this section we will explain how dissipative processes can be studied using lattice Boltzmann simulations.

Our calculation of dissipation in the diffuse interface lattice Boltzmann model follows Qian et al. [76]. The authors find four sources of dissipation in the binary model they consider:

1. Shear viscosity in the bulk of the two liquids $R_v[v] = \int \frac{\eta}{2}(\frac{\partial v_i}{\partial x_j} + \frac{\partial v_j}{\partial x_i})^2 \mathrm{d}\mathbf{r}$,
2. Fluid slipping at the fluid-solid interface $R_s[v] = \int \beta (v_\tau^{slip})^2 \mathrm{d}S$,
3. Composition diffusion in the bulk $R_d[v] = \int \frac{\mathbf{J}^2}{M} \mathrm{d}\mathbf{r}$,
4. Composition relaxation at the interface $R_r[v] = \int \frac{\dot{\phi}^2}{\Gamma} \mathrm{d}S$,

where β is a slip coefficient such that $\eta/\beta = l_s$ is a slip length, allowing for a tangential slip velocity v_τ^{slip}. $\mathbf{J}$ is the diffusive current, which, in our own notation, is $\mathbf{J} = -M\nabla\mu$.

Γ here is a surface diffusion constant, which plays a similar role to M in the bulk and appears in a surface specific version of the advection-diffusion equation [76].

However, not all of these four dissipation contributions apply to our system as we consider different boundary conditions. The first difference is that the authors allow a finite slip velocity v_τ^{slip} of the liquid at the solid surface, whereas our boundary condition is no-slip. In their model, no-slip is achieved by letting $\beta \to \infty$, which would correspond to infinite dissipation. In our model however, we set $v_\tau^{slip} \equiv 0$ from the outset as an independent condition that is not inherent to the binary fluid free energy description. Hence we conclude that we can set $R_s \equiv 0$.

Moreover, the last contribution, R_r, does not apply in our model. Qian et al. [76] find R_r as a consequence of distinguishing between the bulk chemical potential μ and its surface counterpart that they introduce and denote as L. Translated to our notation L is found from minimising the surface free energy density according to $\frac{\delta\Psi}{\delta\phi}|_S = L = \kappa\partial_\perp\phi|_S + \frac{\partial\Psi_S}{\partial\phi_S}$. Qian and co-workers derive an analogue of the bulk advection-diffusion equation Eqn. (2.9), in which Γ enters as a parameter, such that $\dot{\phi} = -\Gamma L(\phi)$. The equilibrium condition for L is $L = 0$, from which our boundary condition $\kappa\partial_\perp\phi|_S = -\frac{\partial\Psi_S}{\partial\phi_S}$ follows. In Qian's model, L is a variable, but in our framework we use $L = 0$ to set our wetting boundary condition as we enforce $\kappa\partial_\perp\phi|_S = -h$ at every time step. Therefore, in the approach used in this work $L \equiv 0$ at every time step, hence $\dot{\phi} = -\Gamma L(\phi) \equiv 0$, and $R_r = \int \frac{\dot{\phi}^2}{\Gamma} \mathrm{d}S \equiv 0$.

We deduce that the dissipation rate (per unit volume) of the system for our LB binary model is a sum of viscous dissipation from shear flow

$$\Phi_\eta = \frac{\eta}{2}\left(\frac{\partial v_i}{\partial x_j} + \frac{\partial v_j}{\partial x_i}\right)^2 \tag{2.25}$$

and dissipation from diffusion

$$\Phi_M = M\left(\nabla\mu\right)^2. \tag{2.26}$$

Therefore the total dissipation rate is

$$\dot{E}_d = \int_V \Phi_\eta \mathrm{d}V + \int_V \Phi_M \mathrm{d}V. \tag{2.27}$$

These dissipation rates however do have corrections which arise from the same reasons as spurious currents in lattice Boltzmann simulations. A curved interface between the two fluid phases will, due to discretisation errors, give rise to $\nabla\mu \neq 0$ even in equilibrium, leading to spurious diffusive dissipation. The spurious velocities arising from $\nabla\mu \neq 0$ will enter into Eqn. (2.25), resulting in spurious shear dissipation.

Moreover, we also see spurious dissipation at corners of walls. Implementing $\kappa\partial_\perp\phi|_S = -h$ is straightforward on flat walls, but leads to μ gradients on solid corners, which in turn result in spurious currents and spurious dissipation. However, in this thesis we do not attempt to quantify exactly local dissipation rates. For studying the relative relevance of dissipation contributions Eqn. (2.25) and Eqn. (2.26) provide useful tools.

Chapter 3

Jumping Drops

3.1 Self-Propelled Droplet Jumping in Experiments

In this section we describe the experimental work which motivated our research on coalescence that is presented in this chapter. Boreyko and co-workers were the first to observe a remarkable behaviour of coalescing drops [77]: when two drops coalesce on a superhydrophobic surface, the resulting drop can jump off the surface. We will describe the experimental work and results from 2009 in detail and then summarize other studies that have subsequently considered droplet jumping upon coalescence.

3.1.1 Experiments by Boreyko et al.

In their 2009 paper [77] Jonathan Boreyko and co-workers studied the effect of superhydrophobicity on the condensation of drops on a surface. They took video images of water droplets growing on a chilled surface and monitored the surface coverage and average size of the droplets. The superhydrophobic substrate they investigated was manufactured with so-called two-tier roughness: A silicon substrate was patterned with silicon micropillars of 3.7 µm width and 12 µm spacing and subsequently covered with a forest of carbon nanotubes (CNTs). A picture of this surface is given in Fig. 3.1. The surface was coated with hexadecanethiol, and condensation on this substrate was compared to that on a smooth surface coated with the same chemical compound, to serve as a control case.

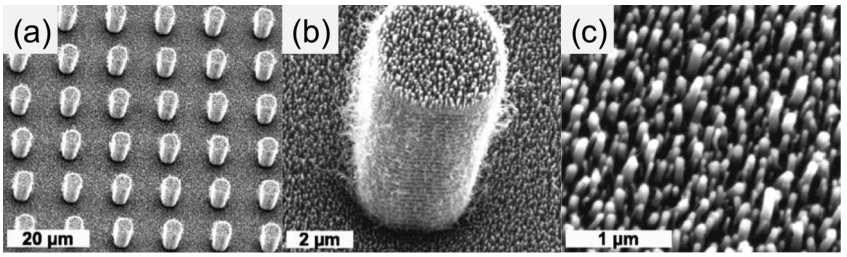


Figure 3.1: Superhydrophobic surface with two-tier roughness used in [77]. Structure (a) is used in the condensation experiments showing coalescence-induced jumping. (b) Single silicon micropillar, covered with CNT nanopillars. (c) Close-up CNT nanopillars. Image from [19].Reprinted with permission from [19]. Copyright (2007), AIP Publishing LLC.

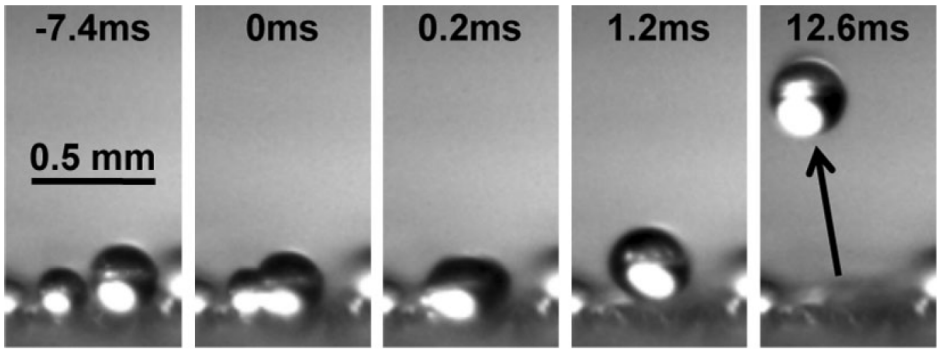


Figure 3.2: Side-view of the droplet merge-and-jump process observed in [77]. The right drop has initial momentum from a previous coalescence, the merged drop has additional out-of-plane momentum as a result of the present coalescence. Reprinted figure with permission from [77]. Copyright (2009) by the American Physical Society.

Boreyko et al. observed that the superhydrophobic surface was much more effective in condensing water. Since there is no removal mechanism, droplets would continue to grow on the smooth surface until only a few large drops covered the surface. This was assumed to inhibit heat transfer and thus to make condensation less effective [77, 78]. In contrast, on the superhydrophobic surface, drops were seen to grow but then get autonomously removed, keeping the average drop size fixed and small compared to the smooth sample.

The autonomous removal is what is of interest for the present work. What Boreyko and co-workers observed was unexpected: when static but growing droplets happened to get in contact, they would coalesce, and at the end of the merging process detach from the surface in an out-of-plane jump. Jumping velocities of up to 0.25 m/s were recorded. Fig. 3.2 depicts an example of such a merge-and-jump occasion. The jumping could however only be observed if the initial droplets had reached a sufficient size. When

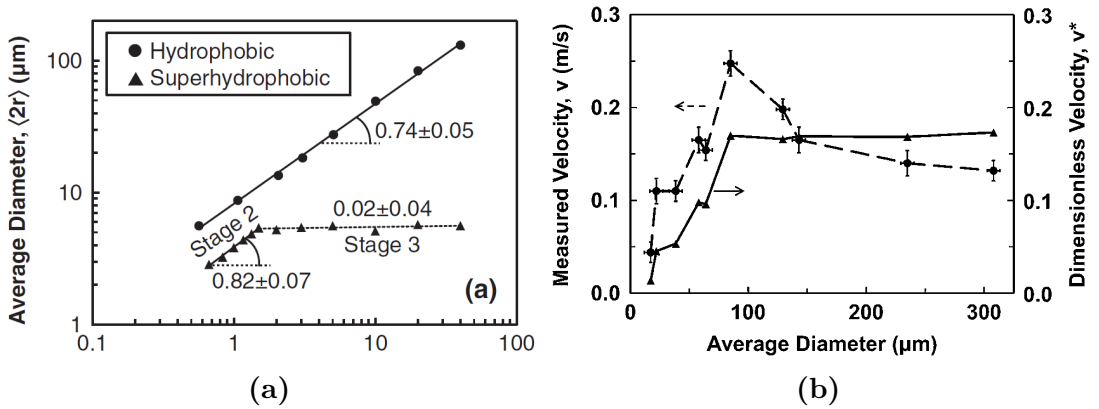


Figure 3.3: Experimental results from [77]. (a) Temporal evolution of the average drop diameter. The x-axis is time in minutes, the numbers shown are the exponents for the assumed powers law dependencies of the drop size on time, $\langle 2R_0 \rangle \sim t^{\alpha}$, of the average initial drop diameter $\langle 2R_0 \rangle$. (b) Jumping velocity of merged drop as a function of $\langle 2R_0 \rangle$. Both the absolute velocity and the dimensionless velocity $v^* = v/\sqrt{\sigma/(\rho\langle R_0 \rangle)}$ are shown. Reprinted figure with permission from [77]. Copyright (2009) by the American Physical Society.

smaller drops merged, the resulting drop simply sat on the surface like its predecessors.

By measuring the average drop diameter across the sample, the authors could unambiguously identify three separate stages of condensation on the superhydrophobic surface: growth without coalescence, conventional coalescence of two drops forming a new, bigger drop on the surface ('immobile coalescence'), and coalescence with a subsequent jump and the resulting droplet bouncing across the substrate ('mobile coalescence'). On the smooth control surface, only the first two stages were present.

Mobile coalescence appeared only above a clear threshold value of the average drop diameter, and, subsequently, the average drop diameter stayed constant within experimental error. To indicate how unambiguous this separation between stage two and three was, the relevant plot from [77] is shown in Fig. 3.3a. With regard to the individual drop sizes necessary for jumping, the authors found that at least one of the drops involved had to have a diameter larger than 10μm.

Boreyko et al. attempted a theoretical explanation for this threshold drop size. In order to estimate the minimum drop radius R_0 necessary for jumping, they assume the energy released from surface tension is fully turned into kinetic energy and hence a velocity. For equal-sized drops this leads to a characteristic velocity of $\nu_{ci} \sim \sqrt{\frac{\sigma}{\rho R_0}}$,

controlled by the liquid-gas surface tension σ and the liquid's density ρ. As such, they assume the process is a process balancing capillarity as a driving force and inertia as the limiting factor [79, 80].

To estimate when this assumption breaks down, i.e. viscosity starts playing a role, they calculate the Reynolds number for the given system, $Re = \rho v L/\eta$, see Eqn. (1.9). Inserting the capillary-inertial velocity ν_{ci} as characteristic velocity and the initial drop radius R_0 as characteristic length scale they find that Re becomes smaller than unity, i.e. viscous forces dominate over inertial ones, when $R_0 < r_c \sim \eta^2/\sigma\rho$, with r_c being the critical radius for jumping to be observed. For water, this theoretical prediction leads to a critical diameter of 10 nm [77], but the experimentally observed value below which the drops did not jump was of the order of 10 µm. So, according to the authors, the theoretical argument underestimates the critical size by three orders of magnitude. Boreyko and co-workers appreciate that neglecting dissipative processes in early-stage coalescence [79, 81] and in contact line movement [82, 83] may play a role in causing this discrepancy.

Boreyko and co-workers also measured the jumping velocity v_{jump} of the coalesced drop. After a steep increase in velocity with increasing drop size for small drops, they found that for drops of about 85 µm average diameter the velocity was maximal, and for larger drops it decreased again. The dimensionless velocity v_{jump}/ν_{ci} however stayed approximately constant for drop diameters larger than 85 µm. This can be seen in Fig. 3.3b. To characterise the influence of viscous effects, the authors state that for their smallest jumping drop $Re = 0.38$ and at the maximum velocity $Re = 11$.

3.1.2 Subsequent Studies

Following Boreyko and co-workers' publications in 2009 several other research groups have addressed the phenomenon of droplet jumping upon coalescence. Wang and co-workers [84] have recently presented an explanation how Boreyko et al.'s velocity measurements depend on drop size using analytical arguments. They consider how much energy should

be released by the transition from two smaller drops to one resulting big drop. Estimating how much energy is dissipated in the coalescence process and deducting this from the available energy, they find that the kinetic energy should scale with initial drop size as

$$E_K \approx \alpha\sigma R_0^2 - \beta\eta\sqrt{\frac{\sigma R_0^3}{\rho}}, \tag{3.1}$$

and hence that the jumping velocity scales with drop radius as

$$v_{jump} = \sqrt{\frac{\sigma}{\rho R_0}}\left(\delta - \epsilon\frac{\eta}{\sqrt{\rho\sigma R_0}}\right)^{\frac{1}{2}}, \tag{3.2}$$

where α, β, δ, and ϵ are numerical prefactors. This scaling for v_{jump} reproduces qualitatively the behaviour of the jumping velocity with drop size in Fig. 3.3b.

In [17] He et al. study the effect of surface adhesion energy, $W_{adh} = \sigma(1 + \cos\theta_r)$, on the ability of drops to jump following coalescence, together with the effect of the ratio of drop sizes. This formula for W_{adh} is cited from [85], but other authors [86] state that the apparent equilibrium contact angle θ_e should be used rather that the receding contact angle θ_r. W_{adh} is not taken into account in [84] as a possible inhibitor of jumping after coalescence. He et al. [17] observe jumping for initial droplet diameters in the range of $10 \ldots 30\,\mu\text{m}$. Ignoring dissipation the authors introduce an energy barrier E^* that is said to increase with W_{adh}, but the functional dependency is not given. If the initial energy of the two coalescing drops is larger then E^* then the drop can jump. This leads to a simple expression $1 + \left(\frac{R_1}{R_2}\right)^2 - b\left(1 + \left(\frac{R_1}{R_2}\right)^3\right)^{2/3} \geq 0$, where b is a factor that incorporates the energy barrier and increases with W_{adh}, and $R_{1,2}$ are the radii of the initial droplets. This model reproduces their experimental findings which are that jumping occurs more often on the surface with low W_{adh}, and that as W_{adh} increases the necessary ratio R_1/R_2 for jumps to occur decreases to unity. However, no explanation is given for the threshold absolute size of the droplets below which jumping is suppressed.

Another theoretical study on the mechanism of droplet bouncing was presented by Liu et al. [87]. The authors consider the drop coalescence and jumping motion as a

two-stage process. The first stage comprises coalescence which results in a composite drop in the shape of a spherical cap, sitting on the surface but spread wider than its equilibrium configuration. The second stage is the receding motion of this composite drop, which can lead to jumping if the driving force is large enough. The authors of [87] focus their attention on the second stage. They propose a force balance equation involving the driving force from the composite drop being out of equilibrium, a retardation force, gravity, and the inertia of the receding motion. The retardation is considered as resulting from adhesion and the theory accounts for different surface types (smooth, micro-patterned, or nano-patterned), for different wetting states (Wenzel, Cassie-Baxter), and for the surface parameters. The force balance equation is the solved numerically. The authors find that jumping cannot take place if the coalesced drop sits on a flat surface, or if the drop is in a Wenzel state on a superhydrophobic surface with micro-roughness. For a Wenzel state with non-impaled nano-roughness the surface parameters are important: the smaller the area fraction ϕ_a of the surface, and the larger the intrinsic angle or surface tension, the better the drop jumps. Cassie drops on such a two-tier surface are shown to jump easily if the drops are not too small, in the range of a few tens of micrometres.

Although the conclusions of this paper seem reasonable the initial assumption needs revisiting. Both the authors' experiments and my simulations show that the drop does not form a spherical cap before the receding motion that leads to jumping sets in.

3.1.3 Motivation and Outline of the Chapter

The question of whether a coalescence event leads to the merged drop leaving the surface is an important one, as efficient removal of droplets is an important aspect in many applications, most prominently water harvesting and device cooling. In such situations, vapour condensation is the key step. It has been shown that heat and mass transfer in condensation is much more effective if it happens drop-wise rather than film-wise [88]. The difference is at least an order of magnitude, and it is predominantly the small droplets which most efficiently transfer the majority of the heat from the surface [89, 90].

In recent papers surfaces with combined chemical functionalisation and microscopic roughness were studied with respect to water condensation efficiency. Such superhydrophobic surfaces allow droplets that are large enough to roll off the surface due to gravity [25, 91], thereby limiting the maximum size of condensing droplets up to the millimetre range. Using additional nanoscopic patterning, condensing drops were shown to be even more mobile and shedding occurred at drop sizes significantly below the capillary length, in the range of $\approx 100\,\mu m$ [14, 19].

Boreyko's work presented in Sec. 3.1.1 showed that drop removal can be facilitated by coalescence, independent of gravity, and allow even smaller droplets of 10–100 µm to leave the surface. Further work was done fabricating special two-tier surfaces designed to achieve spontaneous removal of small droplets [20, 92], increasing the drop number density by $\approx 65\%$ and the self-removal volume by $\approx 450\%$ compared to nanopatterned surfaces [20].

In [93] it is pointed out that, in addition to drop size, drop morphology is also crucial for efficient heat and mass transfer. A drop in the Cassie state has much less contact with the substrate than a collapsed drop, and it was shown in [93] that this leads to a 4–6 times lower heat transfer rate than for a partially wetting drop.

To summarize, self-removal of droplets due to drop coalescence is an important pathway to facilitate efficient drop removal and therefore heat and mass transfer in water harvesting and thermal management applications. Evidently, one key point is to understand how the ability to jump depends on the size of the droplet, and another is to investigate how surface features influence the coalescence and jumping mechanism. Size dependence was discussed in [77], but their model for the minimum drop radius ignored dissipation and underestimated the observed critical value by three orders of magnitude. Clearly, a better understanding of the influence of dissipation is necessary, together with how jumping is affected by the surface morphology. In this Chapter, we will try to shed light on these two aspects.

In order to understand the mechanism of coalescence on a superhydrophobic surface, and possibly jumping, it is helpful to review previous work on droplet coalescence processes.

This will be done in Sec. 3.2. We performed lattice Boltzmann simulations in order to approach the problem of coalescence-induced jumping, the simulations are described in Sec. 3.3. In Sec. 3.4 we will present results for drop coalescence in free space, without a surface, to both confirm that our simulations show the behaviour predicted in the literature and provide a comparison to our simulations for coalescence of drops on a surface. We will describe the mechanisms governing drop coalescence when a surface is present in Sec. 3.5. Sec. 3.6 will address the relevance of surface topology and pinning to coalescence-induced jumping.

3.2 Drop Coalescence: a Summary of the Literature

The physics of the coalescence of two liquid drops is a widely discussed topic in the fluid dynamics community. Publications span from analytical studies of the two-dimensional problem in the viscous (Stokes) regime to numerical studies of the bridging process in the inviscid case, and to experimental work on pendent and sessile drops. Hopper [94, 95] provides a fully analytical solution of the complete merging process of two equally-sized cylinders in the regime of creeping flows, i.e. in the viscous case, when the Stokes equation describes the hydrodynamics of the system . In [96, 97], he discusses the problem of two cylinders of different size, and solves it numerically, again in the Stokes regime.

Most publications, however, study the initial part of the coalescence process, when the two surfaces have just joined in a very small area, and a liquid bridge of radius b is opening up to merge the drops. Examples of numerical investigations are [79, 98], which employ boundary-integral methods to study the inviscid regime. In [99] a finite-element algorithm is used to solve the full Navier-Stokes equation. Jia et al [100] and Gross et al. [101] study viscous coalescence using lattice Boltzmann simulations. Recent experimental papers study the early stage of coalescence of a pendent and a sessile droplet [81, 102], two pendent drops [102], two sessile drops [103], and quasi-two-dimensional oil lenses immersed in water [104]. In [82, 83, 105, 106] the effect of the drops coalescing on a surface is studied, including the process of the shape relaxing to a new sessile drop.

Most experimental work is limited to the early stage of bridge opening where the neck radius is small compared to the drop size. This is because theoretical studies (apart from Hopper's analytical solution of the Stokes case) so far required $b \ll R_0$, and because experimentally the later stage, when the bridge radius approaches the size of the initial drop radius, is difficult to access. This is due to the fact that the two coalescing droplets must be supported in some way: suspended from a syringe [99], sessile on a surface [82, 83], or sitting between two tube openings [81, 102, 107, 108]. The support alters the time evolution of the bridge radius $b(t)$ when $b \approx R_0$ as compared to a free, floating setup, since the drops' initial shapes are distorted from ideal spheres or because translational movement of the drops towards each other is inhibited.

Many researchers argue that at least at early times, or, equivalently, very small bridge radii, the flows opening the neck between the drops are in the Stokes regime, i.e. governed by viscosity and surface tension. Depending on the viscosity of the liquid(s) concerned, this is followed by an inviscid process, governed by capillary forces and inertia.

In the initial viscous regime, the radius of the bridge b is said to increase with time t as $b(t) \sim \frac{\sigma t}{\eta}$, according to a simple scaling argument [81]. The exact two-dimensional solution from [95] predicts a logarithmic correction, such that $b(t) \sim \frac{\sigma t}{\eta} \ln\left(\frac{t}{\tau_{vc}}\right)$, where τ_{vc} is the viscous-capillary time scale $\tau_{vc} = \frac{R_0 \eta}{\sigma}$ as introduced in Eqn. (1.12). It is derived analytically in [79] that the three-dimensional problem at early times is asymptotically the same as the two-dimensional one. This is intuitive: the early opening of the neck, in two dimensions a narrow v-shaped structure with a sharp tip, will be governed locally by the Laplace pressure due to this sharp tip. The large curvature of the tip will be much more important in driving capillary flows than the smaller curvature of the interface around the liquid bridge in the third dimension. This 2D-3D similarity is widely accepted in the literature and hence the three-dimensional bridge opening process is said to be governed by $b(t) \sim \frac{\sigma t}{\eta} \ln\left(\frac{t}{\tau_{vc}}\right)$ [79].

Recent experimental studies however find that in the Stokes regime the neck opening

dynamics follows

$$\frac{b(t)}{R_0} \sim \frac{\sigma t}{\eta R_0} = \frac{t}{\tau_{vc}} \tag{3.3}$$

[81, 102, 104], not confirming the logarithmic correction. It is argued in [101] that this disagreement between theory and experiment may be a result of the asymptotic nature of the theoretical predictions, which hold only in the limit $b \ll R_0$. Gross et al. find using lattice Boltzmann simulations, and argue from a simple scaling argument, that $b(t) \sim R_0 \left(\frac{t}{\tau_{vc}}\right)^{1/2}$ [101]. For 2D and 3D simulations, their data sets collapse after non-dimensionalising with the viscous time scale, implying the viscous-capillary regime. Moreover, their $Re \approx 0.01 \ldots 0.4$ suggests further that the coalescence process happens in the regime dominated by viscous and capillary effects. The square-root scaling with time they find is, however, in stark contradiction to other theoretical predictions and experiments [81, 102, 104].

Yao and co-workers propose an exponential scaling to fit their data [109], which contradicts Eggers' proposed scaling from [79]. However, Yao et al. acknowledge that their data is not in the range of early coalescence, i.e. $b \ll R$ and $t \ll \tau_{vc}$.

When flows are in the inertial, inviscid regime, bridge dynamics is theoretically predicted to be of the form $b(t) \sim t^{\frac{1}{2}}$ [79, 98], with [79] and [101] giving

$$b(t) \sim \left(\frac{R_0 \sigma}{\rho}\right)^{1/4} t^{1/2}, \qquad \frac{b(t)}{R_0} \sim \left(\frac{t}{\tau_{ci}}\right)^{1/2}, \tag{3.4}$$

from a simple scaling argument in two dimensions. These findings are well accepted and also experimentally well confirmed [81, 99, 102, 103, 104].

A challenge however is posed by the problem of droplets coalescing whilst sitting on a surface. Here, analytical solutions are not accessible, as the problem is made more complicated by contact line movement. Essentially, the droplets not only have to form a bridge between them, they also have to slide their mass across the surface they sit on to form the new droplet.

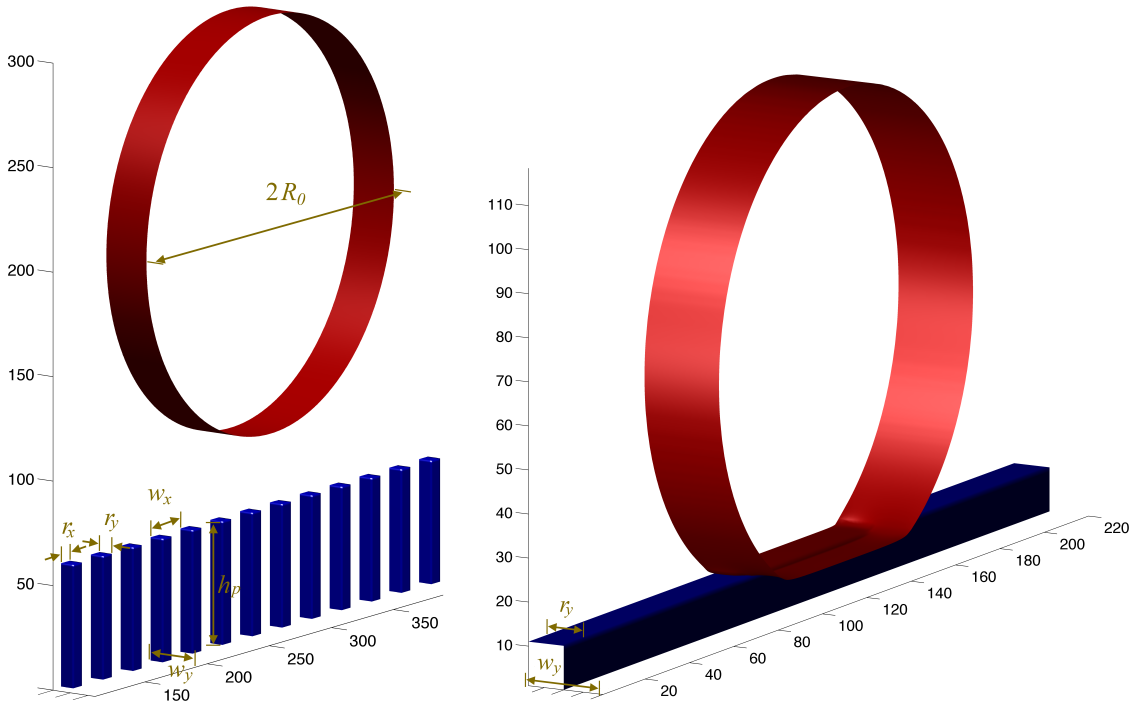
Movement of the contact line is itself an issue of much discussion as it contradicts the no-slip boundary condition commonly accepted to govern liquid-solid interactions. The

current approach to resolving this contradiction is to introduce evaporation/condensation near the moving contact line to facilitate movement [82, 110, 111] or to assume finite slip near the interface [112, 113, 114].

For the early, viscosity-dominated, coalescence process, theory predicts that the bridge-opening movement vertical and parallel to the solid surface follows different laws: $b_\perp(t) \sim \frac{t\theta_Y^2\sigma}{\eta}$ and $b_\parallel(t) \sim \left(\frac{R_0 t\theta_Y^2\sigma}{\eta}\right)^{\frac{1}{2}}$, respectively [83]. The difference is intuitive as $b_\parallel$ requires the contact line to move along the surface (assuming that the contact angle is not too big so that the bridge that is forming is in contact with the surface). These theoretical predictions are confirmed reasonably well in [83]. Later in the process, when $b_{\perp,\parallel} \approx R$, the dynamics are experimentally found to be slower [83], following an exponential growth similar to the scaling in [109]. Subsequently, relaxation of the now elliptically elongated drop to a spherical cap shape is found to be a very slow process, up to 10^7 times slower [82, 83] than bulk hydrodynamics predicted by the viscous-capillary relaxation time $\tau_{vc} = \frac{R\eta}{\sigma}$. The researchers assign this to an assumed strong dissipation occurring during the motion of the contact line which they believe comes from a gas-liquid phase transition at the liquid-gas interface near the solid surface [82, 106].

The distinction between the viscosity-limited and the inertia-limited regimes, i.e. the viscous-capillary and the capillary-inertial regimes, respectively, can be done by considering the characteristic length scales. The length scale on which viscosity dominates is $\ell_\nu = \eta^2/(\rho\sigma)$, Eqn. (1.13). For water ℓ_v is about 10 nm (1.38×10^{-8} m [115]). Note that this length scale corresponds to Boreyko's theoretical critical radius in [77]. Similarly, in the literature the Reynolds number, Eqn. (1.9), is used to characterise whether a hydrodynamic process is viscosity- or inertia-limited. The Ohnesorge number $Oh = \eta/\sqrt{\rho\sigma L}$ characterises the balance of viscous forces with inertia and capillary forces. Besides $Re \gg 1$, $Oh \ll 1$ is also used in the literature to characterise capillary-inertial processes.

For the problem of coalescing drops there exist controversial views in the literature as to what the appropriate length scale L used for the dimensionless numbers Eqn. (1.9) should be, and, equally, to what length scale ℓ_v should be compared. Some researchers



(a) **(b)**

Figure 3.4: Quasi-2D simulation geometry, showing (a) an unperturbed cylindrical drop of radius R_0 above a substrate patterned with posts and (b) the drop interacting with a 3D substrate, comprising ridges in the x direction.

use the radius b of the forming bridge whereas others suggest the width of the tip of the v-shaped neck, $\sim b^2/R$, as a more appropriate length scale [98, 102]. We will address this point in connection with our simulation results in Sec. 3.4.1.

3.3 Lattice-Boltzmann Simulations

In this section we present the simulations we performed to access surface related aspects of coalescence-induced jumping and to study aspects of energy conversion and dissipation in coalescing drops. We will first describe the general geometric setup of the bouncing process and then the initial conditions specific to the coalescence problem.

3.3.1 Geometry

We performed quasi-2D lattice Boltzmann simulations using a binary model, in which both phases have the same density, but different viscosities, as described in Ch. 2. Drop coalescence experiments are naturally three-dimensional, but for our numerical simulations we restricted ourselves to two dimensions for reasons of computational feasibility. However, three-dimensional surface features, such as posts or parallel ridges, can be accounted for if a quasi-2D geometry is used. An example of such a geometry is shown in Fig. 3.4a. The drop has a spherical cross-section in the x-z-plane and is translationally invariant in the y direction, giving it a cylindrical shape when unperturbed by a surface. When the drop comes in contact with a patterned surface, it can interact with the three-dimensional features of the surface pattern, permitting flow in the y direction and the possibility of pinning as for a three-dimensional situation. An example of a drop interacting with a quasi-2D surface is shown in Fig. 3.4b for a ridge in the x direction.

We considered three different substrate types: (i) a rectangular lattice of square posts of side lengths r_x, r_y, arranged with lattice constants w_x and w_y along the x and the y direction, respectively, as depicted in Fig. 3.4a, (ii) rectangular ridges of width r_y and center-to-center spacing w_x which run along the x direction, i.e. parallel to the direction of coalescence, as shown in Fig. 3.4b, and (iii) ridges of width r_x and spacing w_x which run in the y direction, i.e. perpendicular to the direction of drop coalescence. This setup can be simulated in two dimensions (assuming a cylindrical drop) as flow in x direction within the substrate is not possible anyway.

For the surfaces (i)-(iii) the substrate was set up without a base, to permit efficient motion of the gas phase underneath the drop. The height of the structure h_p was in each case chosen sufficiently large that the liquid penetrating the structure would not reach the bottom end of the solid features.

Besides coalescence on substrates with different topologies we also ran simulations of drop coalescence in free space, without a supporting substrate. These simulations were done in two dimensions. Their purpose is three-fold: Firstly, they are used to

determine whether a distinct regime, viscous-capillary or capillary-inertial, is realised in our parameter range. Secondly, the free coalescence simulations serve as a proof of principle to show that known results for coalescence are achieved with our algorithm. Thirdly, they serve as a comparison to the coalescence process on a substrate, and help to quantify the effect of a supporting substrate.

In the substrate and free coalescence cases, and both for two-dimensional and quasi-2D simulations, periodic boundary conditions were applied in the x, y, and z directions.

3.3.2 Initial Conditions

Because the lattice Boltzmann algorithm leads to a diffuse interface, special attention had to be paid to the initial setup of the two droplets. In a typical lattice Boltzmann simulation with a binary phase, a single drop is normally set up with a sharp boundary between the two phases $\phi = \pm 1$ at the initial simulation step $t_{\text{sim}} = 0$. The interface then relaxes into its equilibrium configuration, resulting in a tanh shape of width ξ. This equilibration process takes a certain time depending on the simulation parameters. However, in our problem, where two droplets interact with each other, this relaxation process would occur at the same time as the actual physical motion of the interface as the liquid bridge opens. This leads to two problems: On the one hand, the coalescence dynamics is obscured by the relaxation dynamics. On the other hand, we are interested in dissipation phenomena, and to reliably measure the local dissipation, the equilibration processes need to have finished.

Therefore, the initial conditions for our coalescence problem is chosen as follows: Initially, we use a simulation box of $L_x/2 \times L_y \times L_z$. At $t_{\text{sim}} = 0$ a single drop, which would have an undisturbed radius R_0, is placed on the surface, in a shape that reflects the Cassie-Baxter contact angle for the given surface. The drop is positioned such that its maximum extension to the right is at $L_x/2$. This drop is left to equilibrate until $t_{\text{sim}} = t_{equil}$. Then, the x dimension of the simulation box is doubled, to L_x, and a mirror-image of the drop is placed in the second half of the simulation box. Due to the

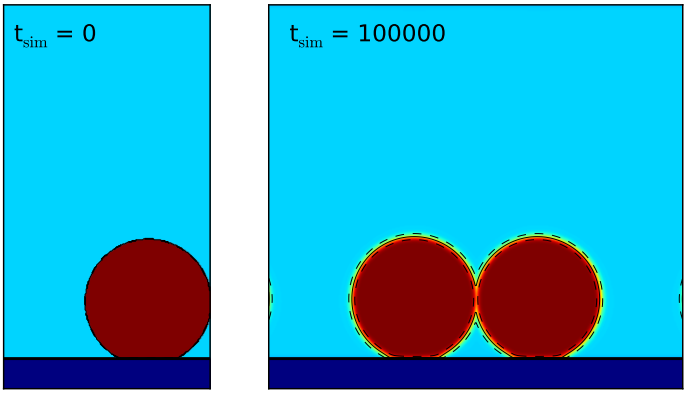


Figure 3.5: Initial conditions (left) and the duplicated simulation box showing the individual equilibrated drops (right) at $t_{\text{sim}} = t_{equil}$. In this picture, and in all that follow, the solid line denotes the liquid-gas boundary, and the dashed lines indicate the extension of the diffuse interface.

initial positioning of the drop, the interfaces of the two drops touch upon doubling the system. Therefore for $t_{\text{sim}} > t_{equil}$ the coalescence process starts, merging two equilibrated single drops.

3.3.3 Simulation Parameters

Lattice Boltzmann simulations were run to gain insight into several problems. We studied the coalescence process of drops in free space, i.e. without a surface, we addressed how different types of surfaces affect jumping upon coalescence, and we studied how the ability to jump upon coalescence depends on the drop size. We now explain the different simulations. A summary of the parameters used is given in Table 3.1.

	R_0	η_l	η_g	σ	ξ	ϕ_a	θ_Y
surface geometries	60	0.3/3	0.01/3	0.0189	2.83	0.2	$105^\circ \ldots 150^\circ$
θ_Y dependence	40	0.3/3	0.01/3	0.0189	2.83	0.2	$105^\circ \ldots 150^\circ$
free drops	$40 \ldots 200$	0.5/3	0.05/3	0.0462	5.77	–	–
size dependence	$40 \ldots 130$	0.5/3	0.05/3	0.0462	5.77	0.24	120°

Table 3.1: Liquid and surface parameters for the coalescence simulations. R_0 – unperturbed radius of the initial drops, $\eta_{l,g}$ – viscosity of the liquid and the gas, respectively, σ – liquid-gas surface tension, ξ – interface width, ϕ_a area fraction of the surface, θ_Y intrinsic contact angle of the surface.

3.3.3.1 Free Coalescence

For the free drop coalescence simulations the drop size was varied from $R_0 = 40$ to 200 lattice units. The simulation box was adjusted in size to accommodate the drop size. This was done to give the merged drop enough space to expand without being affected by its images resulting from the periodic boundary conditions. However, care had to be taken that the simulation box was not too large, because of the inertia of the gas phase. Any drop interface motion has to accelerate the gas phase as well, so an increase of the amount of gas phase relative to the energy provided by the drop's interface would have affected the dynamics. The size of the 2D simulation box was chosen as $L_x/2 = 2R_0 + 40$ lattice units, $L_y = \sqrt{2}(2R_0) \times 3 + 30$ lattice units. Using $\kappa = 0.1$ and $A = 0.024$, the width of the diffuse interface was $\xi = 5.77$, a value large enough that spurious dissipation would be small (see Ch. 2.3.3). The choice of κ and A resulted in a surface tension of $\sigma = 0.0462$. The viscosities of both phases, for $\tau_l = 1$ and $\tau_g = 0.55$, were $\eta_l = 0.5/3$ and $\eta_g = 0.05/3$, respectively. This gives a relatively small viscosity ratio of $\frac{\eta_l}{\eta_g} = 10$, which leads to viscosity effects in the gas which must be accounted for. However, these parameters allow a reliable measurement of the local dissipation. t_{equil} was chosen very large, $t_{equil} = 10^5$, so that equilibration, which depends on the system size, does not affect any scalings of measured values with drop size.

3.3.3.2 Comparison of Surface Geometries

In all simulations involving substrates the surface features were chosen larger than the interface width $\xi = 2.83$, using $A = \kappa = 0.02$, which gave a surface tension of $\sigma = 0.0189$. We studied the coalescence process of drops on ridges along the y and x direction of width $r_{x,y} = 4$ and spacing $w_{x,y} = 20$. Additionally, oblong posts were used with sizes of (r_x, r_y)=(4,6), and (6,4) in lattices of measures (w_x, w_y)=(10,12). Therefore, all the surfaces had the same area fraction $\phi_a = 0.2$ to make them comparable. The intrinsic contact angle was varied from $\theta_Y = 105°$ to 130° to find the θ_Y value at which coalescence leads to jumping, $\theta_{Y,j}$.

3.3.3.3 Size Dependence

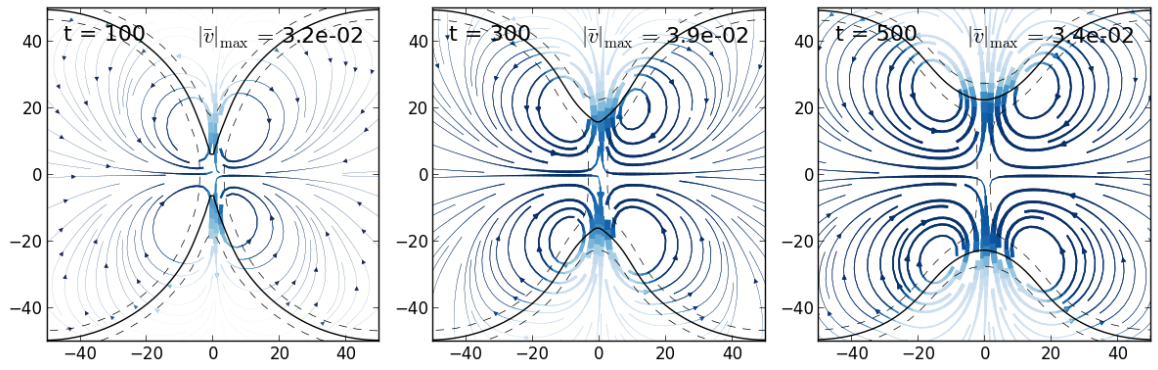
As will become clear in Sec. 3.6.2, the different surface geometries we use affect the ability to jump, as well as the contact angle. To avoid the effect of pinning, which cannot be quantified exactly, we use a surface of ridges along the x direction to study the dependence of jumping on R_0. On x ridges, jumping is most likely, as will be shown in Sec. 3.6.2. The width and lattice constant of the ridges were $r_y = 6$ and $w_y = 25$, respectively.

3.4 Free Coalescence in Two Dimensions

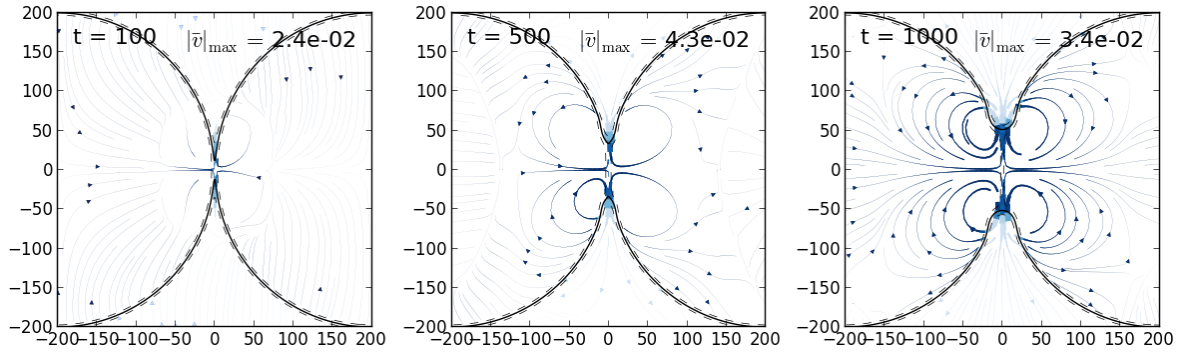
In this section, we will study coalescence of droplets in two dimensions using lattice Boltzmann simulations. Lattice Boltzmann has previously been used [101], but only for the viscous regime, and only for the early bridge opening process. We are interested in the regime where inertia and capillary forces dominate the dynamics, because ultimately, the findings for free coalescence in this section are intended to aid in the understanding of the self-propelled jumping process on surfaces which we will discuss in Sec. 3.5. For self-propelled jumping upon coalescence, the process needs to be approximately inviscid, as the experimental results in [77] suggest.

3.4.1 Viscous or Inertial Regime in Simulations

The first question we are striving to answer is whether the coalescence processes studied in our simulations are in the Stokes regime, i.e. dominated by viscous shear flows, or in the Euler regime, i.e. inviscid. The overall process of coalescence can be characterised by the Ohnesorge number for drops of a given radius, $Oh = \eta/\sqrt{\rho\sigma R_0}$. The values are $Oh = 0.11 \ldots 0.055 \ll 1$ for the range of radii used in our simulations, suggesting that the process overall is governed by inertia, and not viscous shear, competing with capillary forces. However, for the initial bridge-forming process smaller length scales than R_0 are the relevant ones, so it is necessary to determine whether early on in the process we might observe viscous behaviour.



(a)



(b)

Figure 3.6: Streamline plot of the velocity field of coalescing free drops with (a) $R_0 = 50$ and (b) $R_0 = 200$. The solid line denotes the liquid-gas boundary, the dashed lines indicate the extension of the diffuse interface, with width $\xi = 5.77$. The colour of the stream lines reflects the phase, dark blue corresponds to the liquid phase. The thickness of the stream lines is a measure of the magnitude of the velocity, the maximum value is given in each frame. Shown is only the relevant part of the simulation box, its actual size was as described in Sec. 3.3.3.1.

One indicator is the viscous length scale ℓ_v according to Eqn. (1.13). Inserting the relevant parameters, the viscous length scale of our lattice Boltzmann simulations for free drop coalescence becomes $\ell_v = (0.5/3)^2/(0.0462 \times 1) = 0.6$ lattice units. $\ell_v = 0.6$ is smaller than the scale of our simulation lattice (i.e. 1), and certainly smaller than any physically meaningful length scale, as we will discuss below.

Other indicators are the Reynolds number and the Ohnesorge number. As discussed in Sec. 3.2, for the bridge opening process there are controversial views in the literature about the appropriate length scale needed to calculate the either dimensionless number: the bridge radius b or the width of the tip of the v-shaped neck, $\sim b^2/R_0$. This author supports the latter, for looking at the flow field of the opening bridge between the droplets, shown in Fig. 3.6, in our simulations the strongest flows occur in a very localised region around the tip of the v. This suggests that the distance to the tip's counterpart at the opposite side of the liquid bridge cannot be the characteristic length scale of the bridge opening process.

To obtain a value for b^2/R_0 one has to consider what bridge sizes are physically meaningful when a diffuse interface is considered. As discussed in [101], the radius of curvature $b^2/(2R_0)$ of the neck has to be $\gtrapprox \xi$, as well as $b \gg \xi$. Together these conditions yield a minimum meaningful bridge radius of

$$b_{phys} \gtrapprox \sqrt{2\xi R_0}. \tag{3.5}$$

For drops of $R_0 = 50$ with an interface width of $\xi = 5.77$ this means $b_{phys} \approx 25$. For $R_0 = 200$ Eqn. (3.5) gives $b_{phys} \approx 50$. The third panel in Fig. 3.6a and Fig. 3.6b, respectively, shows the flow field of bridge opening when $b \approx b_{phys}$. From the velocities given in the plots we find $Re \approx 2.5$. Together with the fact that $\ell_v = 0.6 < b^2/(2R_0) \approx 12$ and $Oh = 0.23 < 1$ we can conclude that the viscous regime is inaccessible in our simulations for physically meaningful bridge radii. Hence, even at an early stage of the coalescence process, the flows in our simulations should not be dominated by shear flow. Yet, $Re \gtrapprox 1$ and $Oh \lessapprox 1$ suggest that we are not in the purely inertia-governed regime

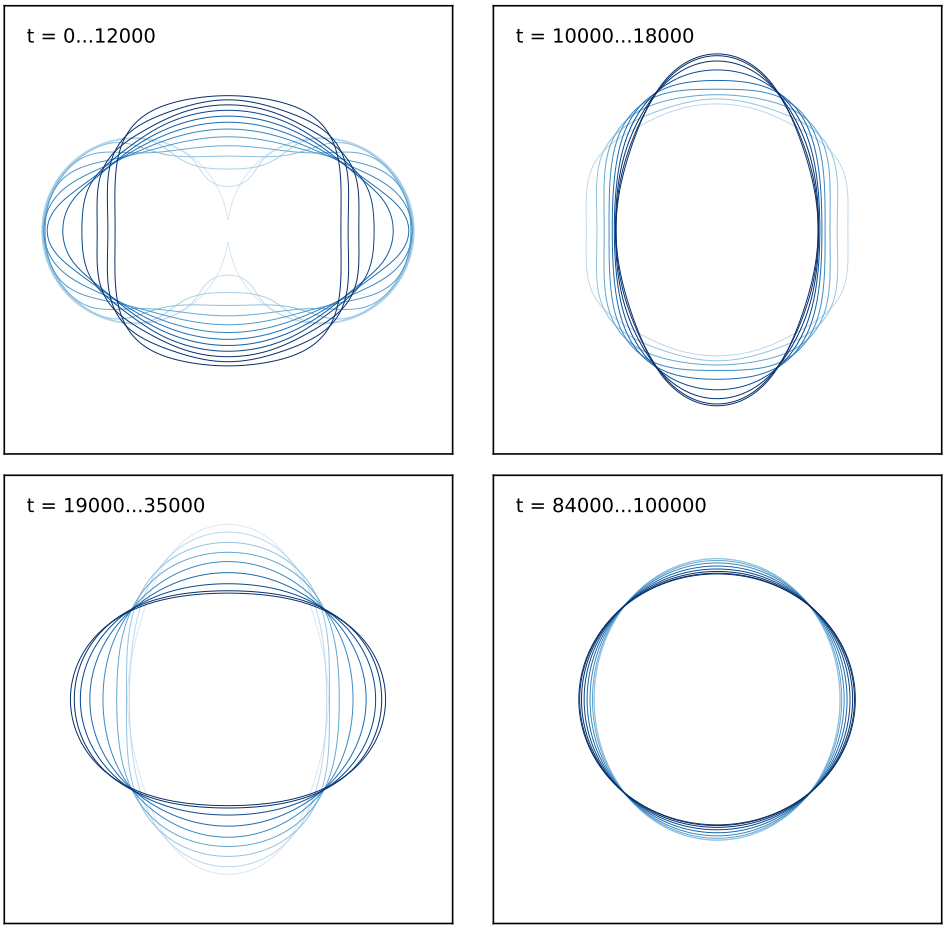


Figure 3.7: Evolution of the drop shape starting from the coalescence of two single drops. The time runs from light to dark shades in each panel. The example is for $R_0 = 100$.

either, and viscosity will play some role, at least during the bridge-opening process.

In the following section we will ascertain whether the capillary-inertial regime is observed with our parameters and whether the $b \sim t^{1/2}$ growth law seen in experiments is confirmed by our simulations.

3.4.2 Coalescence Process

In this section we will address the evolution of the liquid bridge with time. Experimental and previous theoretical work on coalescence predominantly studied the initial bridge opening process with $b \ll R_0$, as described in Sec. 3.2. With our lattice Boltzmann simulations the bridge-opening process of two coalescing droplets is easily accessible, especially for $b(t) \lessapprox R_0$ and $b(t) > R_0$.

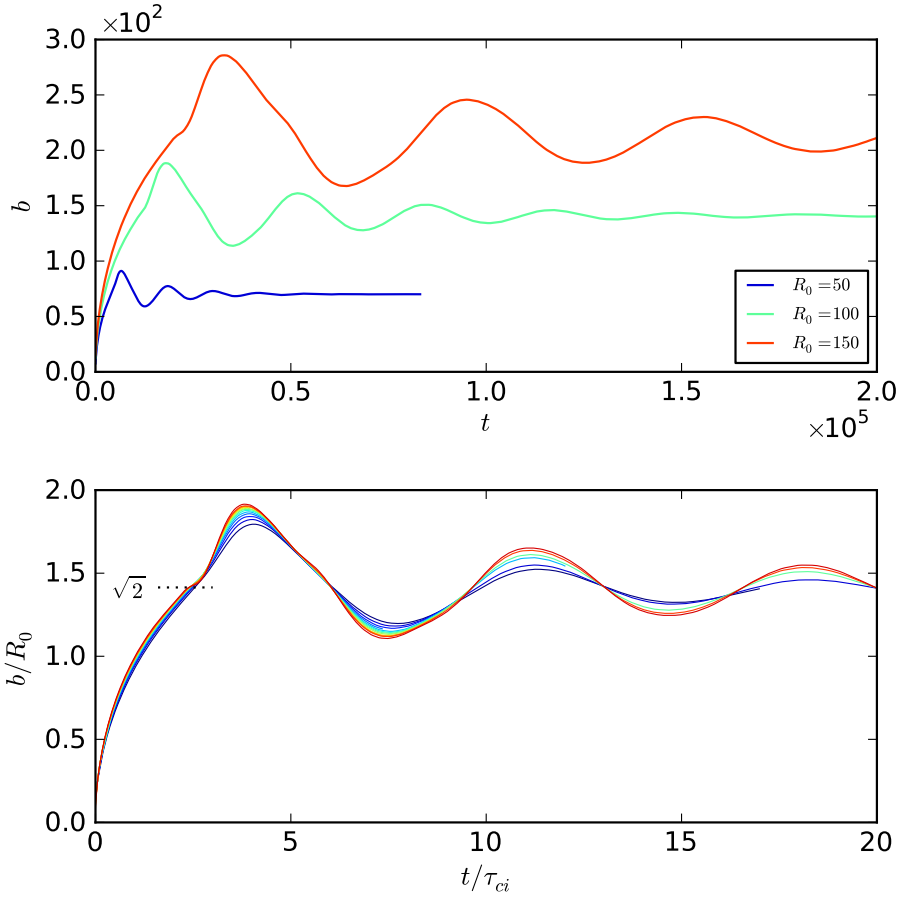


Figure 3.8: Variation of the bridge ridge radius b with time. Top: for three different radii of the initial droplets. Bottom: Non-dimensionalised b and t for $R_0 = 40 \ldots 200$ (blue to red lines).

To access the size of the bridge forming between the two drops we record the width of the liquid phase at the axis of symmetry (or rather at the nodes next to the axis of symmetry as the axis itself sits half way between two lattice nodes due to the duplication approach). Continuous values for $b(t)$ are found by linearly interpolating between the last node that sits within the liquid phase (i.e. has $\phi > 0$) and the first node that is in the gas phase ($\phi < 0$).

Note that [79] showed that the early stage of coalescence can be treated as a two-dimensional problem, whereas here we treat the entire process in two dimensions. The simple scaling law Eqn. (3.4) derived in [79] was only found for the two-dimensional case, implying the condition $b \ll R_0$ for 3D experiments.

The early stage of bridge-opening is difficult to access in the simulations. We have

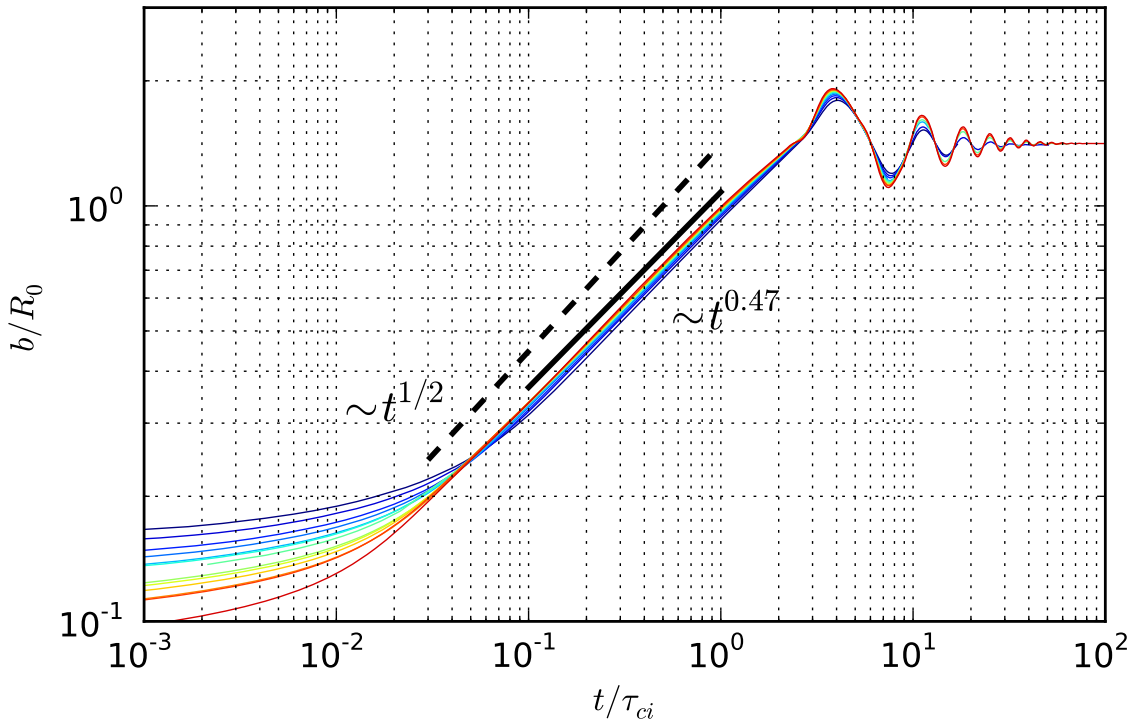


Figure 3.9: Dimensionless bridge radius b/R for drop radii $R_0 = 40 \ldots 200$ (blue to red lines) of the initial droplets evolving over time t scaled by the capillary-inertial time scale τ_{ci}. The solid line represents the slope $\alpha = 0.47$ from fitting all the datapoints between $t/\tau_{ci} = 0.1$ and 1 , corresponding to a growth law $b \sim t^{0.47}$. The dashed lines indicates the expected $b \sim t^{1/2}$ power law.

described already in Sec. 3.4.1 that physically meaningful bridge widths in our simulations are already quite large, on the order of $1/4 \ldots 1/2 R_0$. Additionally, exact placement of the drops such that the water-gas boundary layers, where the order parameter $\phi = 0$, of both drops exactly touch is tricky due to the discreteness of the lattice. Our liquid-gas interface is diffuse and it is chosen to be relatively wide to allow stable simulations and prevent spurious velocities and dissipation. As a result, even when the two drops do not exactly touch, the interfaces of both drops will "see" each other and start merging. On the other hand, overlapping interfaces will effectively start with a finite initial bridge radius. Therefore, the early behaviour of the bridge formation will depend on the initial degree of overlap of the drops.

Fig. 3.7 shows the evolution of the drop shape over time for an initial drop radius of $R_0 = 100$ lattice units. Note how the coalescence process results in a large distortion of

the merged drop, a result of inertia of the initial drops' masses. With time, the distortions evolve into harmonic oscillations of the composite drop, which slowly relax to equilibrium.

In Fig. 3.8, top panel, we plot the evolution of the bridge radius, half the width of the drop along the axis of symmetry in the x direction, with time $b(t)$, for the drop in Fig. 3.7, together with the results for $R_0 = 50$ and $R_0 = 150$. In the bottom panel of Fig. 3.8 we plot how the dimensionless bridge radius b/R_0 for all our simulations varies with dimensionless time. The time is non-dimensionalised by the inviscid time scale τ_{ci}

$$\frac{b(t)}{R_0} = f\left(\frac{\sigma t^2}{\rho R_0^3}\right) = \bar{f}\left(\frac{t}{\tau_{ci}}\right), \tag{3.6}$$

The curves for all radii collapse in this plot, showing that the coalescence process is indeed an inviscid process, governed by capillary forces and inertia. The slight deviation of the curves for the smaller droplets can be explained as a result of the initial conditions: due to overlap of the diffuse interfaces when the simulation box is duplicated, the volume of the composite drop is not exactly twice that of the original drop.

For all drop sizes the bridge radius first grows approximately linear, until it reaches about $\sqrt{2}R_0$, the radius of the combined drop, as indicated in Fig. 3.8. Subsequently, we observe an oscillation of b reflecting the oscillatory motion of the merged drop.

The initial growth is close to the predicted and experimentally observed scaling $b \sim t^{1/2}$. This is confirmed in Fig. 3.9, where we plot the dimensionless bridge radius against the dimensionless time in a double logarithmic plot. The linear behaviour confirms a power law growth $b \sim t^{\alpha}$ (albeit over a short time interval), and the slope gives the exponent α. Fitting the data between $t/\tau_{ci} = 0.1$ and 1 we find $\alpha = 0.47$ with negligible error. This is very close to the predicted $\alpha = 0.5$, which is indicated by the dashed line in Fig. 3.9.

This finding is noteworthy, since the square-root scaling with time has so far only been numerically seen for bridge radii $\ll R$ [98] and experimentally observed for bridge radii that are large, but smaller than the drop radius [81, 99, 102, 104, 109]. Menchaca-Rocha and co-workers [103] measured b up to values larger than the initial drop radius, but their findings for the late stage evolution deviate from $b \sim t^{1/2}$, they find $t^{0.41}$. I think this

deviation may be due to the three-dimensional nature of the experiments, or it may stem from the fact that their experiments were performed with drops sitting on a surface. The surface will for $b \gtrapprox R$ interfere with the merging drop bulging outwards.

In our simulations we observe that the $b \sim t^{1/2}$ growth law still holds until $b \approx \sqrt{2}R_0$, even though the shape at such a late stage is far from "two drops with a bridge between them", as can be seen from Fig. 3.7, top left panel. The last shape displayed in this panel corresponds to $b \approx \sqrt{2}R_0$.

Looking at Fig. 3.8, the oscillations after the initial growth do not look harmonic until later in the process. This is expected due to the strong distortions of the drop. Measuring the time between the curve maxima T_{osc} in Fig. 3.8 we find that they are of order of the capillary-inertial time scale for the merged drop (see Ch. 1.3), $\tau_{ci} = 2^{3/4}\sqrt{\rho R_0^3/\sigma}$. $T_{osc,0} = 4.3\tau_{ci}$ between the first two maxima, and for the subsequent oscillation $T_{osc} = 4.1\tau_{ci}$ ($T_{osc} = 4.2\tau_{ci}$ for $R_0 = 50$). We will use these results later for our study of drop impact in Ch. 5.1.

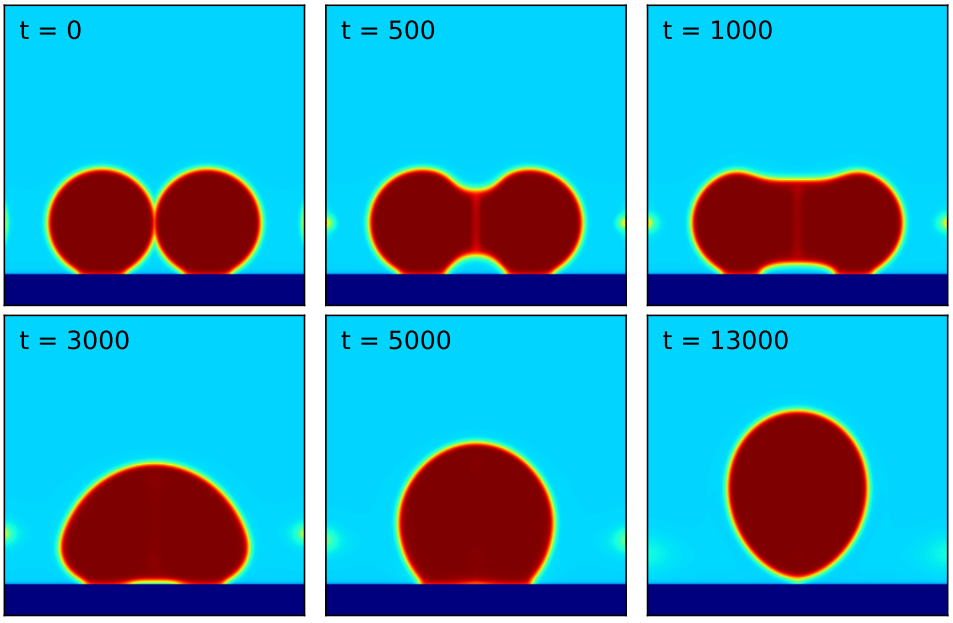
To conclude this section, we predicted, based on the Reynolds and Ohnesorge numbers of the bridge forming process, that the coalescence process should be governed by the competition of surface tension forces and the drops' inertia, but not viscous forces. This prediction was done based on the observation of physically meaningful length scales, which, in our range of drop radii and for the interface width used, ranges from $b \gtrapprox 0.5R_0$ to $b \gtrapprox 0.25R_0$. In this region of bridge radii the inertia-driven character was confirmed by a collapse of all $b(t)$ curves when the time is made dimensionless by the capillary-inertial time scale. Furthermore, we confirmed the theoretically predicted and experimentally observed growth law $b(t) \sim t^{1/2}$, finding a power law exponent of 0.47. After the merging process the drop continues to oscillate with a period scaling with the capillary-inertial time scale, at $T_{osc} \approx 4.1\tau_{ci}$.

3.5 Coalescence on Solid Substrates

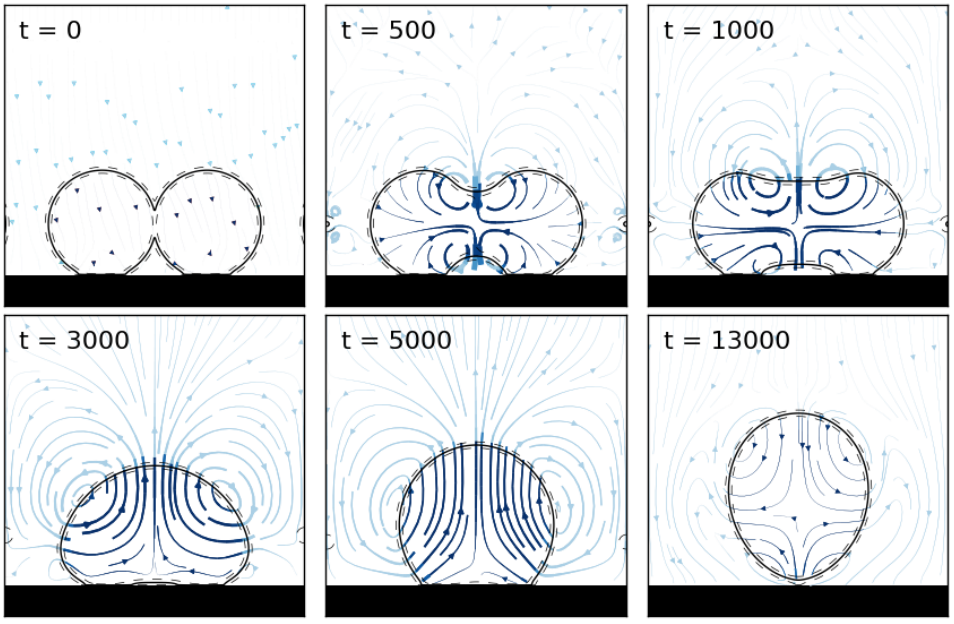
Having studied the coalescence process in free space, in this section we are interested in the effect of a solid substrate. If the coalescing drops are in contact with a surface, the process is no longer symmetric in the x and z directions as it is in free space. Instead, the substrate causes a symmetry breaking in the z direction which may lead to the drop leaving the surface, i.e. jumping. Intuitively, this can be understood as the bottom of the coalescing drop bulging out and pushing off the substrate.

Our lattice Boltzmann simulations, which allow us to model hydrodynamics and include interactions with solid surfaces, are well suited to study this coalescence-induced jumping process. For certain surface and drop parameters the merged drop does indeed jump off the surface. An example of this is shown in Fig. 3.10, for drops of undisturbed radii $R_0 = 50$ coalescing on ridges along the x axis, i.e. parallel to the net drop motion. We show both the evolution of the drop shape by plotting the order parameter field in Fig. 3.10a, and the velocity field in Fig. 3.10b. The time $t = t_0 = 0$ denotes the moment the initial drop is duplicated.

The reader may note that the dynamics of this process of jumping upon coalescence contradicts the assumptions in [87]. In that paper, the authors stated that the merged drop assumes the shape of a spherical cap before starting to retract. Based on this assumption, a dynamic equation for the drop movement was found. Our simulations show that the inertia of the liquid due to the merging process carries through into the receding-and-lifting motion, and therefore should be included into any dynamic model describing the receding motion. In this section we consider general phenomena of the drop detaching mechanism and we discuss the difference to free coalescence. We focus on the detachment process and the jumping velocity in Sec. 3.5.1, and compare our results for the size dependence of jumping to the literature Sec. 3.5.2. After that, in Sec. 3.5.3 we discuss the shape of the drop as it detaches. We will turn our focus to coalescence on different surfaces geometries in Sec. 3.6.



(a)



(b)

Figure 3.10: Coalescence and bouncing process of quasi-2D drops of $R_0 = 50$ on ridges along the x direction ($r_y = 6$, $w_y = 25$). The liquid parameters are those given in Table 3.1 for the size dependence simulations. In (a) the order parameter field of the liquid and gas phase, in (b) the streamlines of the velocity field are shown, for the layer $y = 3$ which cuts through the center of the ridge. The simulation box is was 455 nodes high, here only the lower 280×280 are shown.

3.5.1 Detachment Process and Jumping Velocity

We have discussed the coalescence process for free drops in Sec. 3.4.2. To understand the role interaction with the surface plays in the coalescence process, let us for now consider a surface that is completely hydrophobic, $\theta_Y = 180°$ and therefore does not interact with the liquid apart from providing a barrier from which the merging drop can push off. When the two drops are coalescing the bridge that forms between them bulges out, as we have seen for free drops in Fig. 3.7. This bulging-out motion pushes the drop away from the surface. The acceleration of the bridge is the force pushing the drop off the surface, divided by the mass of the liquid

$$\frac{\mathrm{d}^2}{\mathrm{d}t^2} b(t) \sim \frac{F_{push}(t)}{m}. \tag{3.7}$$

The drop will detach when the pushing force goes to zero, i.e. the drop is not accelerated any further. This means that detachment happens when $\frac{\mathrm{d}}{\mathrm{d}t} b(t)$ is maximal, which is intuitive: At this point the bulging out motion is slower than the drop's acquired velocity and the drop boundary cannot follow the drop's center-of-mass velocity – the liquid surface moves away from the substrate, i.e. the drop detaches. Note that this implies that drop detachment can happen before the drop reaches its maximum elongation, a somewhat counter-intuitive result.

For a process governed by capillarity and inertia, the maximum bridge velocity should scale with the capillary-inertial viscosity, $(\frac{\mathrm{d}}{\mathrm{d}t} b(t))_{max} \sim \nu_{ci} = \sqrt{\sigma/(\rho R_0)}$. This implies that the drop detaches with $v_{jump} \sim \nu_{ci}$.

Our simple argument is confirmed by the results of the original experiments by Boreyko et al. [116]. Their graph for the jumping velocity was given in Fig. 3.3b, and indeed for drop sizes above a certain threshold the dimensionless velocity v_{jump}/ν_{ci} of the jumping drop stays constant, i.e. $v_{jump} \sim \nu_{ci}$. Also Wang's results in [84] confirm $v_{jump} \sim \nu_{ci}$, as Eqn. (3.2) can be written as

$$v_{jump} \sim \nu_{ci} \left(\delta - \epsilon Oh\right)^{\frac{1}{2}}. \tag{3.8}$$

For a capillarity-inertia driven process $Oh \ll 1$, so the expression reduces to $v_{jump} \sim \nu_{ci}$ for sufficiently large R_0.

The discussion so far did not include surface interaction, which will be present for any surface with a finite contact angle. For $\theta_Y < \pi$ detachment of the drop requires an adhesion energy to be overcome. It represents the necessary energy to replace the single liquid-solid interface of width $\sim \sin\theta_{CB}$ with a solid-gas interface of that width and an additional liquid-gas interface. For a two-dimensional drop on a surface of area fraction ϕ_a the adhesion energy is given by

$$W_{adh} = \sigma\sqrt{2}R_0 2\sin\theta_{CB}(\cos\theta_Y + 1)\phi_a. \tag{3.9}$$

for a merged spherical droplet of radius $\sqrt{2}R_0$. It can be understood as the adhesion work acting as a retardation force [87] to inhibit the droplet jumping.

This extra energy for jumping introduces a contact angle dependence to the ability to jump. In the inviscid case, where no energy is lost to dissipative processes, the energy available for the drop to jump is the difference between its initial and merged surface energies, which is approximately

$$\Delta E_S = (2 - \sqrt{2})\sigma 2\pi R_0, \tag{3.10}$$

for high apparent contact angles and in two dimensions. This ΔE_S has to be larger than W_{adh} in order to allow jumping, and any excess energy is turned into kinetic energy of the jumped drop, as we will discuss in relation to the drop shape at detachment in Sec. 3.5.3.

3.5.2 Size Dependence and Dissipation

We performed simulations with varying drop size on ridges parallel to the coalescence motion, aiming to reproduce Boreyko's and Wang's findings for the velocity scaling [77, 84]. The results are given in Fig. 3.11, together with the matching quantities for the free drop coalescence simulations discussed in Sec. 3.4.

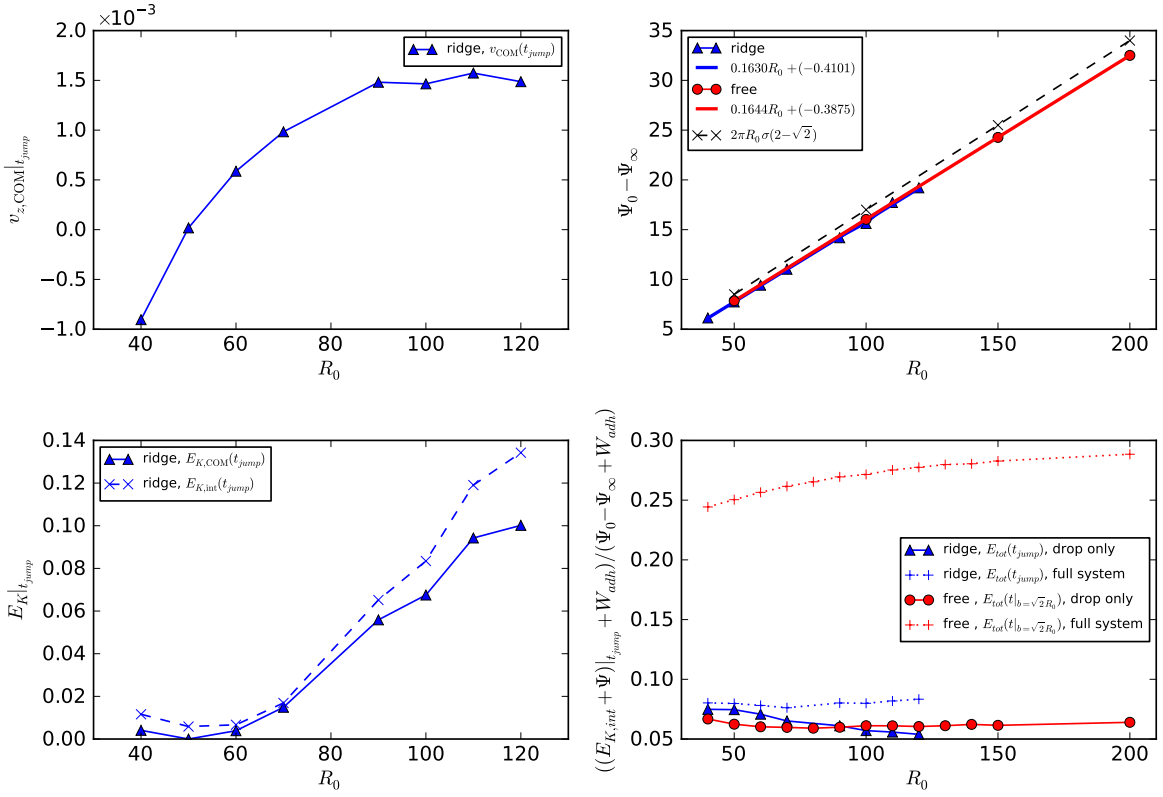
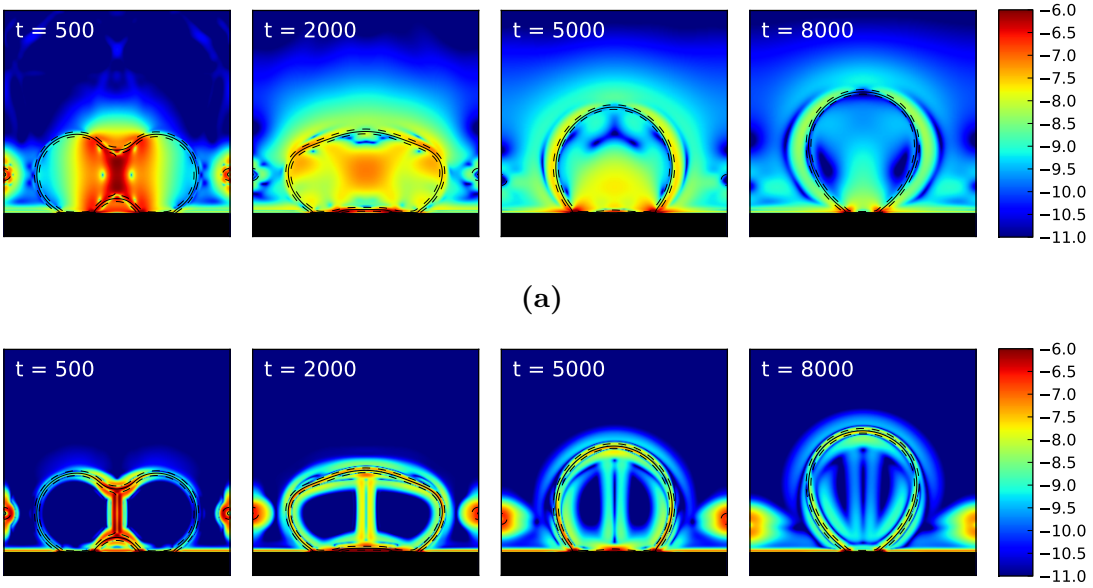


Figure 3.11: Simulation results for the size dependence of the jumping process. Top left: jumping velocity of the drop, bottom left: corresponding kinetic energy of the drop for the internal fluid motion (dotted) and the center-of-mass motion (solid). Top right: the energy available to the drop, corresponding to the change in interface energy. Bottom right: the energy of the liquid drop (solid) and of the entire system (dotted) at jumping, divided by the available energy as a measure of dissipation in the system. All quantities are given in lattice units. The simulation parameters used are listed in Table 3.1.

In the top left panel the jumping velocity is plotted against the initial drop radius. Note that we report a negative jumping velocity for $R_0 = 40$. In this case the contact with the substrate is contracted to zero due to internal upwards flow, but the center of mass of the droplet is actually moving downwards. The drop does not actually leave the surface and therefore the negative velocity is not a physical jumping velocity.

Fig. 3.11 shows that we do not recover the $1/\sqrt{R_0}$ behaviour expected if $v_{jump} \sim \nu_{ci} = \sqrt{\sigma/(\rho R_0)}$. The shape of the curve however corresponds to the initial increase of v_{jump} for small radii that both [84] and [77] observe. This region of increasing v_{jump} with R_0 corresponds to $Oh = 0.037 \ldots 0.017$ in the experiments [77] and $Oh = 0.1 \ldots 0.014$ in the analytical study [84]. For our range of drop radii $R_0 = 40 \ldots 120$ and the



(a)

(b)

Figure 3.12: Local dissipation rate $\frac{\mathrm{d}e}{\mathrm{d}t}(x, y)$ in logarithmic scale, given in lattice units, for drops of $R_0 = 50$ coalescing on a ridge. The $y = 3$ layer cutting though the ridge is given, the simulation box is was 455 nodes high, here only the lower 280×280 are shown. The simulation parameters are given in Table 3.1, for the size dependence simulations.

simulation parameters listed in Table 3.1 the range of Ohnesorge numbers of our system is $Oh = 0.12 \ldots 0.07$. As such, our simulations show jumping at slightly higher Ohnesorge numbers than the critical Oh found in experiments. However, the simulation results given here describe the jumping process on ridges in the x direction, whereas the substrate in [77] was a pillar surface. We will show in Sec. 3.6 that ridges along the x direction, parallel to the coalescence motion, facilitate jumping more easily than post surfaces.

In the bottom left panel of Fig. 3.11, we plot the kinetic energy of the drop at the moment of detachment. Both the energy of the center-of-mass motion $E_{K,\mathrm{COM}}$, and the internal kinetic energy $E_{K,int}$, which is kinetic energy at each lattice node, summed over the volume of the drop, are shown. The deviation between the two indicates that there are additional flows within the drop, in addition to the lifting velocity of the drop.

The free energy $\Psi(t)$ of the system is the sum of the bulk, interface, and surface free energy contributions. By taking the difference between initial free energy $\Psi_0 = \Psi(t = 0)$ and the free energy after equilibration of the system $\Psi_\infty = \Psi(t \to \infty)$ we obtain the

interface energy difference between the initial two droplets and the merged droplet floating above the surface after jumping, which, assuming no dissipation, is the energy available to the drop for jumping, minus the adhesion energy required for drop detachment. $\Psi_0 - \Psi_\infty$ is plotted in the top right panel of Fig. 3.11.

As expected, it scales linearly with the drop radius, and is close to the approximate surface energy difference $\Delta E_S = 2\pi\sigma(2-\sqrt{2})R_0$ between a merged drop and its initial droplets of R_0. $\Psi_0 - \Psi_\infty$ is plotted for a drop on a surface and a free drop. The results for the free drop and the drop on a ridge are very similar, which is due to the high apparent contact angle of 154° on the ridge surface. The slight shift against the ideal linear curve is presumably due to initial conditions. Part of the interface energy of two separate drops is not available to the composite drop due to overlap of the interface.

Our relatively high Ohnesorge numbers of $Oh = 0.12 \ldots 0.07$ mean that despite jumping being possible there is still considerable dissipation. To get an estimate of the importance of dissipation we plot the energy at the moment of drop detachment, $(\Psi + E_{K,int})|_{t_{jump}}$, plus the adhesion energy $W_{adh} = \sigma\sqrt{2}R_0 2\sin\theta_{CB}(\cos\theta_Y + 1)\phi_a$, over the available energy plus the adhesion energy, for both the drop's internal kinetic energy only (solid lines), and the kinetic energy of the entire system (dashed lines) in the bottom right panel of Fig. 3.11. This way we can access the the energy of the drop as if it was sitting on the surface just before detaching. In an ideal inviscid system $(\Psi + E_{K,int})|_{t_{jump}} + W_{adh}$ would be equal to the difference between the surface energy between of two single and one merged drop sitting on a surface, $\Psi_0 - \Psi_\infty + W_{adh}$. As our system is not inviscid we expect the ratio of both quantities to be smaller than one.

We also include the results from the free drop simulations for the same fluid parameters, to see if interaction with a wall has an effect on the dissipation. For free coalescence, the event corresponding to the jump on a surface is the bridge width reaching $\sqrt{2}R_0$, as will be explained in Sec. 3.5.3.

Plotting the energy ratio reveals three things: firstly, the dissipation is strong in the parameter regime used for our simulations. For the free drop simulations, only $\approx 30\%$ of the available energy is left in the entire system at the moment the composite drop begins

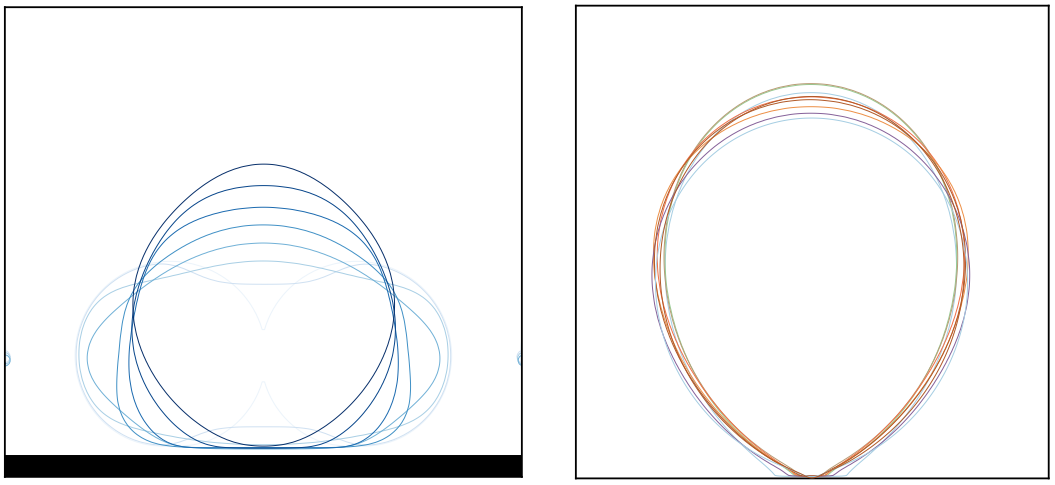
to oscillate. This is because the initial bridge opening process is associated with strong viscous dissipation. Secondly, dissipation is much higher in the presence of a solid wall, as in the case of drop coalescence on a ridge only $\approx 8\%$ of the initial energy remains in the entire system, whereas for the free drop 30% of the available energy is left.

Both these points are confirmed in Fig. 3.12, where we plot the local dissipation rate $\frac{\mathrm{d}e}{\mathrm{d}t}(x, y)$ from viscous shear and diffusion for different time steps. It is clear that the bridge opening process gives the main contribution to the overall dissipation. Later in the process the local dissipation rate is several orders of magnitude smaller than initially in the volume between the original drops. Additionally, it can be seen that there is both dissipation from viscous shear and dissipation from diffusion associated with the motion of the contact line as the drop lifts. This why the overall dissipated energy is larger for a drop on a substrate than for the free coalescence.

As a third remark, we observe that the energy ratios plotted in Fig. 3.11 for the entire system are much higher than for the drop only. In the graphs for the liquid contribution, only the kinetic energy of the drop enters the ratio, whereas otherwise the kinetic energy of the liquid and the gas are taken into account. Therefore we can conclude that the surrounding liquid carries a significant amount of kinetic energy. This is because the density of the gas phase is equal to that of the liquid phase, both are unity. Any liquid motion also moves the gas phase which therefore acquires kinetic energy.

3.5.3 Drop Shape at Detachment

Having considered jumping velocity in Sec. 3.5.1, in this section we discuss the shape of the drop as it detaches from the surface. We argued from Eqn. (3.7) that the drop detaches when $\frac{\mathrm{d}}{\mathrm{d}t}b(t)$ is maximal. From our discussion of the evolution of the bridge radius with time, shown in Fig. 3.8, we know that $\frac{\mathrm{d}}{\mathrm{d}t}b(t)$ shows an increase just after $b(t)$ reaches $b \approx \sqrt{2}R_0$, at the beginning of the drop oscillations. This behaviour was universal for all the curves $b(t)$ for different radii. Therefore we know that the drop detaches at $b \approx \sqrt{2}R_0$, i.e. when the drop is approximately spherical. In Fig. 3.13a this is confirmed



(a) **(b)**

Figure 3.13: Shape of the droplet as it detaches. (a) Coalescence and jumping of a drop on an ideally de-wetting ridge surface with $\theta_Y = 180°$. (b) Drop shape at detachment for various contact angles on a ridge in the x direction, and drop sizes of R_0 =40, 50, 100 (scaled).

for coalescence on a ridge surface with $\theta_Y = 180°$. As the drop detaches it has a slightly elliptical shape, but its horizontal radius is $0.99\sqrt{2}R_0$.

As these considerations are universal for all drops, the almost spherical shape must be independent of the drop and liquid parameters. This universality is confirmed in Fig. 3.13b where we plot the drop shape just before detachment for drops of $R_0 = 40$ and different $\theta_Y = 100° \ldots 150°$ on a ridge in the x direction with $r_x = 4$ and $w_x = 20$, and drops of $R_0 = 50$ and 100 on an identical substrate at $\theta_Y = 120°$ with different liquid parameters listed in Table 3.1. All drops have the same balloon-like shape of lateral radius $\alpha\sqrt{2}R_0$, with $\alpha = 0.92 \ldots 0.99$. Slight deviations can be seen for the drops that have a wider base width, those drops do not actually detach due to their low contact angle.

The shape of the drop just before detaching is not a perfect ellipse of low eccentricity, but has a slightly asymmetric shape that brings to mind a child's balloon. The balloon-like character of the shape is due to the pinch-off of the liquid as the drop detaches. This is a result of the finite contact angle which requires the interface of the drop to distort in order to form an angle $\theta < \theta_r$ before detaching, where θ_r is a 2D version of the Cassie-Baxter

angle Eqn. (1.7), as will be discussed in Sec. 3.6.2.

We conclude this section by summarizing our findings. Any drop that detaches will detach in a given balloon-like shape of the same relative width for all drops. Therefore it will have a certain fixed surface energy $E_S|_{t_{jump}} \sim \sigma R_0$ which is approximately $2\pi\sigma\sqrt{2}R_0$. If the coalescence motion is inviscid, the detachment velocity is $v_{jump} \sim \nu_{ci}$ which means $E_K|_{t_{jump}} \sim \sigma R_0$ as well. Therefore, the initial surface energy will always be distributed in the same fraction amongst surface energy of the jumping drop and kinetic energy, with most of the excess energy between a two small and the single large spherical drop being turned into kinetic energy of jumping. If surface interactions or viscous dissipation inhibit the coalescence motion in some way, the drop may still detach in the same balloon-like shape with $E_S|_{t_{jump}} \sim \sigma R_0$. The kinetic energy however is reduced, as we saw in Fig. 3.11, where the jumping velocity did not reach ν_{ci} as it would have in the inviscid case.

3.6 Comparison of Surface Geometries

In this section we will discuss how the properties of the solid surface affect whether a coalesced drop can jump off the surface. We expect that the area fraction ϕ_a of the surface and its contact angle affect the ability of the drop to jump [87], as discussed in Sec. 3.5.1.

Let us first consider the surface with ridges in x direction. As explained in Sec. 3.5.1, solving $W_{adh} = \Delta E_S$ for θ_Y should give the critical contact angle for jumping. $W_{adh} = \Delta E_S$ from Eqn. (3.9) and Eqn. (3.10), respectively, for our parameters in Table 3.1 and Table 3.2, yields no solution, which implies that the drop should be able to jump at any contact angle, within the approximation of high apparent contact angles. However, the equality $W_{adh} = \Delta E_S$ is only valid for the inviscid case. We know from Sec. 3.5.2 that due to dissipation in our system only a small fraction of the available energy remains before the drop can detach. If one assumes that 10% of the available energy are left this yields $\theta_{Y,j} = 87°$. We observe $\theta_{Y,j} = 113°$ on a surface made of ridges along the x direction, which implies that only 4.5% of ΔE_S are left to facilitate the detachment process. However,

this is only a rough estimate, in fact we expect the dissipation to be dependent on the contact angle.

We are interested in the effect of different surface types on the jumping process: ridges in the x direction, in the y direction, and rectangular posts whose longer side is parallel to the x or the y direction. Recall that the drops move along the x direction when coalescing, we are interested in the question whether the directionality of the surface features has any influence on the coalescence process. For each geometry the area fraction is kept the same, $\phi_a = 0.2$, the specific parameters are given in Table 3.2. For a given geometry, we quantify the ability to jump by varying the intrinsic contact angle and recording for which values $\theta_Y \geq \theta_{Y,j}$ jumping can be seen. In the following sections we present examples of the coalescence-induced jumping process on the different surface types and give an intuitive explanation of the observed results. Further details on the mechanisms involved are studied thereafter in Sec. 3.6.3.

3.6.1 Examples

In Fig. 3.14 we compare the coalescence process for the different geometries given in Table 3.2 at the same intrinsic contact angle of $\theta_Y = 114°$. As can be seen in Fig. 3.14a, on the ridges in the x direction the drop jumps. It also jumps on the substrate with $r_x = 6 > r_y = 4$ (posts 1), as shown in Fig. 3.14b. For the post structure where the posts are oriented in the opposite direction, $r_x = 4 < r_y = 6$ (post 2), shown in Fig. 3.14c, the drop does not quite manage to leave the surface and remains stuck. For ridges in the y direction, shown in Fig. 3.14d, the drop jumps only for high intrinsic contact angles

	r_x	w_x	r_y	w_y	$\theta_{Y,j}$	$\theta_{r,j}$
x ridge	–	–	4	20	113°	151°
posts 1	6	10	4	12	114°	143°
posts 2	4	10	6	12	115°	135°
y ridge	4	20	–	–	125°	125°

Table 3.2: Liquid and surface parameters for the coalescence simulations on surfaces of different geometry. We also give the intrinsic contact angle and the local Cassie-Baxter angle (see Eqn. (3.11)) at and above which jumping can be seen, $\theta_{Y,j}$ and $\theta_{r,j}$, respectively.

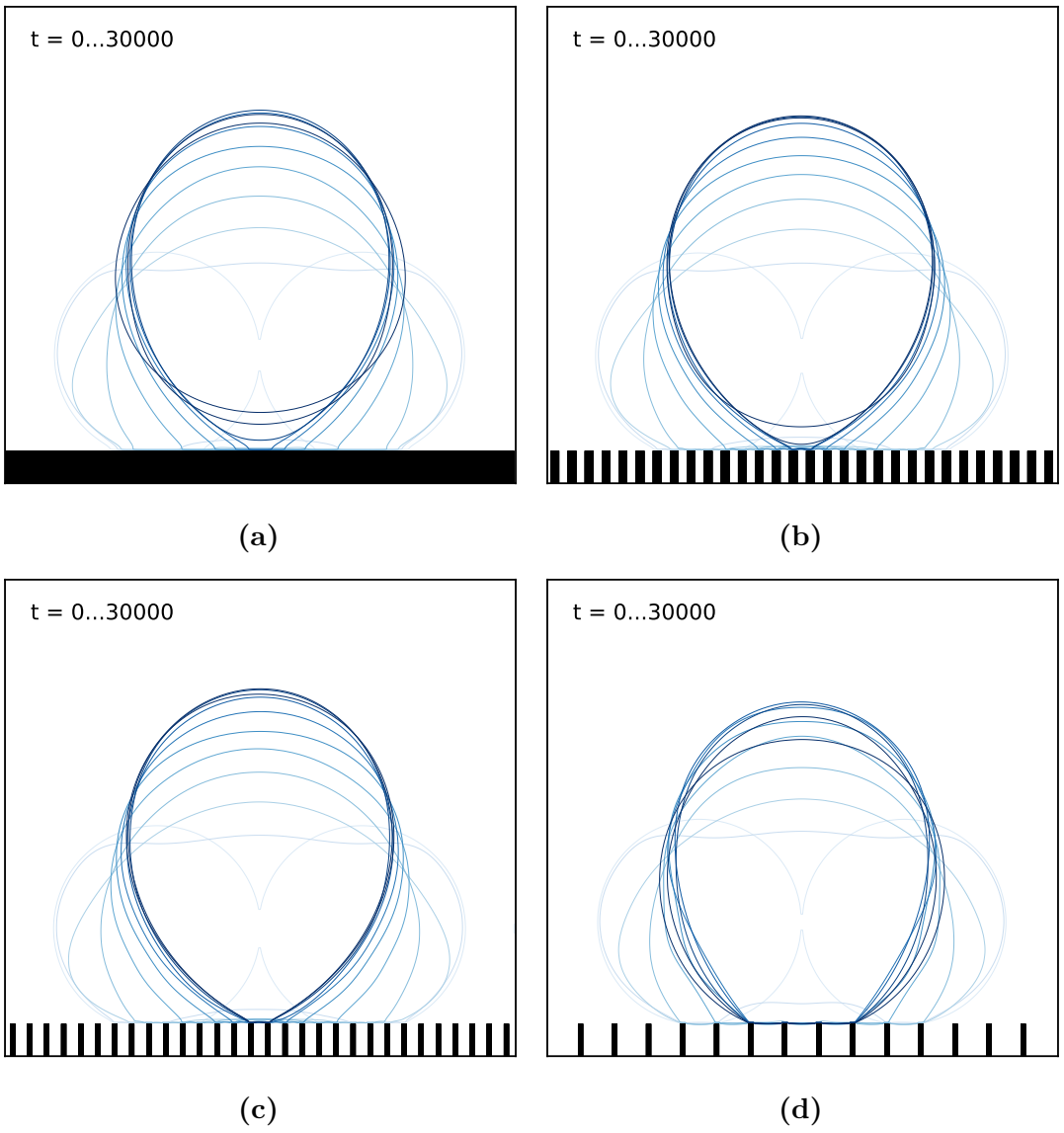


Figure 3.14: Evolution of the drop contour with time for the different geometries specified in Table 3.2 for $\theta_Y = 114°$ in all cases. (a) x ridge, (b) posts 1, (c) posts 2, (d) y ridge. Shown is the y layer cutting across the middle of the surface feature. Time runs from light blue to dark blue.

$\geq 125°$. It lifts only a little, let alone jumps, for the contact angle of $\theta_Y = 114°$ used in the simulation shown in Fig. 3.14d.

3.6.2 Intuitive Explanation of the Effects of Substrate Anisotropy

The anisotropy observed in Fig. 3.14 is a manifestation of pinning (see Ch. 1.2.2). When moving across the substrate, the contact line has to de-pin from every edge that it encounters. A pinning event interrupts the natural motion of the contact line, which

results in the fluid losing momentum that could otherwise contribute to jumping. We will revisit this intuitive picture later and discuss it in detail. First however, we will describe why we expect the effect of pinning to be dependent on the directionality of the solid features.

On the ridge in the x direction, there is no pinning during the recession of the contact line, as there is no edge perpendicular to the contact line's motion. Therefore it is easier for the merged drop to jump on this surface than on the other substrates. The opposite case is ridges along the y direction, which correspond to two-dimensional posts, where the contact line has to de-pin from every post it encounters. The effect of pinning is less pronounced for three dimensional posts than for y ridges, as the curved interface between the posts aids de-pinning. We have considered two different post geometries which differ in the direction of their longest side. The posts that are longer in the x direction are closer to an x ridge and therefore de-pin slightly more easily. This is reflected in the drop's ability to jump at $\theta_Y = 114°$ on this surface, whereas the surface with posts elongated in the y direction does not permit the drop to jump at this contact angle.

The effect of Gibbs' pinning depends on the intrinsic contact angle of the solid edge (see Ch. 1.2.2). Higher contact angles should lead to less pinning and hence less inhibition of coalescence and jumping. We varied the contact angle to find the threshold θ_Y at which the different surfaces would allow the drop to jump. The contact angles that allow jumping are listed in Table 3.2. Their relative magnitudes support the pinning strength arguments outlined in the previous paragraph. In Table 3.2, we also give the corresponding receding angle $\theta_{r,j}$, which is a local version of the Cassie-Baxter angle, the relevance of which we now describe.

The Cassie-Baxter relation for contact angles holds for $r_{x,y}, w_{x,y} \ll R_0$ [117] which clearly is not the case for our simulations. Additionally, it has been shown [118] that during receding the contact line of a drop moves according to a differential area fraction $\phi_{a,d}$ which reflects the local angle of the contact line with respect to the surface geometry. In our quasi-2D case of posts and ridges in the x direction, $\phi_{a,d}$ becomes a one-dimensional line fraction $\phi_{a,d} = r_y/w_y$, and for the two dimensional case of y ridges $\phi_{a,d} = 1$. The

modified Cassie-Baxter relation for the receding angle therefore reads

$$\cos\theta_r = \phi_{a,d}\cos\theta_Y + \phi_{a,d} - 1. \tag{3.11}$$

Therefore, in the two-dimensional case $\theta_r = \theta_Y$. For $\theta_r \geq \theta_{r,j}$ the drop manages to detach from the surface.

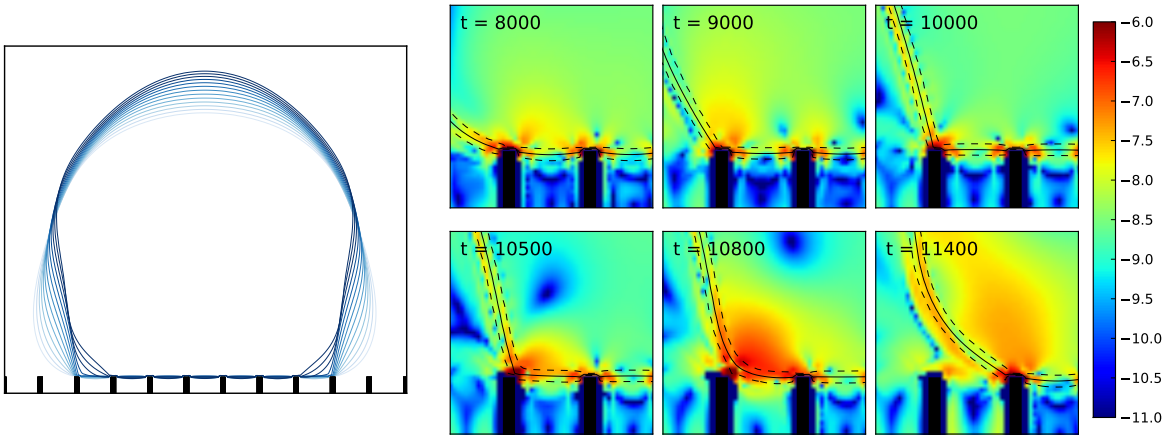
To summarise, as we have kept the area fraction ϕ_a the same for all surfaces, the different jumping behaviour must be due to the directionality of the surface features. We can therefore conclude that the coalescence process is anisotropic with respect to the surface features. Our initial intuitive picture of the coalesced drop simply pushing off the solid surface is therefore not sufficient to describe the coalescence-induced jumping effect. The receding motion of the contact line affects the jumping behaviour. Two drops coalesce and jump more easily if the coalescence motion happens along surface ridges than across them. This anisotropy is a result of Gibbs pinning. Therefore, pinning is very important to the phenomenon of coalescence-induced jumping of small drops. In the following sections we will study the effects of pinning in more detail.

3.6.3 Effect of Pinning on Coalescence-Induced Jumping

Pinning affects the motion of the drop and the jumping ability on posts in two characteristic ways. The first concerns the motion of the contact line while the drop merges and starts lifting, the second affects the final detachment from the surface, as can be seen in Fig. 3.14c and Fig. 3.14d. Both will be discussed briefly in the following.

3.6.3.1 Local Pinning During Receding Motion

During the merging and lifting motion of the liquid the contact line has to move, it recedes across the features of the surface. During this receding motion it encounters the edges of the posts and y ridges, which will lead to pinning. The receding drop has to deform such that the angle θ it forms with the substrate is small enough. Once $\theta < \theta_r$ is achieved, the contact line slides across the post and then detaches from the anterior edge



(a) **(b)**

Figure 3.15: Pinning during the receding motion of the contact line. (a) Change of drop shape with time, showing clear de-pinning according to scenario 3 in [123] for y ridges with $\theta_Y = 105°$. Time runs from light to dark shades. (b) Detailed view of the de-pinning contact line and local dissipation rate associated with the de-pinning event, given on a logarithmic scale, in lattice units. The time is given in lattice untis as well.

[119, 120, 121, 122]. The dissipation associated with a single de-pinning event is only due to the extra deformation of the interface from pinning [123]. With our simulations we can access the de-pinning process and shed light on the details of the dissipation.

In Fig. 3.15a the evolution of the drop shape during a pinning event is shown. It can clearly be seen that the contact line is pinned at the posterior edge, moves forward once the contact angle is $\leq \theta_Y = 105°$, slides across the post and then detaches from the anterior edge of the post. The dissipation rate arising from the de-pinning mechanism is given for selected time steps in Fig. 3.15b. It is obvious that the dissipation in the vicinity of the contact line strongly increases when the drop detaches from the anterior edge of the post, by about two orders of magnitude.

3.6.3.2 Global Pinning at Lift-Off

Besides pinning during the retreat of the contact line, the drop is also subject to pinning as it tries to finally detach from the surface, as we saw in Fig. 3.14c and Fig. 3.14d. The contact line may stay pinned at the edges of the last two posts, or even more posts, as

the drop tries to lift off the surface. As described in the previous subsection, de-pinning and detachment of the drop in only possible if the drop's surfaces is distorted such that it forms an angle $\theta < \theta_r$. Whereas this is easily achieved during the retreat of the laterally elongated drop for sufficiently large θ_Y, the situation is different for the lifting motion of the drop. When lifting, the drop may not be able to form sufficiently small angles θ.

We know from Sec. 3.5.3 that the drop takes the same, almost spherical, shape as it tries to detach, therefore we can deduce that, additionally, it needs kinetic energy that allows the drop to deform such that $\theta < \theta_r$. Besides this kinetic energy needed for de-pinning, there also has to be sufficient kinetic energy to overcome the adhesion energy of the last posts the drop is attached to.

Therefore, the ability of the drop to leave the surface depends on the kinetic energy the drop still has when trying to detach. For a given drop size, the remaining energy depends on the amount of energy dissipated during the lateral retraction of the drop and therefore on the number of pinning events before lifting and the local drop distortion on these occasions.

The amount of energy lost through pinning is difficult to quantify exactly, but will decrease if θ_r increases. This is the reason why both a higher intrinsic contact angle and a surface geometry predominantly parallel to the x direction lead to an increased ability to jump.

3.7 Discussion

In Sec. 3.4 we presented simulation results for the coalescence of two drops in free space and identified the hydrodynamic regime the simulations showed as the capillary-inertial regime. This was done based on the time evolution for the bridge radius. The data for different drop sizes collapsed when making the time non-dimensional using the capillary-inertial time scale. Capillary-inertial scaling was also confirmed by fitting the collapsed data by a straight line in a double-logarithmic plot. However, we fitted the curves over a short interval of one decade only – usually, confirming a power law dependency is

done by considering an interval of several decades of the independent parameter. In our simulations however, we argued that we could not reliably measure the bridge dynamics for small b, owing to the size of the interface width relative to the size of the drop.

We proceeded by presenting simulation results for coalescence on surfaces in Sec. 3.5, which lead to jumping. The sequences shown in Fig. 3.10 for such an event indicate that the assumptions made in [87] do not describe the process correctly. In this publication, the authors stated that coalescence-induced jumping would happen in two stages: a coalescence process in which the two initial drops move towards each other and form a spherical cap, and the retreat of the contact line leading to drop lifting.

Our simulations suggest a different scenario. Fig. 3.10 shows that the initial drops stay in their position while a liquid bridge forms between them. This elongated shape then retracts while the bottom of the liquid bridge pushes the drop away from the surface due to the inertia of the retraction. This indicates that the inertia of the coalescence process is underestimated in [87] and would have to be entered into the dynamic equations the authors solve to characterise self-propelled jumping.

In Sec. 3.5.1 we presented a simple argument explaining how a present surface leads to jumping. This argument explains that the jumping velocity should scale with ν_{ci}, which is confirmed by the experimental findings in [77] and the theoretical prediction in [84]. However, our argument simplifies the physical situation significantly, it ignores deformation of the drop due to the surface. Moreover, it implies that the drop, after detachment, may elongate further vertically. There are no reports of this in the experimental studies referenced, and neither do our simulations show extra elongation after detachment. However, this might be due to viscous losses in our simulations on surfaces which prevent drop oscillations with large amplitudes.

For drop coalescence of different surfaces, we were able to identify that Gibbs' pinning causes an anisotropy of the jumping ability. We were however not able to quantify the effect, due to two reasons. We considered relatively small drops, on few posts, which means that surface interaction has a discrete nature. This makes it difficult to derive and test a theory. The small size of the drops also lead to overlap of the initial drops when

placed on the posts, as placement becomes difficult to control. This affects the energy available for jumping and therefore the jumping ability.

It would have been helpful to quantify dissipative effects in our simulations. However, spurious dissipation was strong, due to high contact angles because we used $\tau_\rho \neq 1$ to allow low viscosities. A method to circumvent this is to calculate dissipation from the energy balance of the system, as we did in Sec. 3.5.2. However, the energy balance method has to take into account the kinetic energy of the gas, which is not negligible due to the unit density of the gas.

3.8 Summary and Outlook

In this chapter we investigated different aspects of drop coalescence, we considered the coalescence of free drops in two dimensions and the coalescence on surfaces, in a quasi-2D geometry. For the coalescence of free drops we gave an argument based on dimensionless numbers to indicate that in our simulations we observe the capillary-inertial regime. We confirmed this by showing collapse of the data for different drop sizes when the time was non-dimensionalised by the capillary inertial time scale, and we found that the growth of the bridge radius follows the theoretical and experimental results in the literature.

When placed on a surface, coalescing drops are subject to a breaking of up-down symmetry and to the boundary conditions imposed by the surface. We explained the effect of the symmetry breaking by considering a perfectly de-wetting surface, which leads to the drop detaching in a shape that is nearly spherical and leaving the surface with a velocity scaling with ν_{ci}. In our simulations, the drops do not detach with a velocity $\sim \nu_{ci}$ which we explain by the presence of dissipation.

The energy that would be available for jumping scales with the difference between the surfaces of the two initial drops and the composite drop. We find that for free coalescence about 30% of the available energy remains, whereas for coalescence on a ridge surface only about 8% is left for jumping. The fact that only such a small fraction of the available energy remains to be used for jumping is owed to strong dissipation during the bridge

forming process, and, additionally, dissipation due to the retraction motion along the surface.

We proceeded by comparing the effect of different surface geometries on coalescence-induced jumping. We found an anisotropy: the drops jump more easily if the coalescence happens along a ridge rather than perpendicular to it. The reason for this anisotropy is Gibbs' pinning which affects both the receding motion of the contact line while the drop retracts and the lifting process. We confirmed that Gibbs' pinning during retraction is associated with the dissipation of energy. The energy dissipated during these pinning events subsequently affects the ability of the drop to jump as it cannot deform sufficiently to overcome pinning when trying to detach from the surface.

For the coalescence process on a surface the parameter regime used in our simulations did not allow us to observe jumping in the capillary-inertial regime, due to dissipation in the system, both during the coalescence process and during the drop retraction stage. However, dissipation during the retraction of the drop can be avoided if surface interaction is circumvented by setting $\theta_Y = 180°$. It would be interesting to see if, by this measure, and by using larger drop sizes to achieve $Oh \ll 1$, the experimental results for the behaviour of v_{jump} with increasing drop size can be reproduced. Additionally, with such simulations our predictions on the drop shape during and after detachment, as discussed in Sec. 3.7, could be tested.

Understanding the influence of different surfaces on drop detachment is important as it may help design surfaces better suited for water harvesting or cooling applications. In such applications, drop removal at small drop sizes is crucial for the efficiency of the device. Therefore it will be beneficial to understand the influence of surfaces on coalescence-induced jumping even when dissipation is not negligible. So far, we could only describe the effect of surfaces qualitatively but it was beyond the scope of this thesis to develop a theoretical model. Simulations with larger drop sizes, which could be two-dimensional, would help overcome the problems discussed in Sec. 3.7. Moreover, being able to exactly calculate the dissipation arising from pinning would be helpful. With the lattice Boltzmann formalism used in this thesis this was not possible, due to

spurious effects and gas inertia, as described in Sec. 3.7. However, in our group currently a lattice Boltzmann method based on [124] is being implemented, which allows large density and viscosity ratios of up to 1/1000. Such a simulation method would allow to quantify dissipation if an energy balance method is applicable.

Chapter 4

Pancake Bouncing

4.1 Motivation

In the introduction to this thesis (Sec. 1.4) we have described what phenomena emerge upon drop impact on conventional flat surfaces, and how micro/nano-patterned, superhydrophobic, surfaces enrich the physics of impacts as they allow complete rebound of water drops. The usual pathway for impact upon superhydrophobic surfaces is the following: As a drop lands it spreads under the driving of inertia into a disc-like shape and then retracts its elongated surface to minimise the surface energy, remaining in contact with the surface throughout the receding stage. The drop eventually rebounds off the surface in an approximately spherical shape – the rebound is close to elastic because of the low friction on a superhydrophobic substrate.

Recently however, a very different behaviour has been reported. On a special multi-layered, two-tiered, and superhydrophobic substrate (MTS), a drop was seen to take off without retracting first – it left the substrate in the elongated shape. An example of this remarkable behaviour can be seen in Fig. 4.1. This phenomenon was termed 'pancake bouncing' [125]. As far as we are aware this bouncing pathway has not been reported previously and it represents a significant departure from conventional liquid impact regimes on a solid surface.

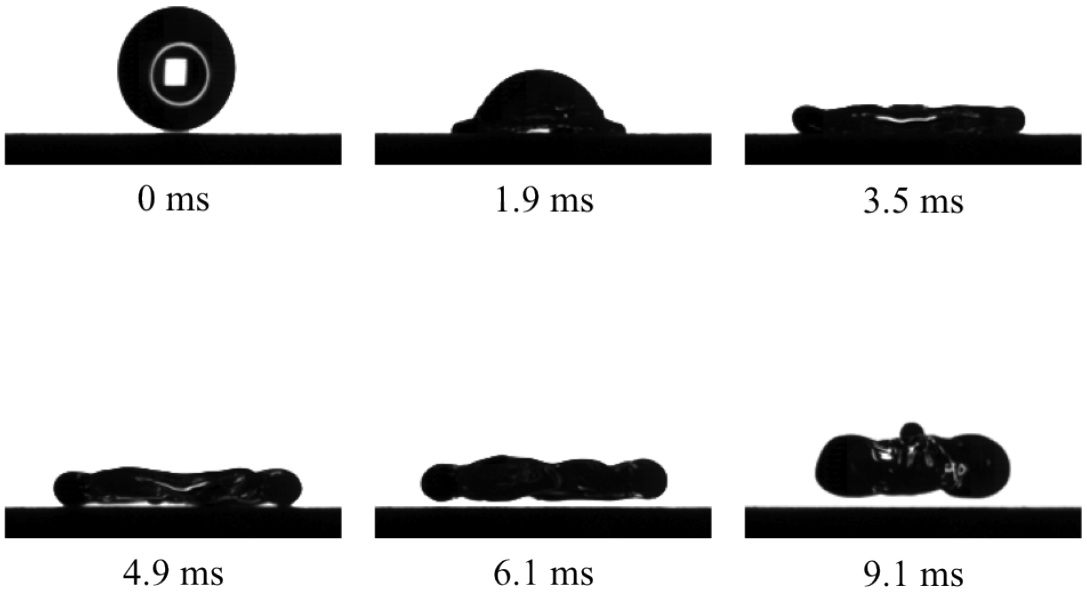
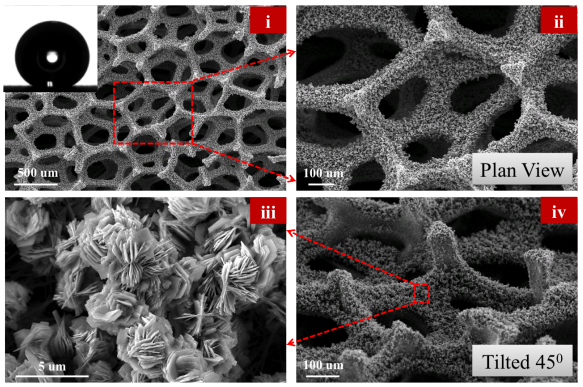


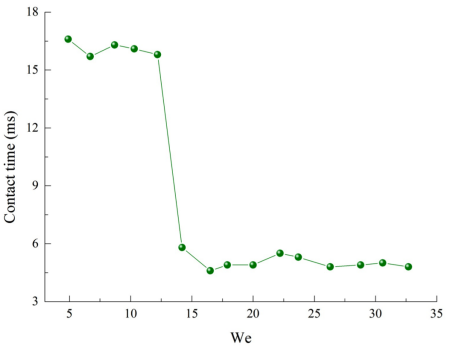
Figure 4.1: Time sequence of a bouncing process on MTS substrate showing pancake bouncing at $We = 19.6$. Courtesy of Zuankai Wang, Department of Mechanical and Biomedical Engineering, City University of Hong Kong

4.1.1 Initial Experiments

The experiments first showing pancake bouncing were performed by the group of Zuankai Wang, Department of Mechanical and Biomedical Engineering, City University of Hong Kong. The novel texture on which they first observed pancake bouncing is a solid copper substrate that is multi-layered, two-tiered, and superhydrophobic. As shown in the scanning electron microscopy (SEM) image in Fig. 4.2a, the material is alveolar, with stacks of hexagonal pores topped by a hexagonal array of micropillars. The average pore diameter in the porous medium is 400 µm, and the pillars' height, diameter, and mutual spacing are 200 µm, 40 µm, and 260 µm, respectively. In addition, all the solid surfaces of the material are coated by nanostructured flowers of average diameter 3 µm which are made superhydrophobic. The intrinsic contact angle of a flat surface covered with the nanoflowers is 160°. The apparent contact angle of water on the MTS surface is over 160°, and the contact angle hysteresis is less than 2°.



(a)



(b)

Figure 4.2: (a) Micrograph of the MTS substrate. (i) top view, showing the porous nature of the texture, (ii) increased magnification, showing the triangular pillars at the top of the porous structure, (iii) close-up of the nanoflowers covering the entire structure, (iv) side view of the micropillars covering the top of the substrate.
(b) Sudden decrease of contact time with increased Weber number for drops bouncing on the MTS surface.
Both figures courtesy of Zuankai Wang, Department of Mechanical and Biomedical Engineering, City University of Hong Kong.

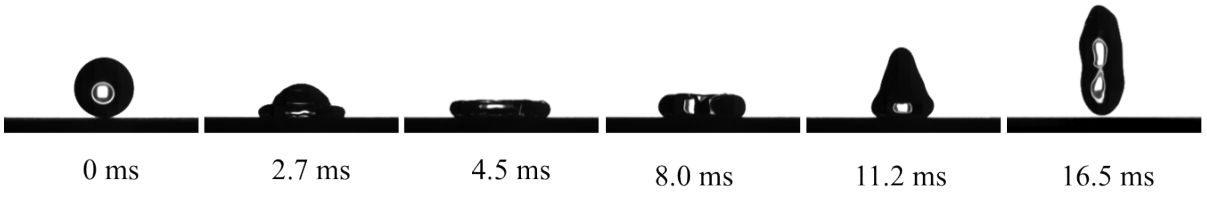


Figure 4.3: Time sequence of a bouncing process on an MTS substrate showing a conventional rebound at $We = 7.8$. Figure courtesy of Zuankai Wang, Department of Mechanical and Biomedical Engineering, City University of Hong Kong.

The researchers first conducted water droplet impact experiments on the MTS surface using a high speed camera at the rate of 10,000 frames per second to follow the drop motion. The unperturbed radius of the drop was $R_0 \approx 1.45$ mm, and drop velocities on impact v_0 ranged from 0.49 to 1.32 m/s, corresponding to $4.9 < We < 34$. At the lower Weber numbers the drop maintained contact with the substrate and retracted fully before leaving the surface, in the conventional way documented in the literature. An example sequence at $We = 7.8$ is shown in Fig. 4.3. Above $We = 14$ however, pancake bouncing set in, as shown in Fig. 4.1. Here the drop rebounds from the surface very close to its maximum extension, in a pancake shape, without undergoing significant lateral retraction.

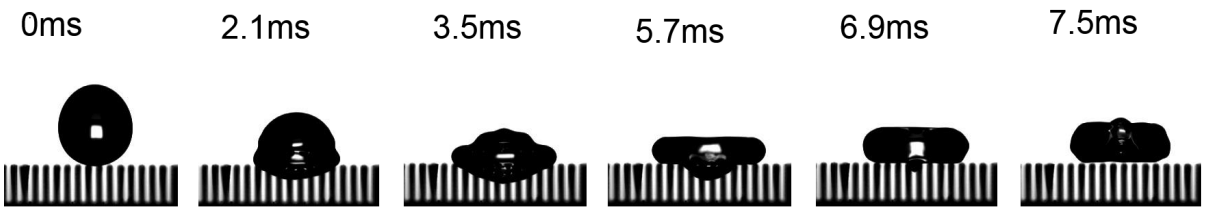


Figure 4.4: Impact on superhydrophobic posts showing pancake bouncing. $We = 4.7$, $w = 0.4\,\text{mm}$, $a = 0.1\,\text{mm}$, $h_p = 1.4\,\text{mm}$. Photos courtesy of Zuankai Wang, Department of Mechanical and Biomedical Engineering, City University of Hong Kong.

The water directly detaches from the substrate at the end of the spreading stage.

The switch from 'conventional' to 'pancake' bouncing also affects the time the drop spends in touch with the surface. Namely, the contact time with the surface is greatly reduced, by a factor ≈ 3 compared to conventional bouncing after retraction, as shown in the plot in Fig. 4.2b. Such pancake bouncing persists up to $We \approx 33$; at higher impact velocities parts of the impinging drop are trapped within the surface and the effect breaks down.

4.1.2 Simplified Surfaces

The Hong Kong material scientists approached us at Oxford for support in understanding the pancake bouncing process theoretically. Their initial experiments suggested that there might be liquid penetration into the substrate, which might be relevant to the bouncing process, but details of the mechanisms leading to pancake bouncing were not accessible from their experimental data.

To get an idea of the physics involved in the pancake bouncing process we performed lattice Boltzmann simulations which will be described in detail in Sec. 4.3. In these simulations, we simplified the surface structure considerably. Instead of mimicking the complicated alveolar substrate, we used a surface comprised of simple posts to study the drop impact. In certain parameter regimes the pancake effect could indeed be seen, and the simulations revealed that there is considerable liquid penetration into the substrate, and that the imbibition motion affects the overall bouncing characteristics.

Based on these observations, we suggested to the experimentalists that they perform

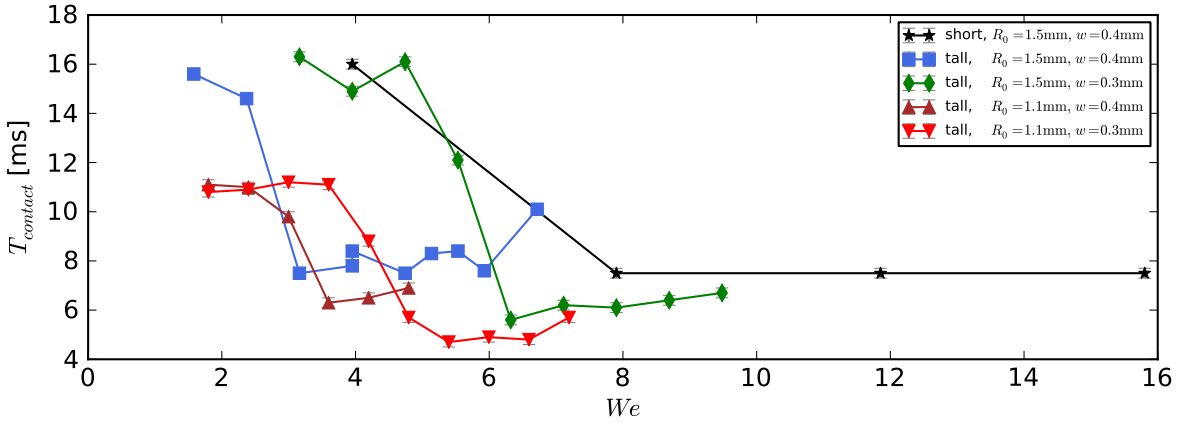


Figure 4.5: Contact time as a function of We for different post substrates and drop sizes $R_0 = 1.45$ and 1.1 mm.

experiments on a pillar surface instead of the MTS. This is because the liquid penetration can be imaged directly for the pillar surface. As the example in Fig. 4.4 shows, pancake bouncing could indeed also be observed in experiments on simple post surfaces, and is not exclusive to the MTS substrate.

For the post experiments drops of two different sizes of $R_0 = 1.10$ mm and 1.45 mm were used with impact velocities ranging from $v_0 = 0.28$ to 0.69 m/s, corresponding to $We = 1.2 \ldots 9.5$. The surfaces were single-layered copper substrates patterned with posts which were covered with the same nanoflower coating as the MTS. They had centre-to-centre post spacings of $w = 300\,\mu$m and 400 µm and heights of $h_p = 600\,\mu$m and 1.4 mm which allowed for the visualisation of the liquid motion within the structure. I was given access to high-speed videos of these experiments, taken at 10,000 frames per second. The analyses in the next chapter are based on data that I extracted from these videos.

4.1.3 Experimental Observations

For the different post surfaces used for drop impact the experimental data showed several interesting features which can be seen in a plot of the contact time against the impact Weber number, shown in Fig. 4.5. In our discussion, we will call posts of height $h_p = 0.6$ mm 'short posts' and posts with $h_p = 1.4$ mm 'tall posts'. The distinction is

based on whether the liquid touches the base of the substrate in the process of imbibition. The key observations were:

1. As with the MTS substrate, there is a distinct decrease in the contact time for impact velocities above a certain Weber number We^*. This We^* corresponds to the onset of pancake bouncing.
2. We^* depends strongly on the substrate and on the drop radius, as is apparent from the sideways shift of the different curves in Fig. 4.5. However, there is a lowest $We^* \approx 3$ which the curves with blue squares and brown upward triangles have in common, which correspond to w =0.4 mm, but different drop sizes. Moreover, the thresholds for pancake bouncing seen in Fig. 4.5 for post surfaces are considerably smaller than for the MTS. For posts, we observe $We^* \approx 3 \ldots 6$, but for the MTS substrate $We^* \approx 14$ (see Fig. 4.2b).
3. The contact time for conventional bouncing, that is for $We < We^*$, depends only on the initial drop radius. For $R_0 = 1.45$ mm which corresponds to the black stars, blue squares, and green diamonds, the contact time for conventional bouncing is ≈16 ms. This is the same as on the MTS substrate for impacts of the same drop size. For the smaller radius of $R_0 = 1.1$ mm, corresponding to brown upward triangles and red downward triangles, the contact time for conventional bouncing is lower, ≈ 11 ms.
4. The contact time for pancake bouncing at $We > We^*$ depends not only on the drop size, but also on the spacing of the substrate's posts.
5. After the sharp decrease of the contact time, it gradually increases again with increasing We. How pronounced this increase is with $We > We^*$, however, depends on the substrate. In particular, for short posts, corresponding to black star symbols, the low contact time seems to persist over a large range of Weber numbers. This is also the case for the MTS substrate, see Fig. 4.2b. On the MTS, low contact times corresponding to pancake bouncing are observed in a range of $14 < We < 33$.

These observations indicate that the pancake phenomenon can be observed on a variety of surfaces, and that it depends on the interplay between the micro- and nano-textured

structure and the impact conditions.

4.1.4 Summary of Experiments and Outline of the Chapter

To conclude our summary of the experimental observations, pancake bouncing is a new impact pathway that represents a significant departure from the liquid impact regimes described in the literature to date. It occurs on several different superhydrophobic surfaces, and therefore we consider pancake bouncing a robust phenomenon which may be relevant to many different surfaces and a large number of applications. The discovery of this new impact pathway opens up a wealth of new physics. Because of the short impact time, it may find promising applications in areas where the time spent on a surface is important, such as self cleaning, heat transfer and anti-fouling and anti-icing technologies.

In this chapter we will explain the phenomenon of pancake bouncing theoretically, based on lattice Boltzmann simulations and supported by the experiments performed by our collaborators which were described in Sec. 4.1.2. In order to do this, it is first necessary to review the state of the art in the physics of drop impact processes. Therefore, in Sec. 4.2 we will present certain aspects of drop impacts that are relevant to the problem at hand. In Sec. 4.3 we will describe the lattice Boltzmann simulations performed to explore the phenomenon of pancake bouncing. Based on the results of these simulations, we will describe in Sec. 4.4 the general mechanisms of the process and identify two criteria necessary for pancake bouncing. Theoretical discussion of the pancake effect is done in Ch. 5. Sec. 5.1 is dedicated to the derivation of a theoretical model describing the two criteria. The results of applying our theoretical model to both the simulations and the experimental data are presented in Sec. 5.2. Based on the theoretical model, we summarize our results in Sec. 5.2.1 in the form of a phase diagram which reveals the surface and drop parameters leading to pancake bouncing. This design diagram also serves as an explanation for the experimental observations described in Sec. 4.1.3. Then, in Sec. 5.3, we will discuss the applicability of the assumptions used to derive the model presented in Sec. 5.1. Sec. 5.4 summarises and concludes our research on the pancake

effect.

4.2 Relevant Aspects of Bouncing

In this section we will review the relevant literature on the physics of impact processes, in particular introducing concepts which are directly related to understanding and modeling the phenomenon of pancake bouncing. The literature on bouncing droplets is usefully divided into papers with three main objectives: (i) explaining the time the bouncing event takes, the contact time or bouncing time, $T_{contact}$, (ii) finding models to describe the maximum extension of the drop during the spreading process, the spreading diameter D_{max}, and (iii) conditions for bouncing, which could be conditions related to the deformation of the drop or conditions related to the substrate geometry. In the following sections we briefly summarize the state of the art for these main areas of interest.

4.2.1 Contact Time

Richard et al. [80] measured the contact time of a bouncing water drop, finding that viscosity is not important and, for moderate deformation, that is for Weber numbers higher than $We \approx 1$, the bouncing time is independent of the impinging velocity v_0, but scales as $T_{contact} \sim (\rho R_0^3/\sigma)^{1/2} = \tau_{ci}$. The scaling can be readily explained if one considers the bouncing process as an oscillation – the drop behaves like an ideal spring with mass $\sim \rho R_0^3$ and spring constant σ, giving a period of $\sim (\rho R_0^3/\sigma)^{1/2}$. This result had already been found in 1879 by Rayleigh [126], who analytically calculated the frequency of drop oscillations for arbitrary but small distortions of a free drop. Taking into account higher orders of spherical harmonics, but with deformations $\ll R_0$ so as to allow linearisation, he found a general expression for the period of oscillation

$$T_{osc} = \frac{2\pi}{\sqrt{\ell(\ell-1)(\ell+2)}}\sqrt{\frac{\rho R_0^3}{\sigma}}. \tag{4.1}$$

For the simple quadrupolar mode which corresponds to a flattening and elongation deformation with $\ell = 2$, and which is certainly the dominating one for a bouncing drop, the oscillation period is

$$T_{osc} = \frac{\pi}{\sqrt{2}}\sqrt{\frac{\rho R_0^3}{\sigma}} \approx 2.2\sqrt{\frac{\rho R_0^3}{\sigma}} = 2.2\tau_{ci} \tag{4.2}$$

for a free drop in vacuum.

Several other authors have confirmed this scaling [53, 55, 56, 127, 128], albeit finding different prefactors. Experimentally, prefactors of 2.6, 2.65, and 2.3 were found in [80], [53], and [55], respectively. Vincent measured 3.0 [127], but this slightly different prefactor is expected, because he considered bouncing bubbles instead of drops. Taking into account that the skin of a bubble has a double liquid-air interface gives an effective surface tension of 2σ which would decrease the oscillation period by a factor of $1/\sqrt{2}$. The density of the surrounding being equal to that of the bubble itself increases the oscillation period, according to [129], p. 475 , by a factor of $(5/3)^{1/2}$ [127]. With these two effects, the equivalent prefactor of a drop in air would be $3.0(5/3)^{-1/2}2^{1/2} = 3.3$.

The authors of [53, 55, 80, 127] compare their results with Rayleigh's value of 2.2 for the free oscillating drop. As they explain, differences may be due to distortions that are much larger than in the linear regime [53]. Another possible explanation, found analytically by Courty et al. [56], is that an oscillating driving force exerted on a free drop acts to increase the oscillation period by $1/0.78 = 1.28$. This is cited in [53] and [127] as a possible reason for the deviation of the measured values of 2.65 and 3.3, respectively, from Rayleigh's 2.2. However, as Courty et al. say themselves, in the case of a bouncing droplet the wall does not represent an (oscillating) driving force but induces an oscillation by transfering the kinetic energy of the incoming drop into sideways motion resulting in an oscillation. Based on this consideration, they calculate a prefactor of 2.3, which is indeed close to the measured bouncing time prefactors.

I believe that comparing the value of 2.2 for the scaling prefactor to the experimentally found values for the bouncing times does not make much sense in the first place. 2.2 is

the value found for the oscillation period of a free drop. Besides deviations caused by having a surface and because the deformation amplitudes are not in the small, linear regime, we have to keep in mind that the period time of the free oscillation describes one full oscillation. One full oscillation should cover the shape changes from spherical to flattened, to elongated, back to spherical, whereas the bouncing time should, in first approximation, be closer to *half* an oscillation, an assumption also taken in [56]: It covers the motion from spherical just before hitting the surface, to flattened, to spherical when detaching [26], as could be seen in Fig. 1.7. For high-velocity impacts with $We \gg 1$ the drop tends to be elongated vertically when detaching [26], indicating that the bouncing time should be between a half and a full period, depending on the impact Weber number.

This idea of detaching happening at different stages of the spring-like oscillation is discussed in detail in [55]. The authors find, using scaling arguments and analytically, that for small deformations the contact time is equal to the oscillation period. 'Small deformations' here means that the deformation from the impact is smaller than that due to gravity; gravity has been neglected in the articles reviewed here so far. With increasing velocities, but still smaller than ν_{ci}, i.e. $We \ll 1$, the contact time decreases to reach a plateau at *half* the oscillation period. The authors confirm this behaviour experimentally. It shall be emphasised though that this *half* oscillation period is still about $2.0\,(\rho R_0^3/\sigma)^{1/2}$, so the full oscillation period on a surface is close to *twice* the oscillation period of a free drop with small deformations – as discussed in the previous paragraph. This behaviour for $We \ll 1$ is also in agreement with the findings of Richard et al. [80], where the authors reported that they only saw a bouncing time independent of the impact velocity for $We > 1$. For $We \ll 1$ they observed a gradual increase of the bouncing time to about twice the value measured in the constant regime. In [128] Okumura et al.'s calculations [55] are extended, using a logarithmic correction, and the same qualitative result is found.

4.2.2 Maximum Spreading

For our purposes in this Chapter it is important to know how wide a drop spreads during the process of bouncing. For Weber numbers smaller than unity, a bouncing drop will be deformed little, its maximum deformation will be an ellipsoidal shape [50]. In the regime of higher impact velocities, for $1 \lessapprox We \lessapprox 10$, the drop will form a 'puddle', a disc-like shape of maximum width D_{max} and height H_{min}, whereas in the limit of $We \gg 1$ it will be distorted more to form a lamella bounded by a rim (see Ch. 1.4.2). The maximum spreading will be a result of the interplay of inertial forces, surface tension forces, and possibly viscous forces. It scales as $D_{max} \sim D_0 We^{1/4}$, where $D_0 = 2R_0$ [50, 53, 130].

In trying to explain this scaling we follow the very educational deliberations of Clanet and co-workers [50]. An obvious first approach is to use energy conservation: we assume that the kinetic energy of the incoming drop is simply turned into surface energy. When all kinetic energy is consumed, the drop edge comes to rest, and then the retraction process starts. We can approximate this balance as $\rho D_0^3 v_0^2 \sim \sigma D_{max}^2$, yielding $D_{max} \sim D_0 We^{1/2}$, which contradicts the observed $We^{1/4}$ scaling. Apparently, energy conservation is not the correct approach. If energy dissipation is taken into account, with the dissipated energy scaling as $\eta v_0 D_0 D_{max}^2 / H_{min}$ [41], a square-root dependence on We is still found in the limit of large Reynolds numbers, again clearly in contradiction to the physical observation.

However, treating the flattened drop as an effective gravity puddle leads to the correct scaling. A drop larger than the capillary length sitting on a surface is flattened such that gravity and surface tension forces are balanced, forming a puddle rather than a spherical cap. Now, the acceleration experienced by a drop as it hits a wall acts as an effective gravity, scaling as $\frac{v_0 - 0}{\tau_{crash}}$, where the denominator is the crashing time τ_{crash}, of order D_0/v_0. This acceleration $\sim v_0^2/D_0$ exceeds g by two orders of magnitude in a typical experiment, explaining why the drop is so markedly puddle-shaped. The height of this puddle should

scale with a corresponding effective capillary length h_{cap},

$$H_{min} \sim h_{cap} = \sqrt{\frac{\sigma D_0}{\rho v_0^2}}. \tag{4.3}$$

Then volume conservation $H_{min} D_{max}^2 \sim D_0^3$ yields

$$D_{max} \sim D_0 We^{1/4}, \tag{4.4}$$

the scaling observed in experiments [50]. The authors confirm the idea of an effective gravity by experiments in which they rapidly accelerate a drop sitting on a surface upwards, confirming again that $D_{max} \sim We^{1/4}$.

As this maximum width is smaller than that expected if energy conservation holds, the question arises where the missing energy has gone, when in the inviscid limit. It turns out that the assumption that the liquid comes to rest at maximum spreading is false – there is in fact a vortex of internal flow around the edge of the arrested drop which was observed in [50] through tracer particles in impact experiments with balloons at the same conditions as their drop experiments. A sketch of the observed flow is reproduced in Fig. 4.6.

While Clanet and co-workers employ very simple scaling arguments to explain the $We^{1/4}$ behaviour, Merlen et al. arrive at a similar scaling analytically, considering the distribution of Laplace pressure within the drop [130]. They find $D_{max} = D_0(\frac{4\alpha}{3} We + 1)^{1/4}$ in good agreement with Clanet's, Biance's and their own experimental observations [50, 53, 130].

4.2.3 Bouncing Conditions

It was already indicated in Ch. 1.4.3 that low dissipation is a necessary requirement for drop rebound to occur. This requires a high apparent contact angle and a low contact angle hysteresis. Therefore superhydrophobic surfaces (and Leidenfrost surfaces [53]) are suited to observe droplet bouncing. The low contact angle hysteresis results in a low threshold

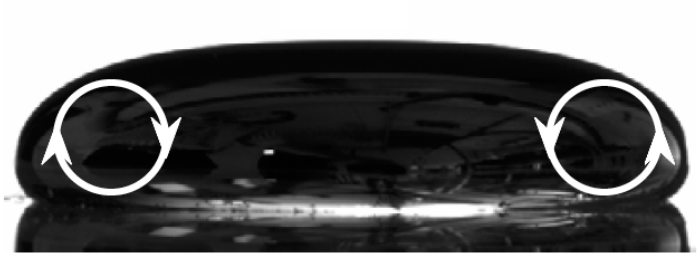


Figure 4.6: Sketch of the vortical motion revealed by the presence of tracers inside a balloon, figure taken from [50]. The balloon was dropped onto a surface at the same impact conditions as for the drop experiments studied in [50]. Reproduced with permission.

for the kinetic energy E_K of the impinging drop to see bouncing, $E_K > \sigma R_0^2 \Delta \cos\theta$ [59, 131], where $\Delta \cos\theta = \cos\theta_r - \cos\theta_a$ is the contact angle hysteresis, the difference between the receding and advancing contact angles $\cos\theta_r$ and $\cos\theta_a$, respectively. This yields $v_0 > \nu_{ci}\sqrt{\Delta \cos\theta}$ or, equivalently,

$$We > \Delta \cos\theta. \tag{4.5}$$

For a typical superhydrophobic surface this corresponds to a threshold of the order of $We \approx 0.01 \ldots 0.1$, which is not a strong restriction on We.

Yet, a low contact angle hysteresis is just one amongst many of the conditions required for bouncing. Another is that obviously the drop should not be too large. Its size needs to be much smaller than the capillary length so as not to be affected by gravity. This is explained in the framework of the drop-spring model by Biance et al. [53]. If $R_0 \gg \ell_{cap}$ does not hold, the drop's speed has to be large enough so that the elastic force from compression of the drop overcomes its weight, yielding $v_0 > v_{crit} = \nu_{ci}/(1 - R_0^2/\ell_{cap}^2)$ [53] or, equivalently,

$$We > \left(1 - \frac{R_0^2}{\ell_{cap}^2}\right)^{-2}. \tag{4.6}$$

Moreover, there are conditions that depend on the substrate geometry which determine whether a droplet can bounce off for a certain impact velocity. Later in this chapter, in Sec. 5.1.1, we will use arguments that are similar to the derivation of these conditions, so it is helpful to review the substrate related conditions for full rebound here.

4.2.3.1 Substrate Related Conditions

When a drop impacts on a superhydrophobic surface there are certain conditions that ensure that the drop does not stick to the surface. If these are not fulfilled and a drop impinges too fast a transition from the (suspended) Cassie-Baxter state to the (collapsed) Wenzel state is observed, and the drop ends up sticking – partially or fully – to the surface [59, 132, 133]. The conditions can be determined by comparing the dynamic pressure (also referred to as Bernoulli pressure) of impact $p_D \sim \rho v_0^2$ to the pressures acting against the liquid entering the substrate. These are (i) the Laplace pressure p_L of the liquid-gas interface curving between the tops of the posts underneath the drop and (ii) the capillary pressure p_c.

The Laplace pressure p_L counteracts the curving of the interface which is suspended on the edges of the posts. It scales as

$$p_L \sim \sigma\delta/w^2 \tag{4.7}$$

[59], where w denotes the centre-to-centre spacing of two posts and δ is the height of the arc that the curved interface forms. If this arc touches the bottom of the substrate, i.e. if $\delta = h_p$ with h_p being the height of the posts, then the suspended interface will collapse and a transition from the Cassie to the Wenzel state will take place. This collapse mechanism is referred to as the 'sag' or 'touch down' mechanism [59, 131, 133, 134, 135, 136]. Touch-down of the interface will occur if p_D is larger than the p_L associated with $\delta = h_p$, yielding a condition on the dynamic pressure of $p_D > p_{sag} \sim \sigma h_p/w^2$ to effect collapse. Expressing this in terms of dimensionless variables gives

$$We < We_{sag} \sim \frac{R_0 h_p}{w^2} \tag{4.8}$$

for the drop to stay suspended upon impact. The scaling relation for p_L only holds in the limit $r \ll w$, where r is the post width. For post widths that are comparable to their spacing the authors of [59] note that the scaling argument results in $p_D > p_{sag} \sim \sigma h r/w^3$

for collapse, yielding $We < We_{sag} \sim R_0 h_p r/w^3$ as a condition for bouncing.

The capillary pressure p_c impedes the wetting of the sides of the posts. If it is overcome by the dynamic pressure, the liquid interface slides down the sides of the post. This triggers a Cassie to Wenzel collapse transition, leaving an impinging drop sticking to the surface. This collapse mechanism is referred to as the'sliding' mechanism or 'de-pinning' mechanism [59, 133, 136, 137]. The capillary pressure is the force exerted by the perimeter of a post per unit area A_p of projected liquid-gas interface [137]

$$p_c \sim r\sigma \cos\theta_a / A_p, \tag{4.9}$$

where θ_a is intrinsic advancing contact angle of the surface of a pillar. For a generic pillar surface the de-pinning condition can then be expressed as $p_D > p_{slide} \sim \phi_a/(1-\phi_a)|\cos\theta_a|\sigma/r$ [59], where ϕ_a is the area fraction (see Ch. 1.2.1). Or, equivalently,

$$We < We_{slide} \sim \frac{\phi_a}{1-\phi_a}|\cos\theta_a|\frac{R_0}{r} \tag{4.10}$$

to allow bouncing.

4.2.3.2 Water-Hammer Pressure

For the sake of completeness it must be mentioned here that recently another type of pressure has been proposed as relevant to the impalement transition during bouncing [133, 138], the water-hammer pressure p_{WH}.

The phenomenon of water-hammer is well known in engineering applications: $p_{\mathrm{WH}} = \rho v C$, where C is the speed of sound in water and v is the velocity of the flow, occurs in water flow through pipes, where it can cause considerable damage and pipe erosion. It arises due to rapid deceleration of flow when valves are closed [139]. Water-hammer pressure was introduced to drop impact phenomena on flat solid surfaces in [140] as the pressure due to a compressional wave initiated when the drop collides with the solid wall. It is given by $p_{\mathrm{WH}} = \alpha/2\rho v_0 C$, where $\alpha/2$ is a prefactor that is due to the spherical shape

of the drop, with α expected to be close to unity for high-velocity impacts [140]. Indeed, for high-velocity impacts this collision pressure is so significant that it can cause erosion [141].

In [137] the water-hammer pressure is used to explain the Cassie to Wenzel transition of a gently placed drop that neither p_L nor p_D can account for and in [133, 138] it is considered a second wetting pressure, acting in addition to p_D, to facilitate collapse. According to [138], on superhydrophobic surfaces water-hammer pressure is generated at the contact stage of drop impingement, before any spreading sets in and is due to the compression of liquid behind the shock wave envelope. In [133, 137], an expression for the pressure is given as $p_{\mathrm{WH}} = k\rho v_0 C$, where k is a "constant depending on the type of collision" [137]. $C \approx 1.5 \times 10^3\,\mathrm{ms}^{-1}$ is very large, giving a pressure three orders of magnitude larger than p_L and p_D (typically on the order of $0.1 \ldots 10\,\mathrm{kPa}$), without the factor k which the authors introduce and conveniently choose at 0.001 and 0.003, respectively [133, 137]. The authors explain that the high water-hammer pressure rapidly falls to p_D as spreading sets in [138] and is limited to the small area of initial liquid-solid contact [133]. This is assumed to facilitate a partially wetted state if $p_{\mathrm{WH}} > p_c > p_D$, in which only a small area underneath the centre of the drop is wetted [138]. However the authors do not actually observe this state, attributing this to the fact that p_{WH} can not be calculated exactly. Hee et al. [133] find that even when they calculate $p_{\mathrm{WH}} > p_c$ their drops still show full rebound.

In [137] Kwon et al. argue that the unexpected Cassie-to-Wenzel transition following gentle drop deposition is due to p_{WH}. However, I believe this transition could possibly be accounted for by capillary waves travelling down the drop as it detaches from the syringe instead of by introducing p_{WH} (see video available online as part of the supplemental material to [137]). Concerning the papers studying drop impact transitions, [133, 138], I find that the relevance of p_{WH} was after all not conclusively shown. Moreover, the relevance of p_L as an alternative to introducing p_{WH} was not discussed.

Summarising these thoughts, I do not consider the water-hammer pressure relevant to the problem of complete rebound discussed in this chapter. The water-hammer pressure

should be only transient and very localised so I believe that it does not contribute to overall Cassie-to-Wenzel collapse which could prevent complete rebounds. This is the reason for omitting the phenomenon of water-hammer outside this review section.

4.2.3.3 Further Thoughts

In summary, there are several conditions that determine whether a drop can bounce. The drop has to be fast enough to overcome dissipation and gravity, given by Eqn. (4.5) and Eqn. (4.6), respectively. However, to avoid triggering one of the possible transitions to the sticky Wenzel state, We has to be smaller than the lower of We_{sag} and We_{slide}, given by Eqn. (4.8) and Eqn. (4.10), respectively. The literature mentioned so far in this section implies that as soon as either of these collapse thresholds are met, the collapse occurs irreversibly, instantaneously, and inevitably.

However, it is in fact conceivable that the wetting scenario can be different: The process of sliding down the posts should take a certain time, instead of happening instantaneously, and if the contact angle is high enough it should even be possible to withdraw the liquid, as the example Fig. 4.4 of the experiments performed by our collaborators indicates. The findings of Hyväluoma and Timonen confirm this. In their numerical studies [142, 143] the sliding-down motion is not instantaneous, and the drop is able to withdraw the liquid after touching the base – even at a moderate intrinsic contact angle (113° and 112°, respectively). Such behaviour is not accounted for by the established collapse transition models, as discussed in [133].

This observation is vital for the research presented in this chapter – and there is an elementary extension to it: not only does the interface take a certain time to penetrate the posts, it should in fact be slowing down in the process, as the pressure $p_D \sim \rho v_0^2$ must decrease during the spreading of the drop when horizontal spreading motion sets in above the posts. On the other hand, the upward force from capillarity, which is simply $p_c A_p$ according to Eqn. (4.9), is constant, which means that arrest and reversal of the impinging motion should even be possible, which can also be seen in Fig. 4.4. We will revisit this idea in Ch. 5, where we approach impingement from a kinematic point of view

in Sec. 5.1.1.

4.3 Simulations

In Sec. 4.1.1 the initial pancake bouncing experiments were presented which formed the starting point of the research discussed in this chapter. To access and understand the relevant mechanisms of the pancake effect, we performed numerical simulations of drop impact on a simplified surface, a pillar substrate, which in turn inspired new experiments that allowed us to study the pancake effect more easily on such surfaces. In this section, we describe these simulations, including the simulation geometry and the range of impact and substrate parameters used. The initial conditions for the simulations are discussed in detail, as they proved a challenge for the given simulation parameters.

4.3.1 Geometry

To support the experimental work, we performed quasi-2D lattice Boltzmann simulations for a binary liquid (see Ch. 2), in which both phases have the same density, but different viscosities.

Drop impact experiments are naturally three-dimensional, but for numerical simulations a two-dimensional setup is more computationally feasible than a three-dimensional one. However, to allow for three-dimensional surface features, such as posts, to be simulated, a quasi-2D geometry has to be used. An example of such a geometry is shown in Fig. 4.7a. The drop has a spherical shape in the x-z-plane and is translationally invariant in y direction, giving it a cylindrical shape when unperturbed by a surface. When the drop comes in contact with a patterned surface, it can interact with the three-dimensional features of the surface pattern, permitting flow in y direction and de-pinning, reproducing important properties of the three-dimensional situation. An example of this is shown in Fig. 4.7b.

The substrate was set up as a rectangular lattice of square posts of side length r and height h_p, arranged with lattice constants w_x and w_y along the x and y direction,

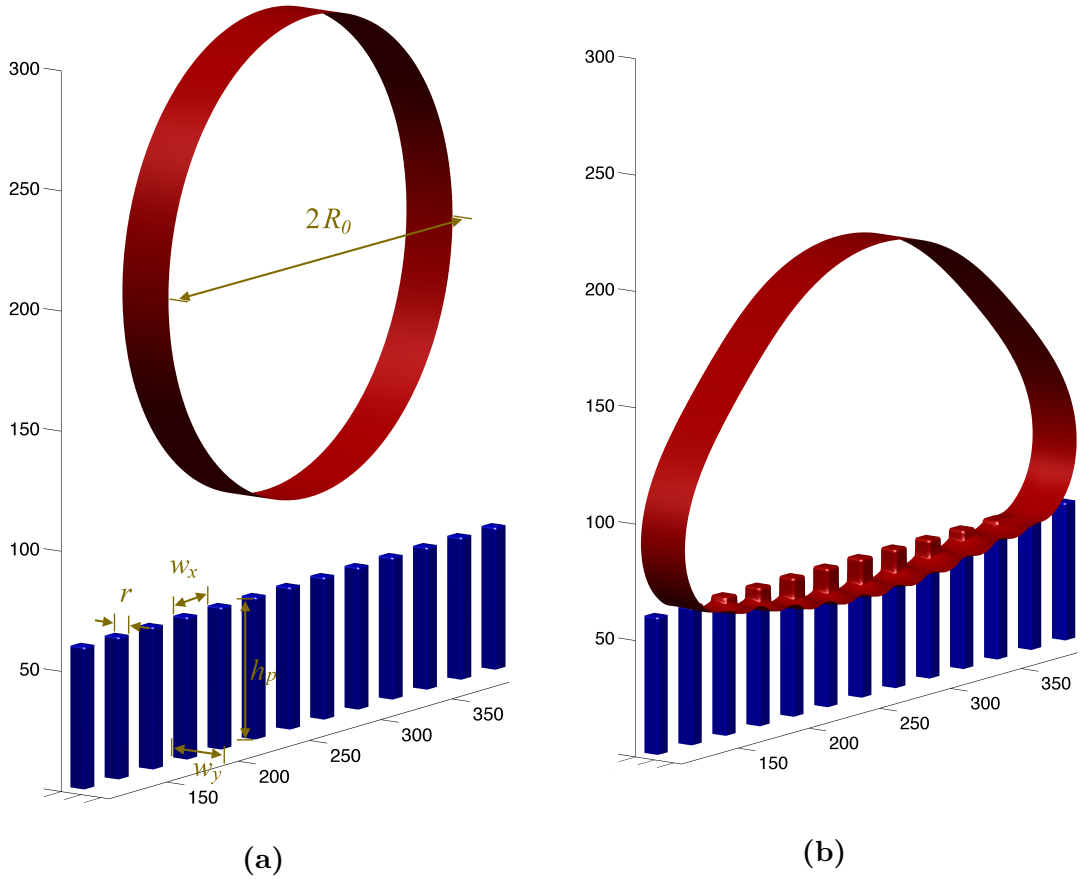


Figure 4.7: Quasi-2D simulation geometry, showing (a) an unperturbed cylindrical drop of radius R_0 above the substrate and (b) the drop interacting with the 3D substrate.

respectively. Periodic boundary conditions were applied in the x, y, and z direction.

4.3.2 Simulation Parameters

The quasi-2D lattice Boltzmann simulations were used to explore the impact behaviour of droplets for varying parameters. Simulations with different surface parameters, liquid parameters, and impact velocities were run, as listed below. Only one parameter was varied at a time, and the default values are given in brackets.

- Drop radius $R_0 = 60 \ldots 120$ (100)
- Surface tension $\sigma = 0.023 \ldots 0.046$ (0.032)
- Intrinsic contact angle $\theta_Y = 140° \ldots 175°$ (150)
- Impact velocity $v_0 = 0.01 \ldots 0.055$ (0.02, 0.03)
- Post width $r = 6 \ldots 14$ (8)
- Centre-to-centre spacing of posts (lattice constant) $w_{x,y} = 18 \ldots 30$ (24)

The height of the posts h_p was chosen sufficiently large that the impacting liquid could penetrate the posts without reaching the bottom. In fact, the substrate had to be set up without a base, to permit gas flow through the substrate. Otherwise the gas phase, perturbed by the motion of the droplet, would push upwards upon collision with the surface, and, due to its inertia, have a cushion-like effect, leading to an effective arrest of the drop's downward motion. This is a consequence of the gas phase having the same density, and hence inertia, as the liquid phase in the lattice Boltzmann binary model.

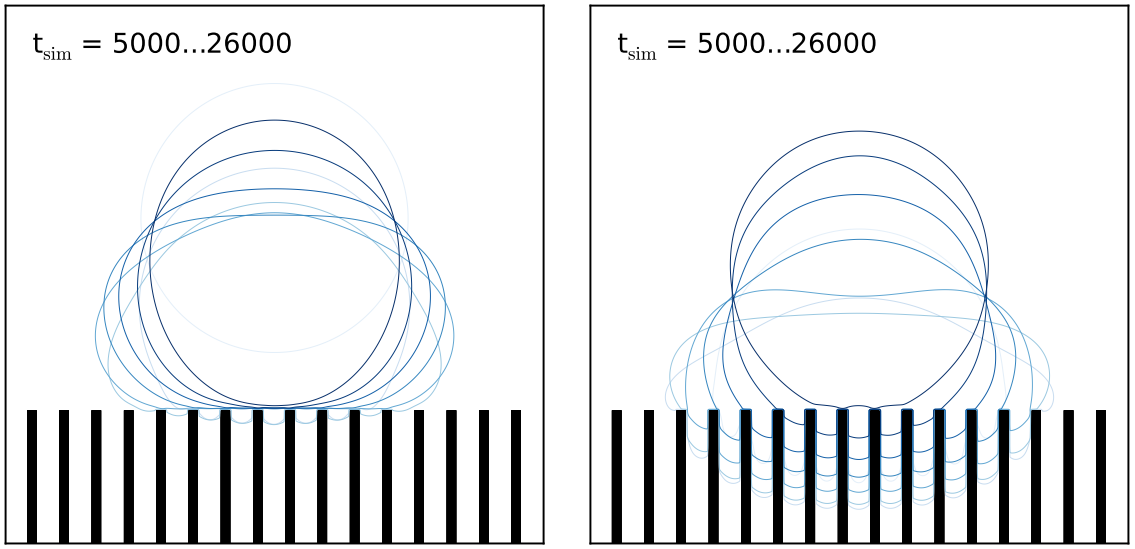
The measures of the simulation box were $L_x = 500$, $L_y = w_y$, $L_z = 600$ lattice points in x, y, and z direction. The width of the diffuse interface in the lattice Boltzmann simulations was, with $\kappa = 0.07$ and $A = 0.0168$, $\xi = 5.77$, smaller than the post width. The viscosities of both phases, given $\tau_l = 1$ and $\tau_g = 0.6$, were $\eta_l = 0.5/3$ and $\eta_g = 0.1/3$, respectively.

4.3.3 Initial Conditions

Given the characteristics of the binary model, which represents the physical liquid and a gas phase by two fluids of equal density, special attention had to be paid to the initial conditions, especially when considering a range of substrate parameters. To simulate drop impact, the cylinder-shaped drop has to hit the substrate with a given impact velocity. This was done by starting the drop above the surface, but with a velocity v_{init}. The drop's initial position had to be sufficiently high above the surface, to allow the liquid-gas interface to relax into its equilibrium configuration before interacting with the substrate. This is because the two phases are initiated with $\phi = \pm 1$, with a sharp boundary, which takes a certain time (depending on simulation parameters) to equilibrate to the natural tanh-configuration.

The initial velocity was applied to both the liquid *and* the gas as otherwise, again due to the 'cushion' effect described in Sec. 4.3.2, the perturbed gas phase would halt the drop before it can reach the posts. Given an initial velocity, the gas squeezes vertically through the array of posts, dissipating energy, and thus slowing down the motion of the liquid and gas together. For varying substrate parameters r and $w_{x,y}$ v_{init} was adjusted by trial and error to achieve the same impact speed.

Besides a substrate formed by an array of posts we also used a substrate consisting of horizontal beams and one mimicking the MTS substrate by using square cells rather than posts. We were interested in the question of whether the vertical direction of the posts facilitates pancake bouncing by channeling the liquid, or whether the phenomenon appears without such geometric aids. The results will be discussed as part of the outlook in Ch. 5, Sec. 5.4.



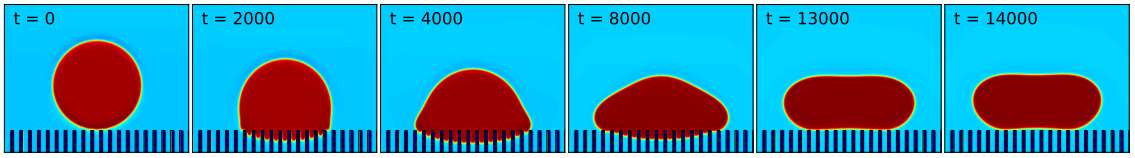
(a) **(b)**

Figure 4.8: Evolution of the drop shape in lattice Boltzmann simulations during an impact with different impact velocities. (a) $We = 1.3$, with $v_0 = 0.020$ and default parameters, (b) $We = 9.5$, with $v_0 = 0.055$ and default parameters. The lines indicate the contour where $\phi = 0$, the middle of the diffuse interface. The layer $y = 4$ cutting through the centre of the posts is shown, for 400×400 out of the 500×600 lattice nodes. Time runs from light to dark blue in steps of 3000 (in lattice units).

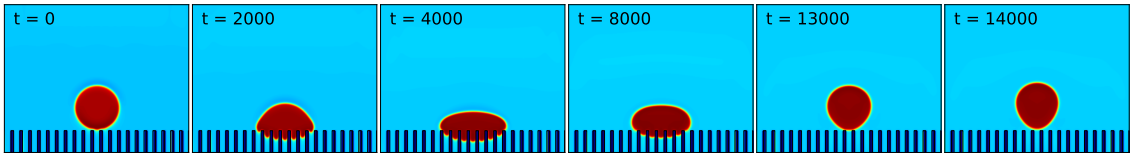
4.4 Simulation Results

4.4.1 Examples

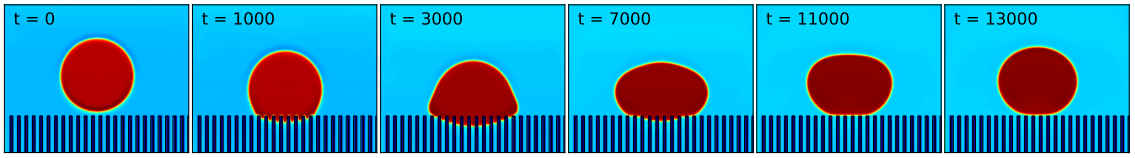
The simulations described in the previous section provide a useful tool to study the drop impact process. In Fig. 4.8 we present two examples of drop impact events at impact velocities $v_0 = 0.020$ and $v_0 = 0.055$, corresponding to $We = 1.3$ and 9.5, respectively. All other parameters are the default ones indicated in the list in Sec. 4.3.2. We plot the contour of the drop in the layer $y = 4$ which cuts through the middle of the posts, changing over time, from light blue to dark blue, for simulation steps between $t_{\text{sim}} = 5000$ and $t_{\text{sim}} = 25000$. As discussed in Sec. 4.2.3.3, it can be clearly seen that the liquid penetrates the structure first, followed by a reversal of the imbibition process due to the highly hydrophobic posts. The higher impact velocity leads to significant penetration between the posts, and to a more distorted body of the drop above the surface. The higher degree of penetration in Fig. 4.8b also has the effect that the liquid takes much



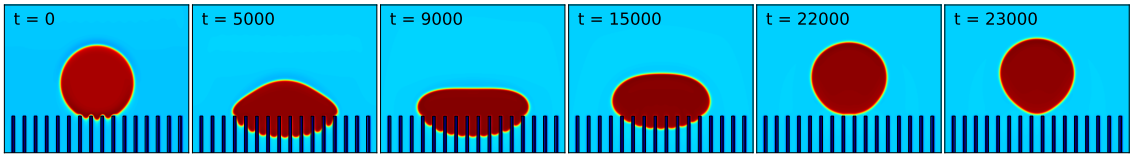
(a)



(b)



(c)



(d)

Figure 4.9: Time sequences of the bouncing process in lattice Boltzmann simulations. In each sequence, the next-to-last time step shows the approximate moment of detaching. (a) $We = 3.15$, $R_0 = 120$, $w_{x,y} = 24$: pancake bouncing is observed. (b)$We = 1.80$, smaller $R_0 = 60$: no pancake effect. (c) $We = 2.80$, $R_0 = 100$, smaller post spacing of $w_x = w_y = 20$: pancake bouncing, although overall spreading is small. (d) $We = 2.80$, $R_0 = 100$, bigger post spacing of $w_x = w_y = 30$: overall spreading is large, but drop retracts before lift-off. Parameters are given in lattice units. In these plots $t = 0$ does not exactly correspond to the moment when the drop touches the surface, however in the analysis $t = 0$ is the exact time when the drop attaches.

longer to empty the structure.

Besides allowing us to study the general characteristics of the drop impact, our simulations also proved successful in reproducing the pancake effect we are interested in. Our simulations indeed exhibit a full rebound of the impacting drop and, depending on the simulation parameters, show lift-off in an elongated shape, i.e. pancake bouncing.

Examples are given in Fig. 4.9. The figure shows a selection of time sequences of the order parameter field, that is the liquid-gas configuration, for different parameters. The layer $y = 4$ is plotted, cutting through the centres of the posts. The size of the simulation box was 500×600, but only the lower 500×400 lattice points are shown here.

In Fig. 4.9a we can observe pancake bouncing, the drop is close to its maximum width as it leaves the surface. The parameters used were: $R_0 = 120$, $\sigma = 0.032$, $v_0 \approx 0.03$ ($We = 3.15$), $\theta_Y = 150°$, $r = 8$, $w_x = w_y = 24$. In Fig. 4.9b $R_0 = 60$ ($We = 1.80$), otherwise the same parameters apply. The pancake phenomenon has diappeared for this smaller drop size, and the drop lifts off in an almost spherical shape. Note that the liquid spends about the same amount of time impinged in the structure, whereas the dynamics of the body of liquid above the surface is different. Fig. 4.9c shows a drop of intermediate size $R_0 = 100$ ($We = 2.80$), but here the substrate parameters are changed, the posts have a closer spacing of $w_x = w_y = 20$, and in Fig. 4.9d the spacing is wider than before, $w_x = w_y = 30$. In Fig. 4.9c the drop spreads out less than in the panels above, whereas in Fig. 4.9d the spreading is wider. However, in Fig. 4.9d the drop retracts sideways before it lifts off the surface, whereas in Fig. 4.9c it leaves the surface whilst still elongated (although the maximum elongation is small).

4.4.2 General idea of bouncing mechanism

In the following sections we will explore the reasons behind this bouncing behaviour. In order to do this, it is helpful to first define some nomenclature in Sec. 4.4.2.1. Guided by examples of the evolution of geometric parameters during the impact process, we will present the key ideas of the pancake bouncing mechanism in Sec. 4.4.2.2 by identifying

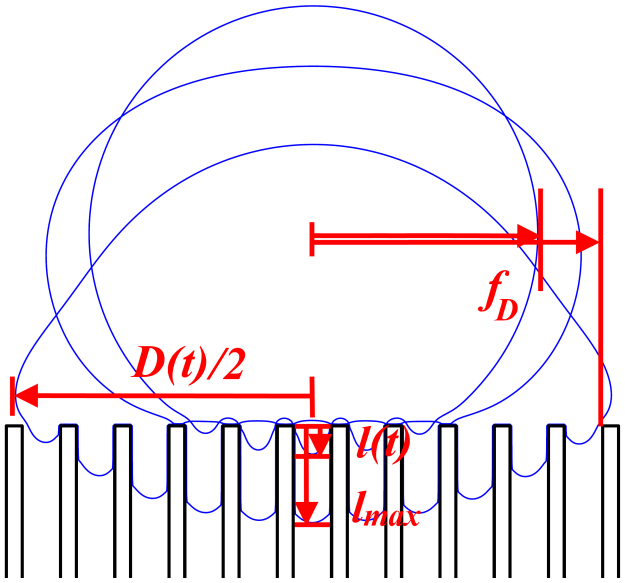


Figure 4.10: Diagram to clarify $D(t)$, $l(t)$, and the meaning of f_D (see Sec. 5.1.1).

two criteria for bouncing. We then show in Sec. 4.4.2.3, that these criteria are indeed independent and therefore can be modeled separately.

4.4.2.1 A Few Definitions

We denote the lateral width of the drop, at its locally widest extension, by $D = D(t)$ (accordingly R is the radius, $R = \frac{1}{2}D$), as shown in Fig. 4.10. We define the pancake 'quality' p of a bouncing event by the drop's elongation at the moment of jumping D_{jump} relative to the maximum width the drop reaches during the entire spreading process D_{max}. Hence

$$p := \frac{D_{jump}}{D_{max}}. \tag{4.11}$$

The respective times t at which this happens are t_{jump} and t_{max}. All times are shifted such that $t = t_0 = 0$ at the moment when the drop first touches the surface.

When we speak of the liquid impinging the substrate and emptying it, we use the term *recoiling* for the vertical emptying process, whereas the horizontal receding movement of the body of liquid above the surface will be described as *retraction*.

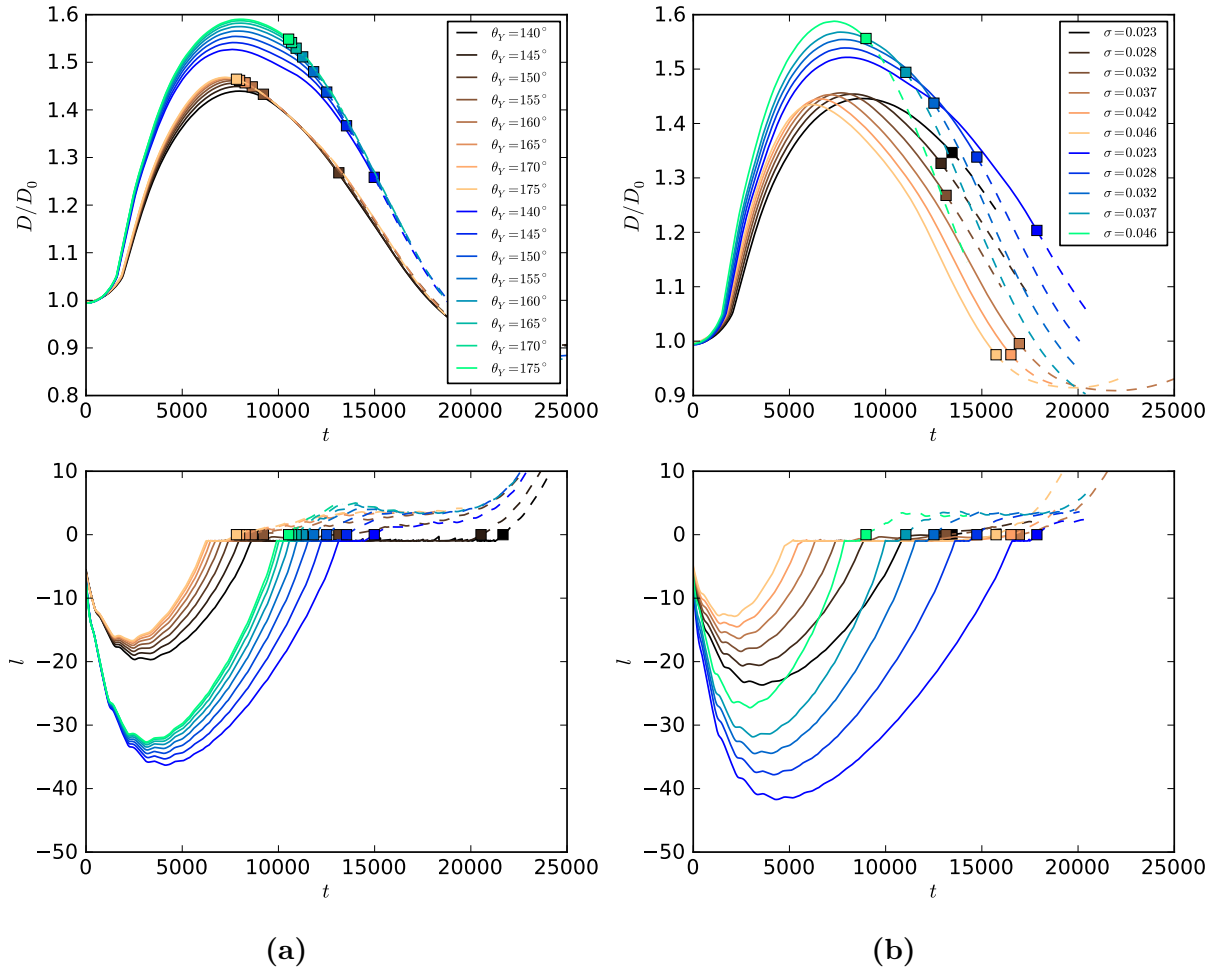


Figure 4.11: Evolution of drop width $D(t)$ (top) and penetration depth $l(t)$ (bottom) at two different impact velocities $v_0 \approx 0.02$ (copper-shaded graphs) and $v_0 \approx 0.03$ (blue-green-shaded graphs) for (a) varying intrinsic contact angles θ_Y and (b) varying surface tensions σ. The squares indicate the moment of detaching from the surface, dashed lines denote the evolution after lift-off.

4.4.2.2 Two Criteria

The sequences in Fig. 4.9 already give a hint about the key point in understanding the pancake bouncing mechanism – the coupling between the liquid's down-and-up motion between the posts and the spreading of the body of liquid above the surface. When the drop impinges on the superhydrophobic surface a portion of liquid moves down between the posts because of the liquid's vertical momentum. This portion of the drop is decelerated, and comes to rest, because of the capillary force exerted by the hydrophobic posts. Part of the drop's initial kinetic energy is stored as wetting energy due to the interaction of liquid with the hydrophobic solid. The impinged liquid is then accelerated

upwards and the wetting energy is converted to kinetic energy, the process of capillary emptying. If, when the liquid reaches the top of the posts, the drop has a sufficient net vertical kinetic energy, the drop can lift off and bouncing occurs.

For this bouncing to happen in a pancake shape, two criteria must be satisfied. The first of these concerns time scales and the second the energy of the drop. We consider each in turn.

Time scales The upwards momentum that causes bouncing must be transmitted to the drop before it retracts. Fig. 4.11 shows two examples of the time evolution of the horizontal spread $D(t)$ and the depth of penetration into the solid structure, $l(t)$, where $l(t)$ is the maximum penetration at any point across the width of the drop, typically in the middle, as depicted in Fig. 4.10. In Fig. 4.11a, the retraction is not affected by a variation of the contact angle. However, the time at which the liquid has recoiled from the posts (corresponding to $l = 0$ in the figure), affects at what stage of the retraction process the drop detaches from the surface. Consider the blue-green curves in Fig. 4.11a: For $l(t)$ (bottom panel) the amount of penetration depends on θ_Y, and so does the speed of recoiling. Hence, the moment at which the liquid reaches the top of the posts, $t_\uparrow$, which appears as a kink in the $l(t)$ graph, depends on θ_Y as does the moment of jumping, which is indicated by a square symbol. Therefore, the drop detaches at different stages of the retraction motion. For high contact angles, corresponding to the green curves, jumping happens just after the drop has reached its maximum extension, whereas for low contact angles, given as blue curves, the drop has retracted significantly when it lifts off the surface. Therefore, if the time scales of recoiling and spreading match, the liquid empties the structure as it is extended maximally. The difference in the maximum spreading diameter is due to the coupling with the imbibition process. If more liquid is imbibed vertically, there is less liquid in the body of the droplet above the posts to spread horizontally.

The same observation of matching time scales is true for the blue-green curves in Fig. 4.11b, where we changed the surface tension σ. The difference here is that the

retraction dynamics $D(t)$ also depends on σ. This is expected as the maximum extension D_{max} and the spreading dynamics, manifested in the drop oscillation time T_{osc}, depend on σ according to Eqn. (4.4) and Eqn. (4.2), respectively.

From the discussion of Fig. 4.11 we can conclude that if the liquid has finished emptying the posts just as the drop reaches its maximum extension, the drop may jump as a pancake. This argument of matching time scales forms the time scale criterion. A useful measure for this criterion is the ratio k of the time the liquid takes to return to the surface $t_{\uparrow}$ to the time at which maximum spreading occurs t_{max}

$$k := \frac{t_{\uparrow}}{t_{max}}. \tag{4.12}$$

For $k = 1$ there is no retraction before lift-off and therefore the pancake quality $p = \frac{D_{jump}}{D_{max}} = 1$, corresponding to a 'perfect' pancake. With increasing $k > 1$ the drop will retract partially and $p < 1$. The case $k < 1$ was not realised by our simulations, but does occur in the experiments performed by our collaborators. For $k < 1$, the liquid recoils too early, when the drop is still in the process of spreading out. The experiments indicate that, at this point, there is still considerable momentum downwards within the body of the drop, which arrests the upward momentum from the recoil. Therefore, the drop does not jump at $t_{\uparrow}$ for $k < 1$.

Energy The second criterion for pancake bouncing concerns the energy of the drop. After emptying the structure, the drop's kinetic energy of upwards movement must be sufficient to lift the drop off the surface. If the energy is not enough at the time of recoiling, the drop will continue to retract until the surface energy released by the retraction process is sufficient to enable the drop to detach from the substrate. An example of such behaviour is given in Fig. 4.8a which has $We = 1.3$. We will refer to this condition as the 'energy criterion'.

In terms of measured geometric quantities, the energy criterion can be observed in the copper-shaded sets of plots in Fig. 4.11a and Fig. 4.11b. Consider Fig. 4.11b. The

copper-shaded graphs are at lower velocity $v_0 \approx 0.02$ than the blue-green ones, $v_0 \approx 0.03$. This corresponds to a lower range of Weber numbers of $We = 0.8 \ldots 1.7$ for the copper curves, instead of $We = 1.9 \ldots 3.8$ for the blue-green curves. Consider the graphs for $\sigma = 0.048$, 0.036, and 0.032, the lightest shades: the liquid returns to the surface ($l = 0$) very quickly, owing to the strong capillary force, but then it stays there before the actual lift-off happens at t_{jump}, denoted by a square symbol. By t_{jump}, the drop has retracted considerably, resulting in a small D_{jump} and hence small pancake quality $p = D_{jump}/D_{max}$. In Fig. 4.11a the same observation holds for the three darkest graphs in the copper-shaded curves, corresponding to lower contact angles of $\theta_Y = 140°$, 145°, and 150°. Here the Weber number of impact does not differ from the other curves, but it is the increased dissipation due to a lower contact angle that causes the energy to be too small for immediate jump.

4.4.2.3 Independence of Criteria

In Fig. 4.12, top panels, we plot $p = D_{jump}/D_{max}$ as a function of k. The plots on the left hand side show simulation results, the right hand side experimental data. The overall pancake quality p, plotted in the top panels, is a result of both the time scale and the energy criterion, hence it is not straightforward to understand. Yet, one can disentangle the effects of both criteria by plotting slightly different quantities.

To see the time scale criterion we plot an 'intermediate' pancake quality, the relative width $D_\uparrow$ at the time of *recoiling* (i.e. when the imbibed liquid reaches the top of the posts again), $t_\uparrow$, instead of actual jumping

$$p_\uparrow := \frac{D_\uparrow}{D_{max}}. \tag{4.13}$$

This way, we see if the liquid returns to the surface whilst the drop is still in a pancake shape, irrespective of whether it can jump. This is plotted in Fig. 4.12, middle panels. For both simulations and experiments we can confirm that at $k = 1$ the intermediate pancake quality is at its maximum, $p_\uparrow = 1$. Both for the middle and the top panels,

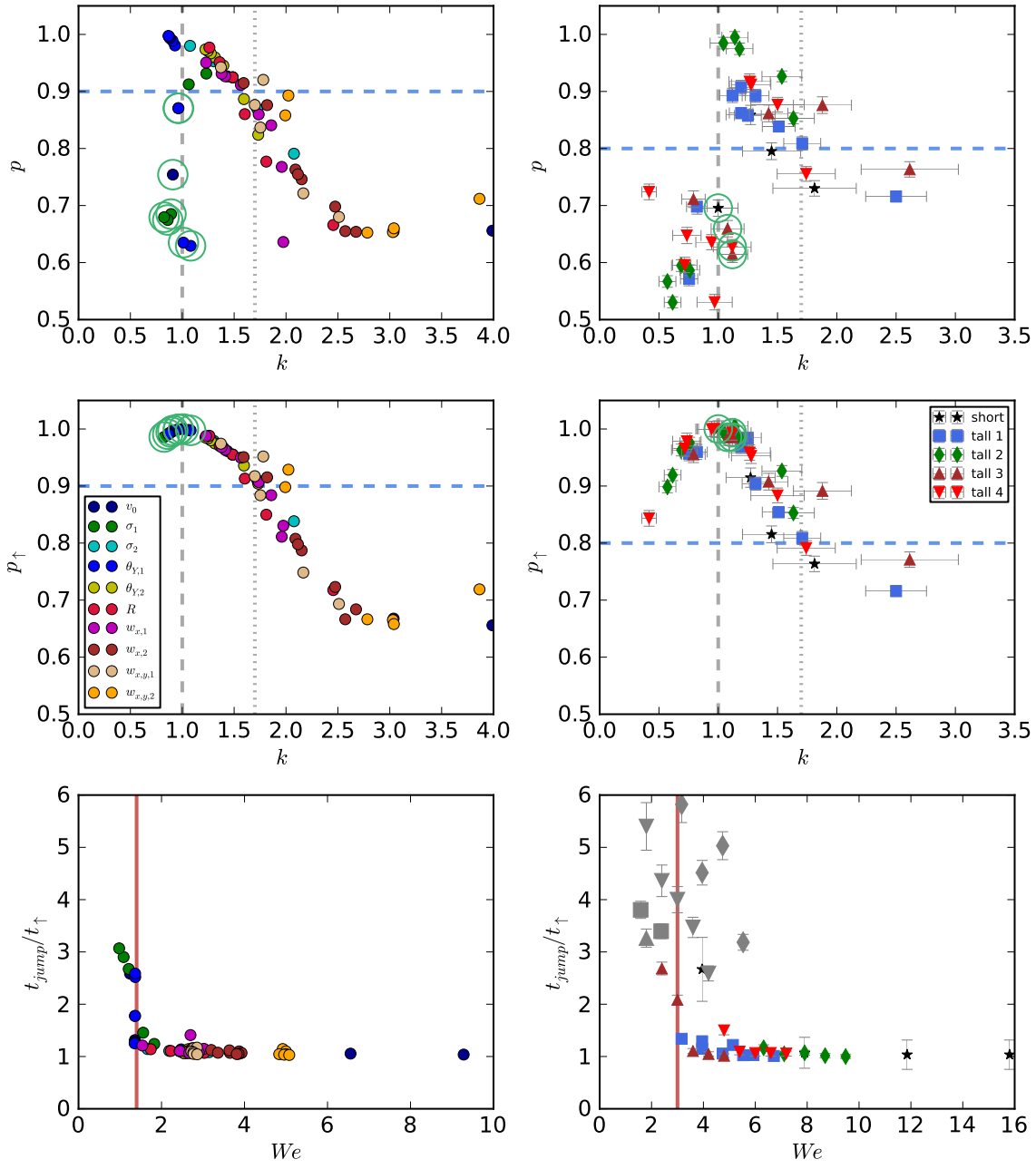


Figure 4.12: Simulation results (left side) and experimental results (right side) for the pancake effect. Top panels: overall pancake quality p, resulting from both time scale and energy criteria. Middle panels: time scale criterion, decoupled from the energy criterion. The intermediate pancake quality at recoiling $p_\uparrow$ is plotted against the ratio of time scales k. Bottom panels: energy criterion, decoupled from the time scale criterion. The relative waiting time on top of the structure, t_{jump}/t_{jump} is plotted against the energy of the drop, expressed as the Weber number We. Blue dashed line: $p = p^*$, grey dashed line: $k = 1$, grey dotted line: $k = k^*$, red solid line $We_c = 1$. Green circles indicate those data points which are affected by the energy criterion. The parameters for the different data sets indicated in the legend are given in Tab. 5.2 and Tab. 5.3, respectively.

the grey vertical line is the $k = 1$ boundary. The blue horizontal line shows the cutoff p^* above which we define a drop as 'pancake' – for $p < p^*$ we consider the rebound 'conventional'. In simulations we chose $p^* = 0.9$ and for the experimental data $p^* = 0.8$. This is so that the cutoff in k (grey dotted line) is at the same value of $k^* = 1.7$ for both. The difference in the steepness of both graphs is because we are comparing 2D and 3D results. The physical three dimensional drop should retract faster because an increase in D corresponds to a bigger increase in surface area than in the 2D simulations. Moreover, a dense surrounding liquid, as is the case in our simulations, should slow down the dynamics, as discussed in Sec. 4.2.1 and in [127, 129].

In the bottom graphs of Fig. 4.12 we show the energy criterion, separated from the time scale criterion. A useful measure to quantify the idea of the energy criterion is the time the drop sits on top of the posts before it actually lifts off. Therefore we use $\frac{t_{jump}}{t_\uparrow}$ and plot it versus the Weber number. As this is dimensionless it allows us to compare experiments and simulations and is therefore more helpful that the difference $t_{jump} - t_\uparrow$. When the kinetic energy, and therefore the Weber number,drops below a threshold value We_c, the critical Weber number for the energy criterion, there is an abrupt increase in the time the drop spends on the surface, i.e. it cannot jump directly after recoiling. We_c is indicated by the red solid line in Fig. 4.12.

The two effects of the time scale and energy criteria, plotted in the middle and bottom panels, respectively, together lead to the behaviour of the data in the top panels of Fig. 4.12. For those drops which do not have sufficient energy and hence spend some time retracting first, the overall pancake quality at detachment decreases from $p_\uparrow$ in the middle panel to a considerably lower p in the top panel. Those drops are marked with green circles in both plots.

In the experimental plots, the data points for $k < 1$ show a low pancake quality p because the drop is prevented from jumping due to the downwards flow. Therefore, it also retracts and jumps at $t_{jump} \gg t_\uparrow$, but this effect is not necessarily due to a lack of kinetic energy. Hence, the respective data points with $k < 1$ are not suited to indicate the threshold in energy, and are plotted in grey colour, for reference only.

The reader may note that in the simulation data, Fig. 4.12, top panel, left side, there are also some data points with $k < 1$, which nevertheless have $p \approx 1$. This is because in the simulations the $t_\uparrow$ in $k = t_\uparrow / t_{max}$ can only be measured *just before* the bottom of the impinging liquid reaches the surface due to the curvature of the liquid-gas interface below the drop (recall that l is the maximum extension of liquid into the substrate). We use the moment when the liquid arrives one lattice node below the surface of the posts. This means that the data points are shifted slightly to the left. In the middle panel the effect is balanced out since $D_\uparrow$ is also measured just before the actual recoiling time.

To summarise, both matching time scales and sufficient energy are individually necessary, but not sufficient, conditions for the occurrence of pancake bouncing. Our discussion above has proved that they are two separate conditions which together result in the complicated behaviour for pancake bouncing. As a result, we can derive a theoretical framework for each criterion separately. This will be done in the next Chapter of this thesis.

Chapter 5

Theory of Pancake Bouncing

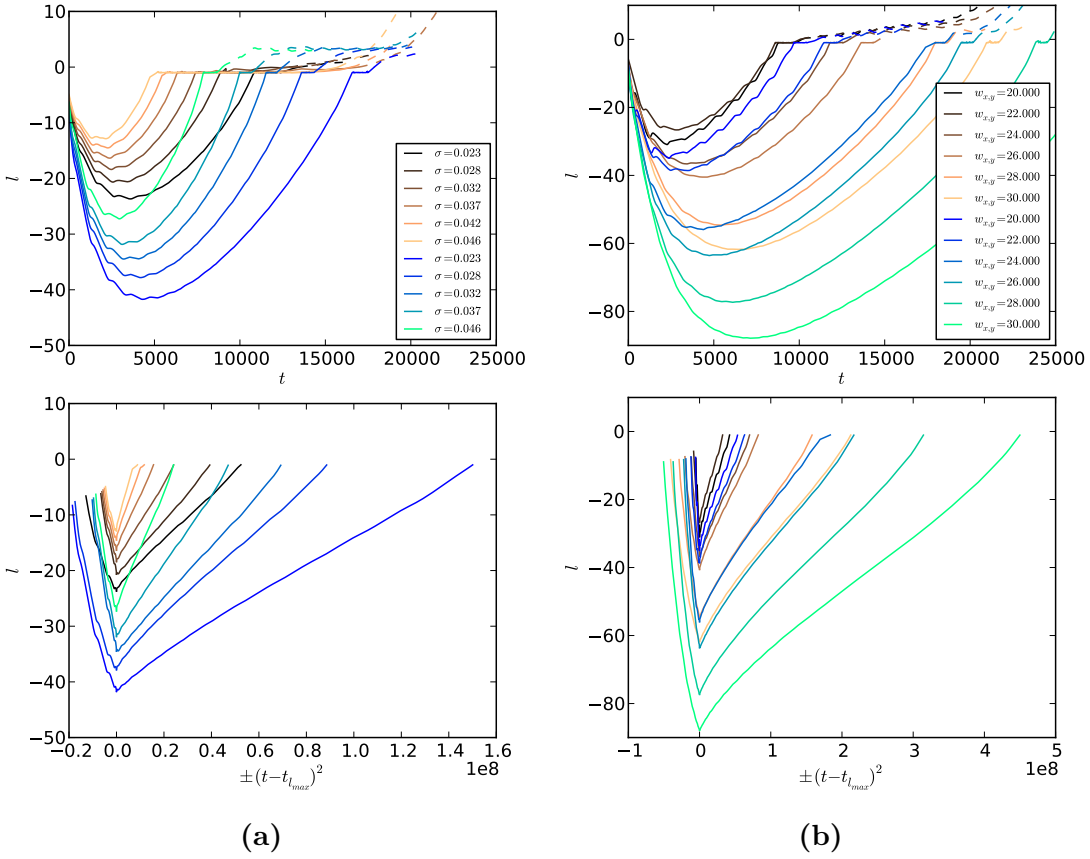
5.1 Theoretical Model

In this section we relate the time scale and energy criteria identified in Sec. 4.4.2 to surface and drop parameters to gain insight into the bouncing process. We aim to identify conditions on these parameters that lead to pancake bouncing. In Sec. 5.1.1 we consider the time scale criterion and in Sec. 5.1.2 the energy criterion. In deriving expressions for the two criteria we will consider the 2D geometry of the simulations and the 3D geometry of the experiments in parallel. We present the results of the theoretical framework in Sec. 5.2 and use them to explain the experimental observations described in Sec. 4.1.3. In Sec. 5.3 we discuss the assumptions we used to derive our theoretical model. Sec. 5.4 summarises our findings on the pancake effect.

5.1.1 Derivation of the Time Scale Criterion

Exact calculations of $t_{\uparrow}$ and t_{max} are not feasible because there is obvious coupling between the penetration motion and the spreading dynamics of the drop. However, we can make good estimates of the relevance of different parameters to the problem.

As outlined in Sec. 4.2.3.3, we approach the problem of liquid impingement dynamics from a kinematic point of view, assuming that the liquid's motion down and up between the posts can be treated by simple kinematics. In doing this we implicitly assume that



(a) **(b)**

Figure 5.1: Dependence of l on time and on the squared time, normalised by $t_{l_{max}}$ for (a) varying intrinsic contact angles θ_Y at $v_0 \approx 0.02$ (copper-shaded graphs) and $v_0 \approx 0.03$ (blue-green-shaded graphs) and (b) varying post spacings $w_x = w_y$ at impact velocities $v_0 \approx 0.25$ (copper-shaded graphs), $v_0 \approx 0.035$ (blue-green-shaded graphs).

the liquid slides down the sides of the posts and is not pinned to the tops of the posts. According to Eqn. (4.10) this is the case for $We > 1.35$ in the simulations. We used $We > 1 \ldots 10$ and our results suggest that the interface does indeed de-pin from the posts even for small We. For experiments, we used $We > We_{slide}$ and the videos of the impact process confirm that the liquid enters the posts and does not stay pinned to the tops.

Consider Fig. 5.1 where two examples of the time evolution of the penetration depth are plotted. The top panels show the dependence on t. For each part of the graph, for $t < t_{l_{max}}$ and $t > t_{l_{max}}$, where $t_{l_{max}}$ denotes the time at which the penetration is maximal (see Fig. 4.10), the graphs are approximately of the form $l = \frac{1}{2}at^2$, corresponding to simple motion with a constant acceleration a (with an initial velocity for $t < t_{l_{max}}$).

To support the idea of constant acceleration we plot l as a function of the squared time,

normalised by $t_{l_{max}}$ in the bottom panels of Fig. 5.1. The graphs are not strictly linear in each section, but nevertheless we will use the approximation of constant acceleration – after all, in Fig. 5.1 we are characterising the complicated process of a volume of liquid penetrating posts by the dynamics of the local minimum of the droplet only, and some deviations are to be expected.

The liquid moving down between the posts is decelerated by a capillary force, which can readily be written down from the discussion in Sec. 4.2.3.1. The perimeter of each square post is $4r$, where r denotes the width of the post. Similarly to Eqn. (4.9), the contact line around this perimeter exerts a force $4r\sigma\cos\theta_Y$ on the column of liquid in its unit cell, so the overall force applied to the drop by the wetted posts is

$$F_c = -4r\sigma\cos\theta_Y n, \tag{5.1}$$

where n is the number of columns between posts that are wetted. This capillary force points upwards, out of the substrate, for hydrophobic surfaces where $\cos\theta_Y < 0$.

The acceleration the liquid experiences whilst moving down $a_\downarrow$ and up $a_\uparrow$ is then the capillary force, divided by the mass. The different slopes in Fig. 5.1 for $t < t_{l_{max}}$ and $t > t_{l_{max}}$ indicate that these masses are different, as the force itself cannot differ for imbibition and recoiling in a framework where the advancing and receding contact angles are equal to the equilibrium contact angle of the posts, as is the case in our simulations. The deceleration whilst moving down $a_\downarrow$ and the acceleration whilst moving up $a_\uparrow$ are therefore given by

$$a_\downarrow = \frac{-\sigma n 4r\cos\theta_Y}{m_\downarrow}, \tag{5.2a}$$

$$a_\uparrow = \frac{-\sigma n 4r\cos\theta_Y}{m_\uparrow},, \tag{5.2b}$$

where $m_\downarrow$ and $m_\uparrow$ are the amounts of liquid mass that are decelerated whilst going down, and accelerated whilst moving up, respectively. In the experiments there is little difference between $t_{l_{max}}$ and $t_\uparrow - t_{l_{max}}$, indicating that the masses may be different, but

not considerably. In simulations however we find $a_\downarrow$ exceeds $a_\uparrow$ by a factor of the order of five. Moreover, the calculated acceleration exceeds the measured one by a large amount, typically by a factor of the order of ten. We model this by taking $m_\downarrow$ and $m_\uparrow$ to be effective masses

$$m_\downarrow = f_\downarrow m, \tag{5.3a}$$

$$m_\uparrow = f_\uparrow m, \tag{5.3b}$$

where $f_\downarrow$ and $f_\uparrow$ are scaling factors that account for the difference to the actual drop mass. Their orders of magnitude are $f_\downarrow \approx 2$, $f_\uparrow \approx 10$ for simulations ($f_\downarrow \approx f_\uparrow \approx 1$ for experiments), but both should depend on the simulation parameters. Further justification of this assumption and of the size of $f_\downarrow$ and $f_\uparrow$ is deferred to Sec. 5.3.4.

Then the basic kinematic laws for uniformly accelerated motion allow us to calculate the time $t_\uparrow$ for the penetration l to reach its maximum depth l_{max} and to return to zero, i.e. for the liquid to imbibe and empty the post structure again.

$$t_\uparrow = \frac{v_0 m(f_\downarrow + \sqrt{f_\downarrow f_\uparrow})}{-n4r\cos\theta_Y}. \tag{5.4}$$

n, the number of columns between posts that are wetted, should scale with the absolute size of the drop, and with the spacing of the posts. For the 2D simulations and 3D experiments we use

$$\text{sim}: \quad n = f_D \frac{2R_0}{w_x}, \tag{5.5a}$$

$$\text{exp}: \quad n = f_D^2 \frac{R_0^2}{w_x w_y}, \tag{5.5b}$$

where we again employ a scaling factor f_D. It accounts for the width of the wetted arc-shaped region under the drop as shown in Fig. 4.10. Typically $f_D \approx 1$, but it depends on the simulation parameters.

Inserting the respective formulas for the mass in 2D and 3D we arrive at

$$\text{sim}: \quad t_\uparrow \approx -\frac{\pi}{8}\frac{v_0 \rho R_0 w_x w_y}{\sigma r \cos\theta_Y} f_t, \tag{5.6a}$$

$$\text{exp}: \quad t_\uparrow \approx -\frac{1}{3}\frac{v_0 \rho R_0 w_x w_y}{\sigma r \cos\theta_Y} f_t, \tag{5.6b}$$

with a constant prefactor

$$f_t = \frac{f_\downarrow + \sqrt{f_\downarrow f_\uparrow}}{f_D} = \text{const}, \tag{5.7}$$

which incorporates effects from the effective masses moving down and up, the width of the wetted region underneath the drop, and effects from dissipation, which are not negligible in the simulations. In doing this we make the assumption that the width of the wetted region and the effective masses are connected such that their combined effect is a constant for all simulations. This will be verified in Sec. 5.2.

There is also a Laplace force $F_L = -\frac{\zeta \sigma A_p}{R_0} n$, where $A_p = w_x w_y - r^2$ is the surface area of each liquid column between posts. ζ is a dimensional prefactor: for two dimensions $\zeta = 1$, in three dimension $\zeta = 2$. With respect to post imbibition, the Laplace force points downwards, into the structure. It resists the liquid emptying the structure. This, in turn, causes an increase in the liquid-gas interface above the posts which has a radius of $\approx R_0$. To estimate the importance of F_L, for different drop radii F_c exceeds F_L by a factor of 3.3 to 6.6 in simulations, and by a factor of 1.4 to 3.5 in experiments. Therefore, F_c is the dominant force contribution. Moreover, since the local curvature of the drop changes considerably during the process of bouncing, and even goes to zero underneath the drop for a pancake-shaped drop, $F_L = -\frac{\zeta \sigma A_p}{R_0} n$ overestimates the actual contribution of the Laplace force. Therefore, we neglect F_L compared to F_c. This will be discussed further in Sec. 5.3.

In our simulations there is no gravity. In experiments, the effects of gravity are negligible for drop diameters smaller than the capillary length which is about 3 mm for water. For larger drops $-g$ would have to be added to either term in Eqns. (5.2), where g is the gravitational acceleration. The drop radii used in the experiments by

our collaborators are 1.1 and 1.45 mm, so it is reasonable to omit gravity effects in our analysis as deformations caused by the impact are going to be much larger than those caused by gravity.

It is important to note that the equations for the recoil time $t_\uparrow$ are only valid if the liquid can penetrate the posts without hitting the substrate base, as occurs in some of the experiments that were performed. Eqns. (5.6) are not suited to model the penetration behaviour for short posts, as the kinematics leading to Eqns. (5.6) rely on the liquid penetrating the posts as much as its initial velocity allows, without being stopped by the base of the substrate. To distinguish the two cases, if the substrate used has posts so short that the liquid hits the base, we characterise these posts as 'short', whereas otherwise they we call them 'tall'. The substrate in the simulations is set up without a base, but the posts still have to be long enough that the liquid does not imbibe underneath them.

Having found an expression for $t_\uparrow$, our next concern is the spreading time t_{max}. If we neglect the effects of the liquid penetration into the posts, we expect the time for maximum extension to be slightly less than half the bouncing time (see Sec. 5.3.2 for a fuller discussion of this point)

$$t_{max} = \xi_\tau \sqrt{\frac{\rho}{\sigma} R_0^3} = \xi_\tau \tau_{ci}, \tag{5.8}$$

[50, 80, 127], where $\sqrt{\frac{\rho}{\sigma} R_0^3}$ is the usual time scale for capillary-inertial motion, τ_{ci}. Therefore, using Eqns. (5.6) and Eqn. (5.8) and identifying $\rho R_0 v_0^2/\sigma$ as the Weber number *We*, a theoretical prediction for $k = \frac{t_\uparrow}{t_{max}}$ can be written as:

$$\text{sim}: \quad k = \left(\frac{f_t}{\xi_{\tau,\text{2d}}}\right) \frac{\pi w_x w_y}{-8r \cos\theta_Y R_0} \sqrt{We}, \tag{5.9a}$$

$$\text{exp}: \quad k = \left(\frac{f_t}{\xi_{\tau,\text{3d}}}\right) \frac{w_x w_y}{-3r \cos\theta_Y R_0} \sqrt{We}. \tag{5.9b}$$

Applying the time scale criterion $k = \frac{t_\uparrow}{t_{max}} \gtrapprox 1$ and rearranging, this yields:

$$\text{sim}: \quad \sqrt{We} \gtrapprox \left(\frac{\xi_{\tau,2\text{d}}}{f_t}\right) \frac{-8r\cos\theta_Y R_0}{\pi w_x w_y}, \tag{5.10a}$$

$$\text{exp}: \quad \sqrt{We} \gtrapprox \left(\frac{\xi_{\tau,3\text{d}}}{f_t}\right) \frac{-3r\cos\theta_Y R_0}{w_x w_y}. \tag{5.10b}$$

The left hand side is the dimensionless velocity $\sqrt{We} = \sqrt{\frac{\rho}{\sigma} R_0^3}\frac{v_0}{R_0}$.

5.1.2 Derivation of the Energy Criterion

Matching time scales is a necessary, but not sufficient, condition for pancake bouncing as the fluid expelled from the surface must have enough energy to lift the drop.

The total energy available is the initial kinetic energy $E_{K,0}$ plus the surface energy of the initially spherical drop $E_{S,0}$. At the end of the bouncing process, when the drop has just detached, it will have a centre-of-mass kinetic energy

$$E_{K,\text{jump}} = f_K E_{K,0} - (E_{S,\uparrow} - E_{S,0}) = f_K E_{K,0} - \Delta E_S, \tag{5.11}$$

where the initial kinetic energy is reduced due to dissipation and other effects in the bouncing process, by a factor $f_K < 1$. $E_{S,\uparrow}$ denotes the liquid-gas surface energy of a drop that has just detached.

In the literature, using energy conservation for drop bouncing problems is strongly questioned (see Sec. 4.2.2). For millimetric water drops bouncing on flat or superhydrophic surfaces viscous dissipation is usually neglected as the Reynolds number of the spreading process is considerably larger than one, or $Oh = \frac{\eta}{\sqrt{\rho\sigma R_0}} \ll 1$, which is a better measure for this process that involves capillary forces [54]. Indeed, for our simulations typically $Oh \approx 0.09$ and in the experiments $Oh \approx 0.003 \ll 1$.

However, vortical motion is observed inside the drop [50] which carries kinetic energy and hence should be entered into the energy balance. Yet, in our simulations we do not observe strong vortical motion – as the drop moves upwards recoiling from the posts, flow in z direction dominates the flow field, as will be verified in Sec. 5.3.5.

Viscous dissipation is however much more pronounced in our problem than in conventional bouncing experiments, as the liquid penetrates structures that are considerably smaller than R_0. An estimate of the Reynolds number associated with penetration $Re \approx \frac{v_0(w-a)\rho}{\eta}$ is of the order of unity for simulations, with $Re = 1.5 \ldots 5.3$. Therefore, viscosity effects will not be dominant, yet viscous dissipation should not be negligible in the energy balance. In experiments $Re \approx 50 \ldots 150 \gg 1$, so the effects of viscosity will be negligible. We will discuss dissipation and vortical flow further in Sec. 5.3.

Both phenomena, dissipation and internal flow, are embodied in the scaling factor f_K. We apply f_K to the initial kinetic energy only, instead of writing $f_K(E_{K,0} - \Delta E_S)$. This is justified by assuming that the drop shape at lift-off, and hence ΔE_S, is a result of this reduction in energy already.

If $E_{K,\mathrm{det}} > 0$ the energy criterion is fulfilled and the drop can leave the surface, so that

$$f_K E_{K,0} > E_{S,\uparrow} - E_{S,0} \tag{5.12}$$

for pancake bouncing. To find an expression for $E_{S,\uparrow}$ assume that the time scale criterion Eqn. (5.10) is fulfilled, i.e. the drop, having emptied the post structure, is just at its maximum extension. This restriction is necessary as there is no analytical expression for $D(t)$ in the literature. Hence we have to restrict ourselves to the quantities for which we do have an analytical approximation, the shape when the spreading is maximal. For low and moderate Weber numbers (see Sec. 3.5.3), $E_{S,\uparrow}$ can be approximated by the surface of a disc of width D_{max} and height H_{min} as

$$\text{sim}: \quad E_{S,\uparrow} \approx \sigma(2D_{max} + 2H_{min}), \tag{5.13a}$$

$$\text{exp}: \quad E_{S,\uparrow} \approx \sigma(2\pi\frac{{D_{max}}^2}{4} + \pi D_{max}H_{min}). \tag{5.13b}$$

From [50] we know scaling laws for H_{min} and D_{max}, as described in Sec. 4.2.2, where we found an expression for the three-dimensional case in Eqn. (4.3) and Eqn. (4.4), respectively. In two dimensions volume conservation, $H_{min}D_{max} \sim D_0^2$, results in a

different scaling to three dimensions. We get

$$\text{sim}: \quad H_{min} = \xi_H \sqrt{\frac{\sigma 2R_0}{(\rho v_0^2)}} = \xi_H h_{cap}\,, \quad D_{max} = \xi_{D,2\text{d}} 2R_0 We^{1/2}, \tag{5.14a}$$

$$\text{exp}: \quad H_{min} = \xi_H \sqrt{\frac{\sigma 2R_0}{(\rho v_0^2)}} = \xi_H h_{cap}\,, \quad D_{max} = \xi_{D,3\text{d}} 2R_0 We^{1/4}. \tag{5.14b}$$

We should point out here that there is an inherent contradiction to our previous assumption in this approach. Clanet's scaling arguments leading to Eqn. (5.14b) used a 'crashing time' D_0/v_0 for the time the spreading process takes. Yet, in Eqn. (5.8) we claim that $t_{max} \sim \sqrt{\frac{\rho}{\sigma} R_0^3} = \tau_{ci}$. This point will be discussed in detail in Sec. 5.3.2, but, anticipating the discussion there, the results using τ_{ci} instead of D_0/v_0 will not be significantly different, so we will stay with Clanet's scaling from the literature [50] for now.

The initial kinetic and surface energy in two and three dimensions, for simulation and experimental results, respectively, are

$$\text{sim}: \quad E_{K,0} = \rho \frac{1}{2} \pi R_0^2 v_0^2\,, \quad E_{S,0} = 2\pi R_0 \sigma, \tag{5.15a}$$

$$\text{exp}: \quad E_{K,0} = \rho \frac{4}{6} \pi R_0^3 v_0^2\,, \quad E_{S,0} = 4\pi R_0^2 \sigma. \tag{5.15b}$$

Using Eqns. (5.13), Eqns. (5.14), and Eqns. (5.15), the energy condition Eqn. (5.11) becomes

$$\text{sim}: \quad f_{K,\text{sim}} \rho \frac{1}{2} \pi R_0^2 v_0^2 > \sigma \left(4R_0 \xi_{D,2\text{d}} We^{1/2} + 2\xi_H \sqrt{\frac{\sigma 2R_0}{(\rho v_0^2)}} - 2\pi R_0 \right), \tag{5.16a}$$

$$\text{exp}: \quad f_{K,\text{exp}} \rho \frac{2}{3} \pi R_0^3 v_0^2 > \sigma \left(2\pi \xi_{D,3\text{d}}^2 R_0^2 We^{1/4} + 2\pi R_0 \xi_{D,3\text{d}} \xi_H We^{1/2} \sqrt{\frac{\sigma 2R_0}{(\rho v_0^2)}} - 4\pi R_0^2 \right). \tag{5.16b}$$

Rearranging, and identifying $We = \rho R_0 v_0^2/\sigma$, yields

$$\text{sim}: \quad We > \frac{1}{f_{K,\text{sim}}}\left(\frac{8}{\pi}\xi_{D,2D}We^{1/2} + \frac{4\sqrt{2}}{\pi}\xi_{H,2D}We^{-1/2} - 4\right), \tag{5.17a}$$

$$\text{exp}: \quad We > \frac{1}{f_{K,\text{exp}}}\left(3\xi_{D,3D}^2 We^{1/2} + 3\sqrt{2}\xi_{D,3D}\xi_{H,3D}We^{-1/4} - 6\right) \tag{5.17b}$$

Solving Eqns. (5.17) as an equality gives the critical Weber number We_c above which the inequalities are fulfilled. The impact energy is high enough and the drop can jump whilst in a pancake shape.

5.2 Theory Results

With Eqns. (5.10) and Eqns. (5.17) we have derived analytical expressions for the time scale and energy criterion, respectively. However, in order to apply the expressions and propose a design diagram, we need to determine the scaling factors appearing in Eqns. (5.10) and Eqns. (5.17). To remind the reader, ξ_τ, ξ_H, and ξ_D are physical prefactors, and f_t and f_K are necessary to account for dissipation, effective masses, and vortical flow. In order to determine these scaling factors we plot the modeled quantities against the measured ones. This also serves as a test of the theoretical model: if the theory describes the physics well, the data points should show a linear behaviour.

In Fig. 5.2 and Fig. 5.3 we plot all the theoretical predictions for $t_\uparrow$ (Eqn. (5.6)), t_{max} (Eqn. (5.8)), H_{min}, D_{max} (Eqns. (5.14)) against their measured counterparts in the top four panels, for simulations and experiments, respectively. A linear fit 'measured = factor · theory' gives the scaling factors, which are summarised in Table 5.1. The respective fit results are given, including the estimated error with a confidence interval of twice the standard deviation (95.5% confidence).

	f_t	ξ_τ	ξ_H	ξ_D	f_K	We_c
sim.	3.99±0.10	1.36 ±0.03	1.08±0.05	1.14±0.07	0.77±0.03	1.37
exp.	1.36±0.05	0.82±0.05	1.00±0.08	1.02±0.03	–	2.32 $\xrightarrow{f_K=0.92}$ 3.00

Table 5.1: Fitted scaling factors for simulations and experiments

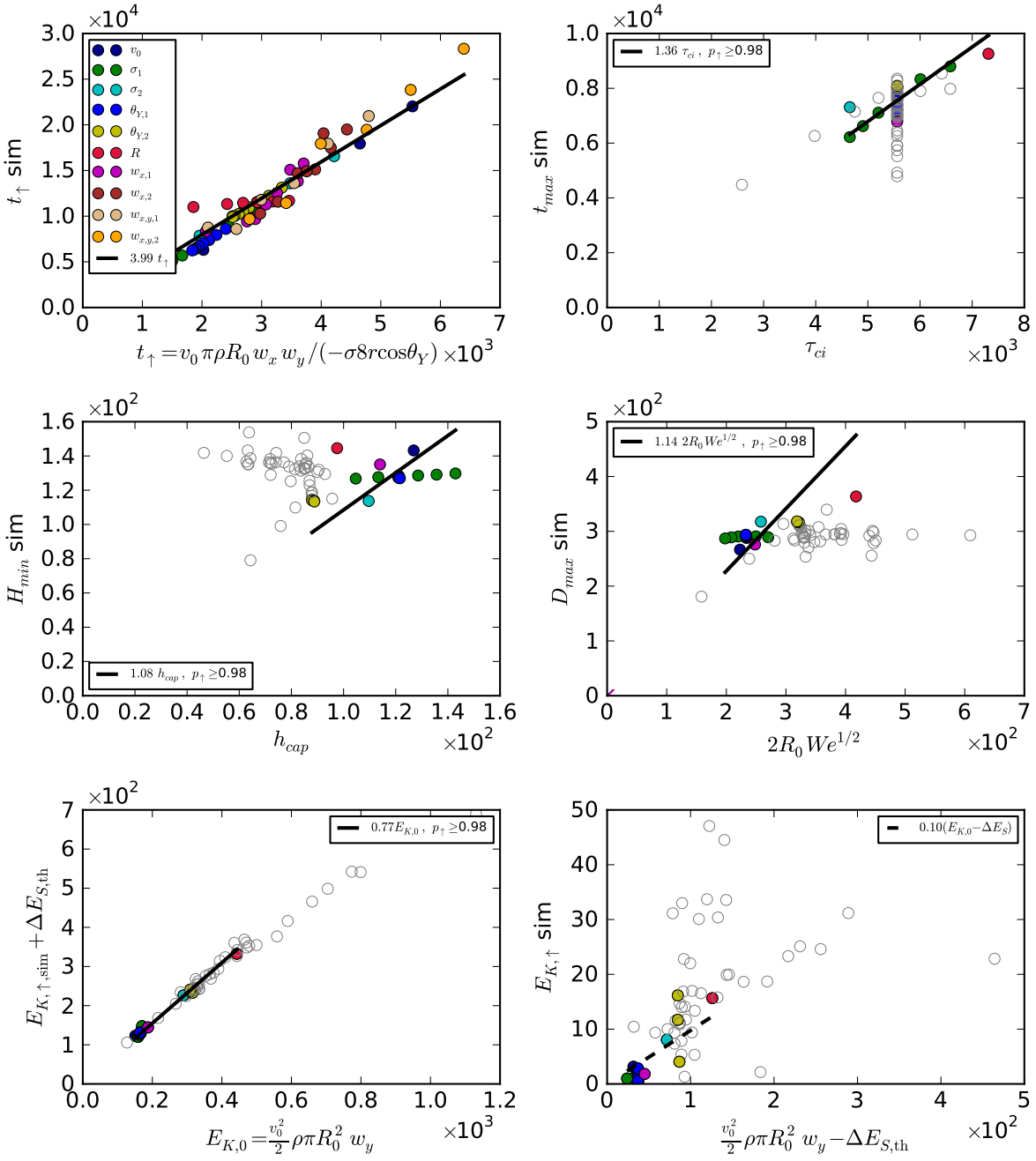


Figure 5.2: Fitting the scaling parameters for simulations (top left to bottom right) f_t, $\xi_{\tau,2\mathrm{d}}$, ξ_H, $\xi_{D,2\mathrm{d}}$, f_K, f_K, with $\Delta E_{S,\mathrm{th}} = \sigma\left(4R_0\xi_{D,2\mathrm{d}}We^{1/2} + 2\xi_H h_{cap} - 2\pi R_0\right)$. The last plot is given as proof that indeed Eqn. (5.12), bottom left panel, is the better ansatz for f_K. The simulation parameters for the different data sets indicated in the legend are given in Tab. 5.2.

For determining ξ_τ, ξ_H, and ξ_D, the scaling factors for t_{max}, H_{min}, and D_{max}, respectively, only those data points were used for fitting for which there is little penetration at $t = t_{max}$. To justify this approach, consider an example: Say there is considerable

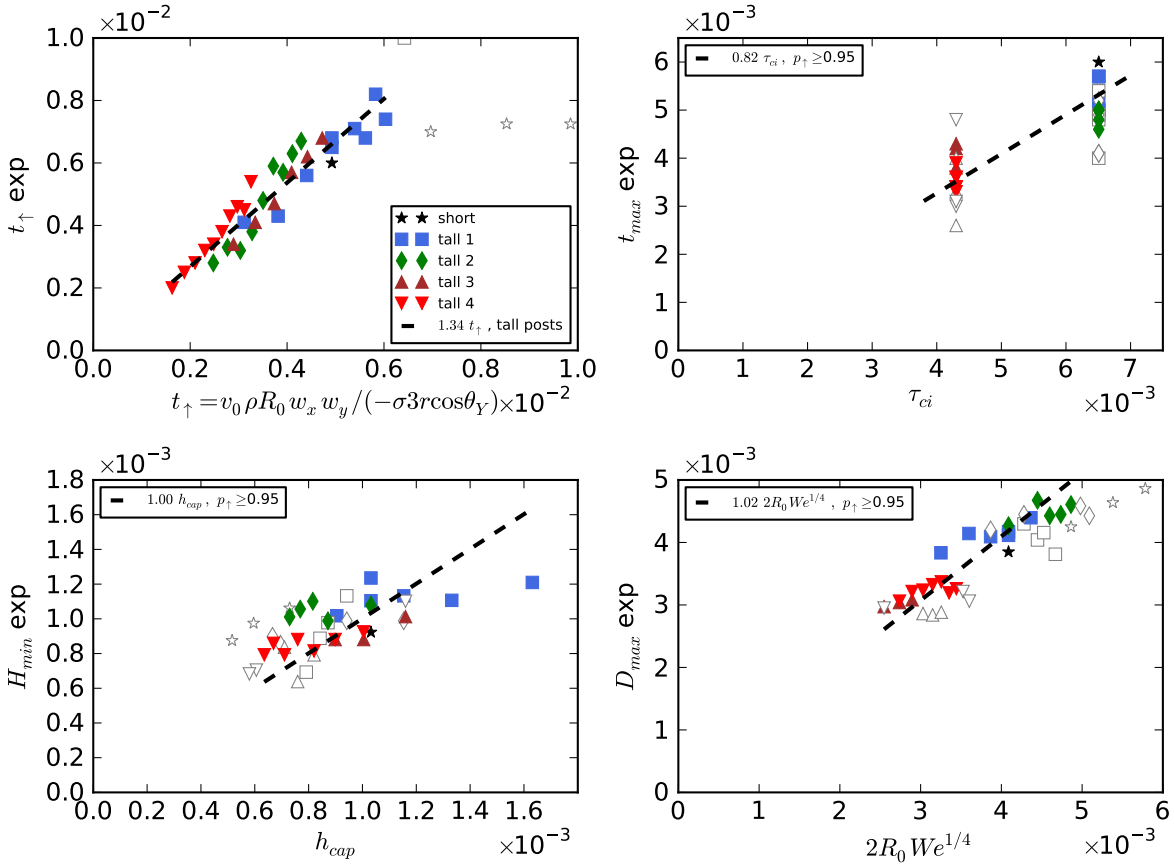


Figure 5.3: Fitting the scaling parameters for experiments (top left to bottom right) f_t, $\xi_{\tau,3d}$, ξ_H, $\xi_{D,3d}$. The parameters for the different data sets indicated in the legend are given in Tab. 5.3.

penetration at the time the droplet reaches t_{max}. The maximum spreading width D_{max} would be a result of the impact Weber number, but it would also reflect that there is less liquid available for spreading as some is imbibed under the surface. However, the portion of the liquid under the surface is not accounted for by the theory for D_{max} in Eqn. (4.4), and the effects would obscure the results of the expected scaling with We. Therefore, we use only data points that have a certain high $p_\uparrow = D_\uparrow/D_{max}$, which means that they are close to having fully recoiled when we measure the time for maximum spreading t_{max}, the height H_{min} at maximum spreading, and the maximum spreading diameter D_{max}. We used a threshold $p_\uparrow^* = 0.98$ in simulation and $p_\uparrow^* = 0.95$ in experiments as there are fewer data points. The remaining data points are included for reference, but plotted as empty grey symbols.

In the experiments we also include data for which the post height is smaller than the

maximum imbibition depth, i.e. the liquid hits the base. For these the time scale theory does not apply, as described in Sec. 5.1.1, hence they are not included in the fitting of f_t but given for reference, plotted in grey.

It is worth noting that our assumption of f_t being a constant for all simulations (Eqn. (5.7)) is indeed a good one: Both for simulations and experiments, shown in the top left panels of Fig. 5.2 and Fig. 5.3, respectively, the data points collapse onto a linear graph reasonably well.

The plots for ξ_τ show a reasonably good linear dependence as well, giving a scaling prefactor of $\xi_\tau = 0.82$ for the experiments. Our derivation suggested that we would

symbol	$v_0[\times 10^{-2}]$	R_0	$\sigma[\times 10^{-2}]$	θ_Y	r	w_x	w_y
● v_0	1.0 . . . 5.5	100	3.2	150°	8	24	24
● σ_1	≈ 2.0	100	2.3 . . . 4.6	150°	8	24	24
● σ_2	≈ 3.0	100	2.3 . . . 4.6	150°	8	24	24
● $\theta_{Y,1}$	≈ 2.0	100	3.2	140° . . . 175°	8	24	24
● $\theta_{Y,2}$	≈ 3.0	100	3.2	140° . . . 175°	8	24	24
● R	≈ 3.0	60 . . . 120	3.2	150°	8	24	24
● $w_{x,1}$	≈ 2.5	100	3.2	150°	8	18 . . . 30	24
● $w_{x,2}$	≈ 3.5	100	3.2	150°	8	18 . . . 30	24
● $w_{x,y,1}$	≈ 3.0	100	3.2	150°	8	18 . . . 30	18 . . . 30
● $w_{x,y,2}$	≈ 4.0	100	3.2	150°	8	18 . . . 30	18 . . . 30

Table 5.2: Simulation parameters used and corresponding symbol. Values are given in lattice units, approximate values are given for the measured impact velocities v_0, however the exact values were used for calculations.

symbol	R_0 [mm]	$w_{x,y}$ [mm]	r [mm]	θ_Y
★ short	1.45	0.4	0.1	160°
■ tall 1	1.45	0.4	0.1	160°
♦ tall 2	1.45	0.3	0.1	160°
▲ tall 3	1.10	0.4	0.1	160°
▼ tall 4	1.10	0.3	0.1	160°

Table 5.3: Parameters used in experiments and corresponding symbol. In each case, the impact velocity was varied.

expect a value $\xi_\tau \lessapprox \frac{1}{2}[2.3 \ldots 2.65]$ [53, 55, 56, 80]. The deviation from this expectation can be attributed to effects from transient imbibition and to the fact that the time for maximum spreading could be closer to the crashing time D_0/v_0 (see Sec. 5.3.2). The plot also suggests that there is a bias due to the substrate parameters: a wider spacing seems to give a higher t_{max}. Such a substrate dependence is not accounted for by our theory.

There appears to be no literature for comparison to the value $\xi_\tau = 1.36$, found for the 2D simulations. However, we do expect it to be larger than for the 3D case, as the spreading process as a whole is slower in 2D. Also, as discussed in Sec. 4.2.1 and in [127], a surrounding liquid of equal density, as is the case for our simulations, increases the oscillation period of a free drop by $(5/3)^{1/2} \approx 1.3$ which will also affect our simulation results. We found in our research on drop coalescence, see Ch. 3.4 that a liquid drop with the same fluid parameters oscillates with $T_{osc} \approx 4.1\tau_{ci}$. Given that the contact time of a drop bouncing on a surface should cover between a half and a full oscillation period (see Ch. 4.2.1), and we expect $t_{max} \approx \frac{1}{2}T_{contact}$, $t_{max} = 1.36\,\tau_{ci}$ is in good agreement with our own findings for drop oscillation.

The fits of D_{max} and H_{min} exhibit a less compelling linear behaviour, especially for the simulation results. This could be due to two things. Firstly the derivation of the scaling laws involved the crashing time D_0/v_0, which may not be the right scaling for a system with considerable imbibition. Using τ_{ci} as the relevant time scale instead of D_0/v_0 leads to a scaling of D_{max} with $We^{1/4}$ in 2D and $We^{1/8}$ in 3D. This will be discussed and the results compared to the ones resulting from using the crashing time in Sec. 5.3.2.

Secondly, we assumed a disc-like shape to approximate the volume of the drop. This is a very rough approximation, especially for low *We*, as the shape is closer to an ellipsoid when the spreading distortions are small. Moreover, for the experimental data at higher *We*, the drop started to show a visible rim, thus deviating from the disc shape. This also resulted in distortions of the drop's top surface, which made measuring H_{min} ambiguous.

For the simulations we can also find the scaling parameter for the energy criterion, f_K, by plotting $(E_{K,\uparrow} + \Delta E_S)$ against $E_{K,0}$ (Eqn. (5.11)), where ΔE_S is found from the scaling factors ξ_H and ξ_D by using Eqn. (5.16a). Technically, $E_{K,jump}$ of a *detached* drop would

have to be measured here instead of $E_K(t = t_\uparrow)$, which means the drop has recoiled, but not detached. However, this is difficult for simulations as the detachment process takes time and, for $We < We_c$ involves retraction already, so does not serve as the quantity appropriate for finding We_c. We have verified that the adhesion work that has to be overcome for bouncing, $n\sigma(\cos\theta_Y + 1) \ll E_K(t = t_\uparrow)$, therefore using $E_K(t = t_\uparrow)$ instead of $E_{K,jump}$ is reasonable.

In the bottom two panels of Fig. 5.2 we plot $(E_{K,\uparrow} + \Delta E_S)$ against $E_{K,0}$ on the left, corresponding to the suggested application of f_K to $E_{K,0}$ only. As a comparison we plot $E_{K,\uparrow}$ against $(E_{K,0} - \Delta E_S)$ on the right hand side, which implies applying f_K to $(E_{K,0} - \Delta E_S)$. Clearly, this does not show a linear dependency, whereas the left hand side does, supporting Eqn. (5.11). From f_K, ξ_H, and ξ_D we can also find the critical Weber number We_c by numerically solving Eqn. (5.17a). This is also given in Table 5.1. The theory yields $We_c = 1.4$, in agreement with the measured results (see Fig. 4.12).

In the experiments we cannot measure the kinetic energy of the motion of the droplet's centre of mass, so finding f_K from fitting is not possible. For the case of no dissipation and no internal velocities where $f_K = 1$ we would find $We_c = 2.3$. However, assuming a reasonable value of $f_K = 0.92$ yields $We_c = 3.0$, which is what is observed in the experiments (see Fig. 4.12).

Please note that the simulation results presented here are those of all parameter variations listed in Sec. 4.3.2, with the exception of those for varying the post width. Large effects from the initial conditions had the result that the impact velocity could not be measured well, due to persistent oscillations in the velocity field. These appeared in other simulations as well, visible in the slight undulations in the $l(t)$ plots in Fig. 4.11, for example. However, in the dataset for varying r these were much more pronounced, due to the high initial velocity necessary to overcome the increased dissipation, when the post width increases.

To summarize the results of this section, we have demonstrated by showing linear dependencies between the theoretical prediction and the measured results that our theoretical model describes the physical observation from experiments and simulations

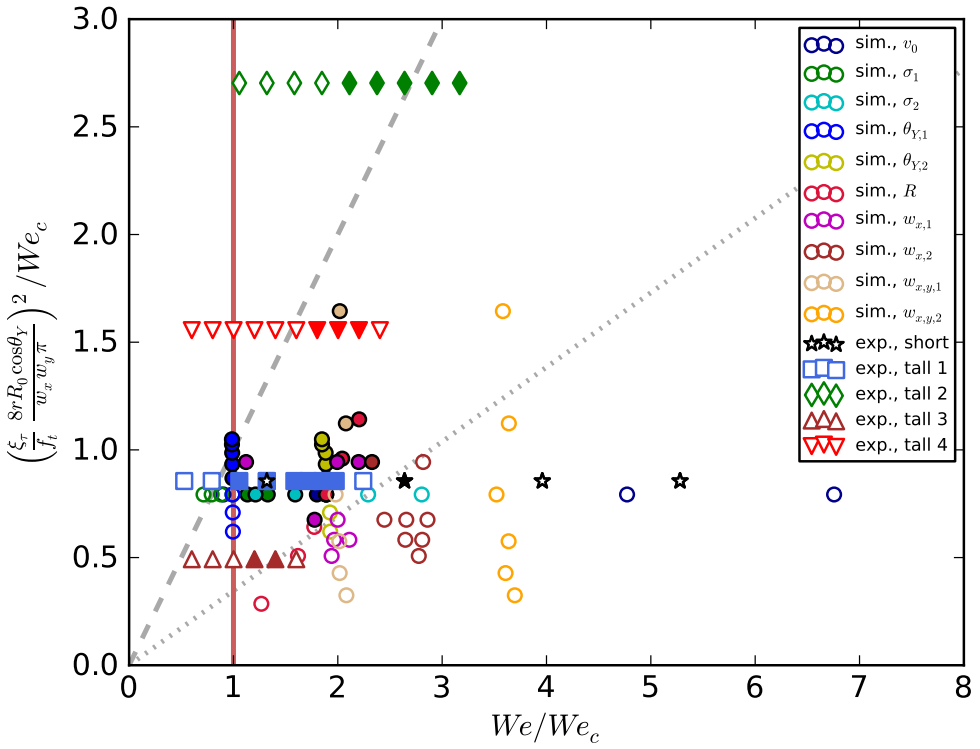


Figure 5.4: Design diagram for pancake bouncing. Full symbols denote a successful pancake bounce ($p > p^*$), empty symbols denote a conventional rebound. For $We/We_c > 1$ (red solid line) the energy criterion is met. To the left of the grey dashed line ($k = 1$), pancake bouncing bouncing can not happen due to downward flow ($k < 1$). The time scale criterion is met in the region between the grey dashed and the grey dotted line $1 < k < k^*$. The parameters for the different data sets indicated in the legend are given in and Tab. 5.2 and Tab. 5.3, respectively.

well within the necessary assumptions and approximations. We have determined the physical prefactors ξ_τ, ξ_H, and ξ_D and accounted for the influence of dissipation, effective masses, and vortical flow by finding f_t and f_K. Using our model, we can now explain the phenomena observed in the experiments, such as the different onset Weber numbers for the pancake phenomenon on different surfaces, and we can explain the dependence of the pancake phenomenon on drop and substrate parameters. This is the aim of the following section.

5.2.1 Design Diagram

If both the time scale and the energy criteria, Eqns. (5.10) and (5.17), are met, the drop firstly has reached its widest extent just when the liquid has emptied the structure, and

secondly has enough energy to bound off the surface at the same time. Both equations give a condition on the Weber number: the energy criterion Eqns. (5.17) states that $We > We_c$ is necessary, where We_c is a constant for all data sets, whereas Eqns. (5.10) gives a lower boundary

$$\text{sim}: \quad We_{min} = \left(\frac{\xi_{\tau,\text{2d}}}{f_t} \frac{8r \cos\theta_Y R_0}{\pi w_x w_y} \right)^2, \tag{5.18a}$$

$$\text{exp}: \quad We_{min} = \left(\frac{\xi_{\tau,\text{3d}}}{f_t} \frac{3r \cos\theta_Y R_0}{w_x w_y} \right)^2, \tag{5.18b}$$

that depends on the substrate parameters and R_0. It represents the Weber number corresponding to the theoretical prediction for $k = 1$. Eqns. (5.10) also state that We should not be too high, as the pancake quality decreases gradually when $We > We_{min}$, i.e. $k > 1$. Rearranging Eqns. (5.9) in the form $y = f(We/We_c)$, that is

$$\text{sim}: \quad y = \left(\frac{\xi_{\tau,\text{2d}}}{f_t} \frac{8r \cos\theta_Y R_0}{\pi w_x w_y} \right)^2 \frac{1}{We_c} = \frac{1}{k^2} \frac{We}{We_c}, \tag{5.19a}$$

$$\text{exp}: \quad y = \left(\frac{\xi_{\tau,\text{3d}}}{f_t} \frac{3r \cos\theta_Y R_0}{w_x w_y} \right)^2 \frac{1}{We_c} = \frac{1}{k^2} \frac{We}{We_c}, \tag{5.19b}$$

we can plot a design diagram for pancake bouncing, shown in Fig. 5.4. We plot the Weber number on the x-axis, scaled by the critical Weber number We_c determined from the energy criterion Eqn. (5.17). The y-axis contains the structural parameters which determine k according to Eqns. (5.19). Only the equation for simulations, Eqn. (5.19a), is given on the diagram, however, for the experimental data Eqn. (5.19b) was applied.

Filled symbols denote a succesful pancake bounce, with $p^* > 0.8$ for the experimental data and $p^* > 0.9$ for the simulation data. Empty symbols denote that the respective threshold on p has not been reached and the bounce is considered a conventional rebound. The lines indicate the same quantities as in Fig. 4.12: The solid red line represents the energy criterion $We = We_c$. The dashed grey line represents $We = We_{min}$ from Eqns. (5.18), the lower boundary on We for the time scale criterion. The dotted grey line indicates the upper boundary on We, corresponding to $k = k^* = 1.7$, which can be read

off Fig. 4.12 for the chosen cutoff values p^*. Pancake bouncing is only possible in the region bounded by these three lines.

The data matches convincingly with the predicted boundaries for pancake bouncing, confirming that our theory describes the phenomenon well. The slight mismatch in the green data points of the experiments is because the predicted time scale is not very exact for the experimental data. This is a result of t_{max} differing for different post spacings, which is not included in our model, as discussed in Sec. 5.2.

One might argue that the data points matching so nicely with the boundaries in Fig. 5.4 is not surprising given that we have applied scaling factors to achieve exactly that. However, we had to use scaling factors because they are either inherently physical (ξ_τ, ξ_D, ξ_H), or have to account for inherent limitations of the simulation algorithm used, i.e. large dissipation and inertia (f_t, f_K). Our aim was to uncover what parameters lead to pancake bouncing; applying these scaling factors allowed us to prove that the dependence on the relevant fluid and substrate parameters we derived are correct.

Guided by the design diagram Fig. 5.4, we will discuss in the following paragraphs how our initial experimental observations listed in Sec. 4.1.3 fit in with the theoretical model developed in this chapter, and how the design of a surface affects pancake bouncing.

Contact time and pancake bouncing We observed in Sec. 4.1.3, point 1, that in bouncing experiments on the MTS substrate and on pillar surfaces, at $We = We^*$ the contact time $T_{contact}$ for the impact event abruptly decreased. A low contact time corresponds to a high pancake quality p, as the drop leaves the surface when it is extended most, without spending time retracting. This explains why at the threshold We^* the contact time decreases so abruptly, it is simply the boundary at which pancake bouncing sets in. Below We^*, the contact time is that of conventional bouncing, which for a given liquid only depends on the drop radius R_0 according to Eqn. (4.2) and the discussion thereafter in Sec. 4.2.1. This complies with our observation in Sec. 4.1.3, point 3: The contact time for $We < We^*$ was $\approx 16\,\text{ms}$ (11 ms) for a drop of $R_0 = 1.45\,\text{mm}$ (1.10 mm), the theory and literature predict $T_{contact} = 2.3 \ldots 2.65\sqrt{\rho R_0^3/\sigma} =$

15.0 . . . 17.2 ms (9.9 . . . 11.4 ms). For $We > We^*$, as observed in Sec. 4.1.3, point 4, the contact time becomes dependent on the drop and substrate parameters. This corresponds to the theoretical model, too, because the time for the liquid to empty the structure $t_\uparrow$, upon which that pancake bounce may happen, depends on the substrate parameters according to Eqn. (5.6b).

Transient phenomenon In Sec. 4.1.3, point 5, it was stated that for Weber numbers higher than We^* the contact time $T_{contact}$ gradually increased again from the lowest value at $We \gtrapprox We^*$, and that the degree of this increase depended on the parameters of the experiment. This means that the pancake effect breaks down if the impact Weber number is too high, and that the range of Weber numbers showing pancake behaviour is different for different surfaces.

Using Fig. 5.4, we can now explain this behaviour. p gradually decreases for increasing $k > 1$, as we discussed in relation to Fig. 4.12, because too much liquid penetrates the substrate and therefore the liquid takes too long to return to the surface. By the time it does, the drop has started retracting and shows less of a pancake character when leaving the substrate. We defined that for a bouncing event to be considered a successful pancake bounce, a pancake quality of $p \geq 0.8$ ($p \geq 0.9$ in simulations) must be achieved. This region of high pancake quality, and therefore low $T_{contact}$, is bounded by $k = 1$ and k^*, the dashed and dotted lines in Fig. 5.4.

k depends on the Weber number as well as the substrate and drop parameters according to Eqn. (5.9b). For given substrate and drop parameters, which affect the y-coordinate on the diagram, this leads to a certain range for We where the pancake quality is high, for $x = We/We_c$ values between the dashed and dotted lines in Fig. 5.4. The width of this region of effective pancake bouncing strongly depends the y-coordinate, and thus on R_0 and the substrate, therefore the range for short contact times must change when varying R_0 and the substrate parameters.

Necessary substrate parameters The phase diagram Fig. 5.4 gives an idea of the design parameters necessary for a surface to show pancake bouncing. The phenomenon appears when the impact energy is high enough for a given liquid, i.e. $We > We_c$. Once this criterion is achieved, pancake bouncing depends strongly on the surface parameters. As the diagram shows, a higher y-coordinate on the diagram will result in a wider We region that allows pancakes. According to Eqns. (5.19), decreasing the post spacing $w_{x,y}$ has this effect, or increasing the post width r, the intrinsic contact angle θ_Y, or the drop size R_0. In turn, if $w_{x,y}$ is becomes too large, or r, R_0, or θ_Y too small, the pancake effect will vanish: matching time scales will only be possible for Weber numbers $We < We_c$ that are too small to give sufficient energy for jumping whilst in the pancake shape.

Substrate-dependent onset Fig. 5.4 also reveals the explanation why the onset of pancake bouncing depends so strongly on the substrate, as discussed in Sec. 4.1.3, point 2, especially the very high-We onset for the MTS substrate. The diagram shows that the minimum Weber number above which we see pancakes, We^* – recall that this is different from We_c, which was the cutoff only for the energy criterion – changes with the substrate: For higher y-coordinates on the diagram (say, for smaller $w_{x,y}$, green and red squares), We^* changes from We_c (red solid line) to the $k = 1$ line (dashed). The energy criterion may be met, but if $k < 1$ there is still no pancake bouncing because the fluid returns to the surface whilst there is still downward flow from the spreading.

This also explains why we observed a *lowest* $We^* = 3$ in Sec. 4.1.3, point 2. This simply corresponds to the energy criterion $We > We_c \approx 3$, below which no pancake bouncing can be seen, irrespective of the substrate parameters.

Moreover, the phase diagram explains why for certain surfaces the jumping pancakes are more impressive, in the sense that they are more disc-like. Not only does a higher y-coordinate allow a wider We region that shows pancake jumping, the region is also further to the right, i.e. *at* higher Weber numbers. Since We affects the maximum drop spreading according to Eqns. (5.14), this will result in the drops being wider while jumping without retracting.

Understanding MTS Pancake bouncing was first reported on the MTS substrate described in Sec. 4.1.1, but its complicated structure prevented an understanding of the effect. Instead, following our suggestion the experimentalists kindly looked at pillar surfaces, which are much simpler, to study the governing ideas of pancake bouncing. Yet, comparing both, they found that the MTS substrate shows a much higher onset of pancakes, at $We^* = 14$ rather than $\approx 3 \ldots 6$ for pillar surfaces, and the pancaking drops look much more impressive, as can be seen from comparing Fig. 4.1 and Fig. 4.4.

The discussion of the substrate dependence of We^* in the previous paragraph also explains consistently why for the MTS substrate the onset of pancake bouncing is at so much higher a Weber number than for the simple pillar surface. There may be a bit more dissipation due to the small pores, which would increase We_c, but this could not account for such a high necessary We^* as the influence of viscous dissipation is generally quite small in the experiments due to the high Reynolds number associated with the imbibition process of $Re = 50 \ldots 150 \gg 1$.

The effect that causes $We^* = 14$ must be the $k = 1$ boundary: Due to the small pore size the fluid returns too early at low $We < 14$, giving $k < 1$ for a large range of Weber numbers before permitting pancakes. Therefore, We has to be much higher than for a pillar structure to give enough liquid imbibition for pancake lifting to be possible.

Using high impact velocities then also results in impressive pancakes of $D_{jump} \gg R_0$, and in the pancake region being wide. From our theory we would expect $14 < We < 41$ for pancakes, an experimental upper boundary was observed at $We \approx 33$.

In turn, this discussion also allows us to understand how to model the MTS substrate better – its porous nature can be taken into account if we treat the pores as effective posts with a spacing w_{eff}. w_{eff} can be estimated from Eqn. (5.18b): For $We_{min} = 14$ and $r \approx 0.08\,\text{mm}$ this yields an effective pillar spacing of $w_{\text{eff}} \approx 0.20\,\text{mm}$. The pore diameter for the MTS is about 0.40 mm, so 0.20 mm is indeed a reasonable number.

Short posts Our theoretical framework for the time scales did not include cases for which the liquid touches the base of the substrate. It is only suited for sufficiently tall

posts. The energy criterion, however, is valid irrespective of the post height.

Experiments suggest that it is much easier to achieve pancake bouncing on short posts – a wider range of Weber numbers shows the effect, as could be seen in Fig. 4.5 and was noted in Sec. 4.1.3, point 5.

This is likely to be because if the drop hits the base substrate under the short posts, the time over which the fluid returns to the surface is decreased. Note, this is only true for a surface with two-tier roughness showing a very high intrinsic contact angle like 160° in our experimental case. For single-tier superhydrophobic surfaces this would result in the (sticky) Wenzel state, and the drop would have considerable difficulty rebounding, as discussed for experimental examples in Sec. 4.2.3.1.

The post height seems to even set an upper boundary on the recoil time $t_\uparrow$ (see grey symbols in Fig. 5.3, top left panel), thus allowing higher impact velocities to be used without the penalty of having too much penetration and therefore late recoil. This explains why for a substrate with short posts we tend to see wider pancakes corresponding to higher *We* than on substrates with longer posts. On the other hand, for low *We*, very short posts will limit the post recoil time such that the liquid will return too early to allow pancake bouncing. Therefore, the post height will strongly affect the onset Weber number, We^*.

5.3 Discussion of Assumptions Used

In this section, we will discuss the various assumptions made in the derivation of the energy and time scale criteria. We neglected the Laplace pressure in finding an expression for $t_\uparrow$ and we introduced effective masses via $f_\downarrow$ and $f_\uparrow$ to account for dissipation and inertia in the derivation of Eqns. (5.10). Moreover, we stated that viscous dissipation is strong for the flow between the posts, and introduced a factor f_K to take this, and vortical flow, into account in the framework of the energy criterion. Additionally, to find an expression for $D_{max}(We)$, we argued that both the crashing time D_0/v_0 and τ_{ci} are possible time scales for the impact, but used the crashing time as done in the

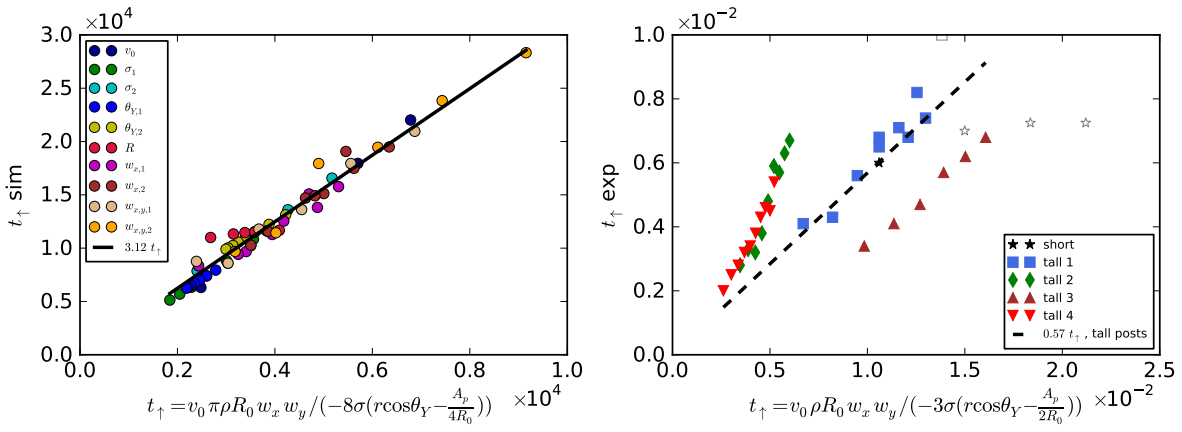


Figure 5.5: Linear fit for the recoil time $t_\uparrow$ with included Laplace force, following Eqns. (5.20), for simulations (left) and experiments (right), respectively. The parameters for the different data sets indicated in the legend are given in and Tab. 5.2 and Tab. 5.3, respectively.

literature [50]. Here, we will provide further evidence that these assumptions were indeed reasonable.

5.3.1 Laplace Pressure

Instead of using the capillary force Eqn. (5.1) as the only relevant force in the derivation of $t_\uparrow$ (Eqns. (5.6)), we discussed in Sec. 5.1.1 whether a Laplace force $F_L = -\frac{\zeta\sigma A_p}{R_0}n$ should be included. We omitted F_L arguing that the actual contribution of the Laplace force would be overestimated by this formula, as the drop shape changes during the bouncing process and the local curvature would even be zero temporarily. Here we present results with the Laplace force included, as a comparison to the simplified model derived

	f_t w/ F_L	rel. error	f_t w/o F_L	rel. error
simulations, 2D	3.12±0.05	1.6%	3.99±0.10	2.4%
experiments, 3D	0.58±0.10	12%	1.36±0.05	3.5%

Table 5.4: Fitted scaling factors f_t for $t_\uparrow$ in simulations and experiments Including the Laplace pressure. The error is given as two standard deviations (95.5% confidence).

in Sec. 5.1.1. Inclusion of F_L leads to Eqns. (5.6) taking the form

$$\text{sim}: \quad t_\uparrow \approx -\frac{v_0 \rho R_0 w_x w_y \pi}{8\sigma \left(r\cos\theta_Y + \frac{A_p}{4R_0} \right)} f_t, \tag{5.20a}$$

$$\text{exp}: \quad t_\uparrow \approx -\frac{v_0 \rho R_0 w_x w_y}{3\sigma \left(r\cos\theta_Y + \frac{A_p}{2R_0} \right)} f_t, \tag{5.20b}$$

where $A_p = w_x w_y - r^2$. Fits of these estimates against their measured counterparts are shown in Fig. 5.5. The results for the fitting factors are given in Table 5.4 and compared to the values found for $t_\uparrow$ without inclusion of F_L. The most noticeable difference is that for the experiments, the right panel of Fig. 5.5, the data clearly does not collapse onto one curve, which results in a large relative error of 12% compared to 3.5% without F_L. For the fit of the simulation data, comparing the left panel of Fig. 5.5 to Fig. 5.2, top left panel, the linearity is visibly better, which is reflected by the smaller relative error of 1.6% instead of 2.4% without F_L.

The difference between the experimental and simulation results is probably that in experiments $F_L = -\frac{\zeta \sigma A_p}{R_0} n$ is larger relative to F_c than in simulations, so a possible overestimation of F_L has a greater consequence. In experiments $F_c \approx 1.4 \ldots 3.5 F_L$ and in simulations $F_c \approx 3.3 \ldots 6.6 F_L$. Moreover, in our simulations effects from gas inertia and dissipation, which will be discussed in Sec. 5.3.4, are so pronounced that a possible overestimation of f_L does not affect the results as strongly as it would in experiments.

Therefore we can conclude that using the capillary force F_c, but neglecting the Laplace force F_L, is a good assumption in our framework. The capillary force is the dominant contribution, and the contribution from the Laplace force is probably overestimated by the simple expression $F_L = -\frac{\zeta \sigma A_p}{R_0} n$. However, an exact formula would have to include details of the interaction of the out-of-the-posts flow with the lateral spreading motion above the posts and details of the drop shape, which is not feasible in our simple kinematic model.

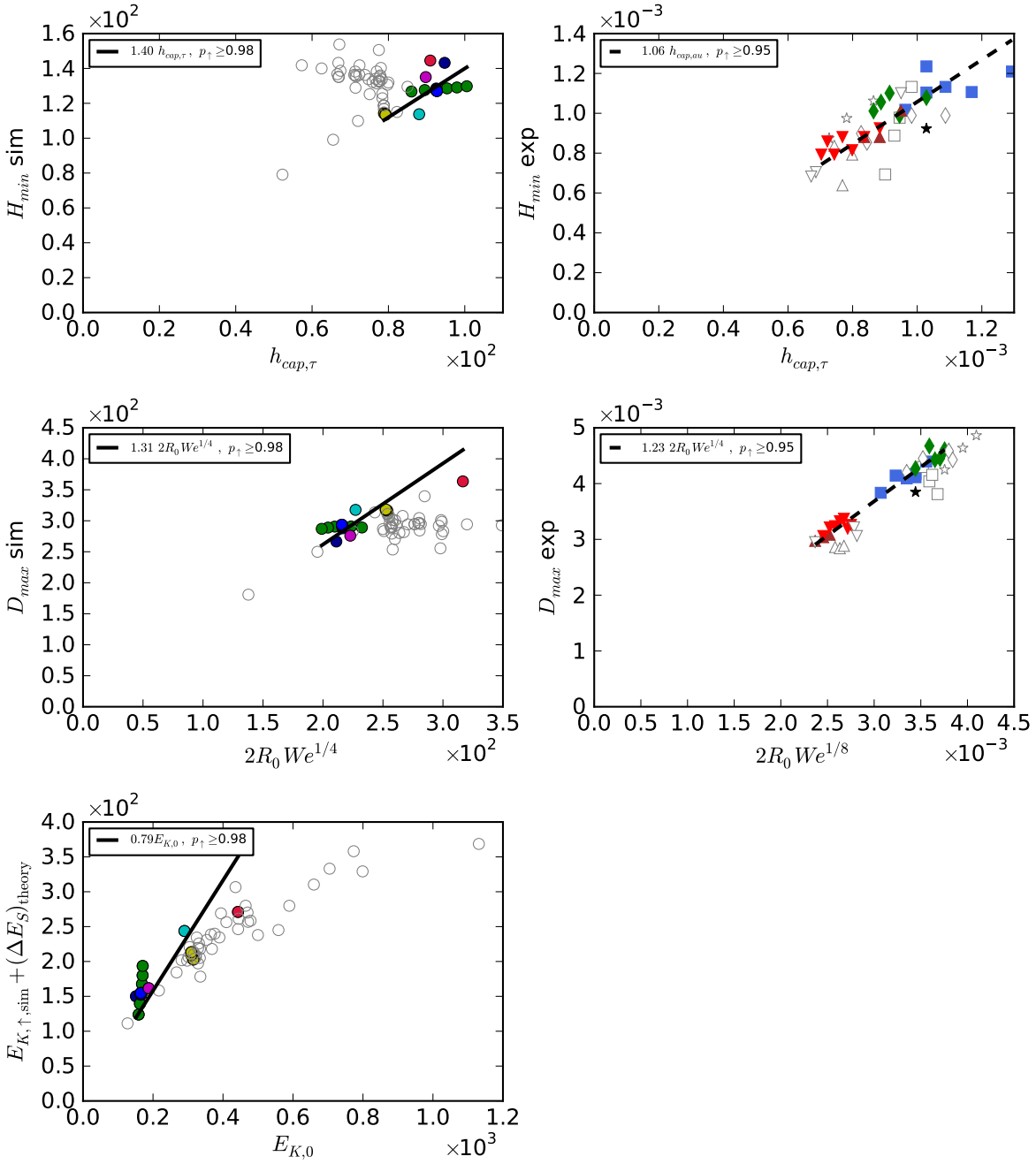


Figure 5.6: Linear fits for $\xi_{H,\tau}$, $\xi_{D,\tau}$, and f_K (top to bottom) for simulations (left) and experiments (right) if the crashing time scale D_0/v_0 is used to approximate droplet spreading. The simulation parameters for the different data sets indicated in the legend are given in and Tab. 5.2.

5.3.2 Crashing Time Scale vs Oscillation Time Scale

In Sec. 5.1.2, the crashing time D_0/v_0 was used as the spreading time scale in the derivation for H_{min} and D_{max} (Eqn. (4.3) and Eqn. (4.4), respectively). This was done in the literature for finding $D_{max}(We)$ [50], and D_0/v_0 is widely used for impact-driven

spreading processes [54]. We argued, however, that it would also be logical to use $\tau_{ci} = \sqrt{\rho R_0^3/\sigma}$. In fact, we assume that $t_{max} \sim \tau_{ci}$ in Eqn. (5.8), as it should be roughly half the bouncing time, which is usually approximated as $\sim \tau_{ci}$ [50, 53, 55, 80, 127].

The difference for our problem is that due to penetration into the substrate the droplet motion has more of the characteristics of an oscillation than on a flat surface – and indeed we observe that t_{max} is approximately constant with v_0, rather than showing a $1/v_0$ behaviour. The correct result for t_{max} probably lies somewhere between D_0/v_0 and $\frac{1}{2}2.6\sqrt{\frac{\rho}{\sigma}R_0^3}$ (see Sec. 4.2.1). Using a time scale of $\tau_{ci} = \sqrt{\rho R_0^3/\sigma}$ instead of Clanet's D_0/v_0 for t_{max} [50] leads to different expressions for H_{min} and D_{max}. The effective capillary length changes from Eqn. (4.3) to

$$h_{cap,\tau} = \left(\frac{\sigma R_0}{\rho}\right)^{1/4} \left(\frac{R_0}{v_0}\right)^{1/2}. \tag{5.21}$$

Volume conservation for an approximate disc shape, $H_{min}D_{max} \sim D_0^2$ in 2D and $H_{min}D_{max}^2 \sim D_0^3$ in 3D, yields

$$\text{sim}: \quad D_{max,\tau} \sim D_0 We^{1/4}, \tag{5.22a}$$

$$\text{exp}: \quad D_{max,\tau} \sim D_0 We^{1/8}, \tag{5.22b}$$

as opposed to $\sim We^{1/2}$ and $\sim We^{1/4}$, respectively. This results in the energy criterion Eqns. (5.17) reading

$$\text{sim}: \quad We > \frac{1}{f_{K,\text{sim},\tau}} \left(\frac{8}{\pi}\xi_{D,2D,\tau} We^{1/4} + \frac{4}{\pi}\xi_{H,2D,\tau} We^{-1/4} - 4\right), \tag{5.23a}$$

$$\text{exp}: \quad We > \frac{1}{f_{K,\text{exp},\tau}} \left(3\xi_{D,3D,\tau}^2 We^{1/4} + 3\xi_{D,3D,\tau}\xi_{H,3D,\tau} We^{-1/8} - 6\right). \tag{5.23b}$$

The linear fits determining the scaling factors $\xi_{H,\tau}$ and $\xi_{D,\tau}$ for simulations and experiments, and f_K are shown in Fig. 5.6, with simulations on the left and experimental results on the right. The results are shown in Table 5.5 – for comparison, the relative errors of the previous fits, where the crashing time was used, are also given. From these scaling

factors, the critical Weber number for the energy criterion is determined as $We_c = 1.75$ in simulations and $We_c = 3.52$ in experiments. The respective values for the scaling laws resulting from using the crashing time were 1.37 and 2.32, the values observed directly were ≈ 1.4 and ≈ 3, respectively.

Therefore, both methods, assuming spreading happens in a crashing time scaling as D_0/v_0 or assuming that spreading takes $t_{max} \sim \tau_{ci}$ result in values for We_c close to the observed ones, for both experiments and simulations. Comparing the quality of the fits for H_{min} and D_{max}, our scaling with τ_{ci} seems to be the better choice for both simulations and experiments. For the simulation results, We_c is not found to be as correct as with Clanet's scaling. This is due to the big error in f_K. Solving Eqn. (5.23a) with the lower and upper boundary for f_K gives $We_c = 1.52 \ldots 2.03$, so it comes close to the observed We_c, which is in itself only an approximate result that we read off the graph in Fig. 4.12.

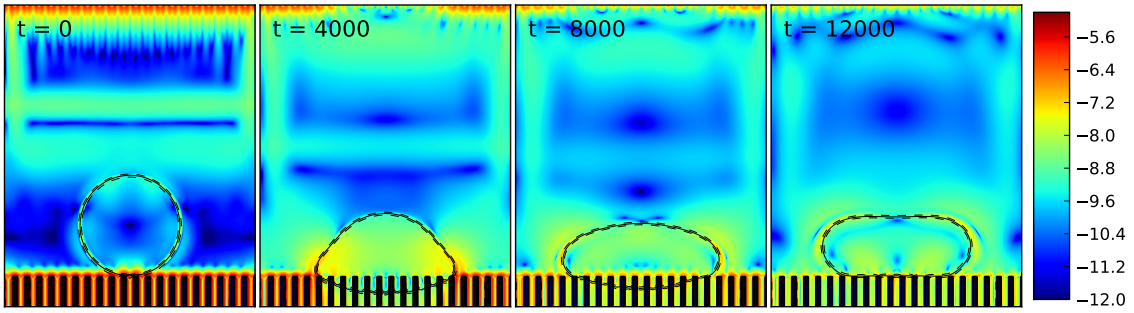
To conclude, either method gives reasonable results, but using τ_{ci} is consistent with our model for the time scale criterion, and the model fits the observed results better. The discussion in this section gives further evidence that $t_{max} \sim \tau_{ci}$ is indeed the correct scaling for the time for maximum spreading for impacts with considerable substrate penetration, as opposed to D_0/v_0 as used in the literature so far. It would be interesting in the future to run further simulations to investigate the applicability of the two time scales in more detail.

5.3.3 Dissipation Between Posts

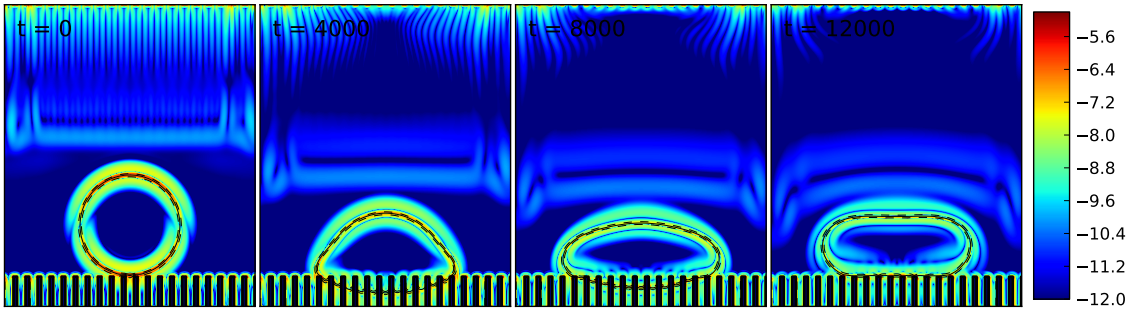
We argued in Sec. 5.1.1 and Sec. 5.1.2 that dissipation is not negligible in the simulations that were performed, and that it is especially relevant when the liquid enters the posts.

	$\xi_{H,\tau}$	rel. err [%]	$\xi_{D,\tau}$	rel. err [%]	$f_{K,\tau}$	rel. err [%]
sim.	1.40±0.03	2.3 (4.9)	1.31±0.03	2.6 (6.1)	0.79 (0.77)	8.6 (1.6)
exp.	1.06±0.04	3.7 (7.9)	1.23±0.02	1.5 (3.0)	–	–

Table 5.5: Fitted scaling factors $\xi_{H,\tau}$, $\xi_{D,\tau}$, and $f_{K,\tau}$ in simulations and experiments as a result of using τ_{ci} for the time scale of maximal spreading. The error is given as two standard deviations (95.5% confidence), the errors from using D_0/v_0 [50] (see Sec. 5.2) are given in brackets.



(a)



(b)

Figure 5.7: Time sequences of the local dissipation rate in logarithmic scale at $We = 3.15$. (a) Viscous dissipation from shear stress, (b) diffusive dissipation. The bar-like area of higher dissipation in the first plots of the sequences is an artefact of the initial conditions (same initial velocity for all liquid and gas nodes), travelling at the speed of the two phases until disturbed by the physical flow. Note that the dissipation between the posts is initially strong end decreases over time, and that the magnitude is generally much less for dissipation from diffusion.

We used this assumption to justify the introduction of scaling factors. Here we verify that dissipation between the posts is indeed much larger than elsewhere in the system.

From Eqn. (2.25) we can estimate the dissipation rate per unit volume $\dot{e} = \frac{\mathrm{de}}{\mathrm{dt}}$, where e denotes the energy density. For the drop oscillation motion above the posts, it scales as $\dot{e} \sim \eta(v_0/R_0)^2$ (see Eqn. (2.25)). Between the posts it is $\dot{e} \sim \eta 8(v_0/(w-a))^2$, which should exceed the dissipation from the oscillation flow by about one to two orders of magnitude as typically $(w-a)/R_0 \approx 6$.

Fig. 5.7a shows the local rate of energy dissipation from shear flow $\frac{\mathrm{d}}{\mathrm{dt}}e_{d,\eta}$, and Fig. 5.7b the equivalent for diffusive dissipation $\frac{\mathrm{d}}{\mathrm{dt}}e_{d,M}$. Fig. 5.7a confirms that between the posts

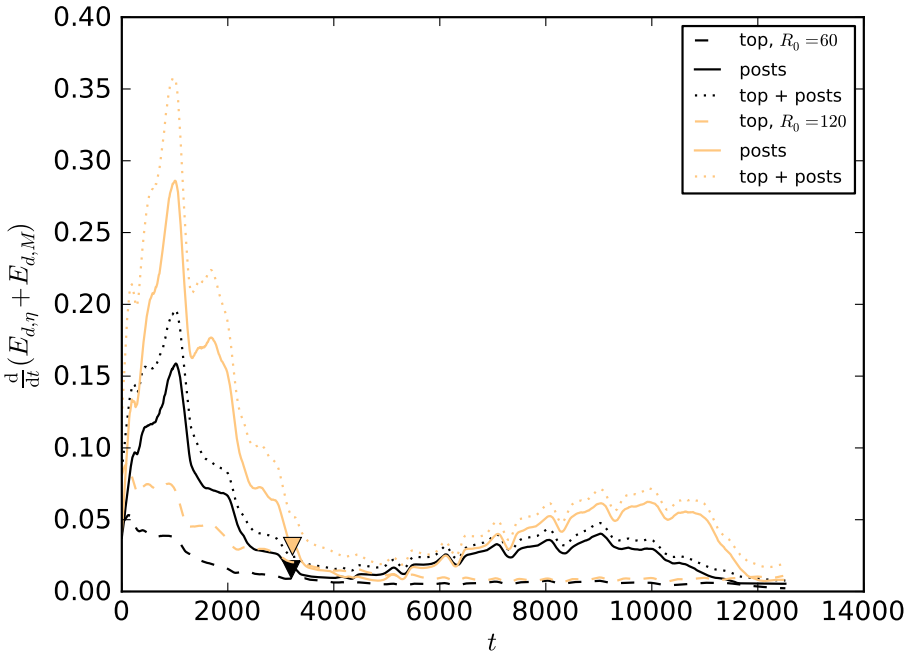


Figure 5.8: Total dissipation rate $\frac{\mathrm{d}}{\mathrm{d}t}(E_{d,M}+E_{d,\eta})$ with time for the liquid phase, with separate contributions for the liquid between the posts and above the surface.

the viscous dissipation is indeed much higher, especially early in the process when the gas squeezes through the posts at a high velocity v_0. Over time, as the gas phase's velocity in $-z$ direction decreases, the effect becomes weaker. The figures also show that the contribution from diffusion is typically two orders of magnitude smaller than that from viscous shear, which allows us to restrict ourselves to discussion of the shear contribution.

Taking into account the volume where this dissipation takes place, we can find an estimate of the total amount of rate of energy dissipation, $\mathrm{d}E_d/\mathrm{d}t$. For the shear flow within posts

$$\frac{\mathrm{d}E_d}{\mathrm{d}t} \approx \eta 8 \left(\frac{v(t)}{w-r}\right)^2 \frac{w^2-r^2}{w^2} L_x L_y h_p. \tag{5.24}$$

Using $L_y = w_y = w$ we find for the gas and liquid

$$\text{gas}: \quad \left(\frac{\mathrm{d}E_d}{\mathrm{d}t}\right)_{p,g} \approx \eta_g 8 v^2 \frac{w+r}{w-r}\frac{L_x}{w} h_p \left(1-\frac{R_0}{L_x}\right) \tag{5.25a}$$

$$\text{liq}: \quad \left(\frac{\mathrm{d}E_d}{\mathrm{d}t}\right)_{p,l} \approx \eta_l 8 v^2 \frac{w+r}{w-r}\frac{L_x}{w} h_p \frac{R_0}{L_x}, \tag{5.25b}$$

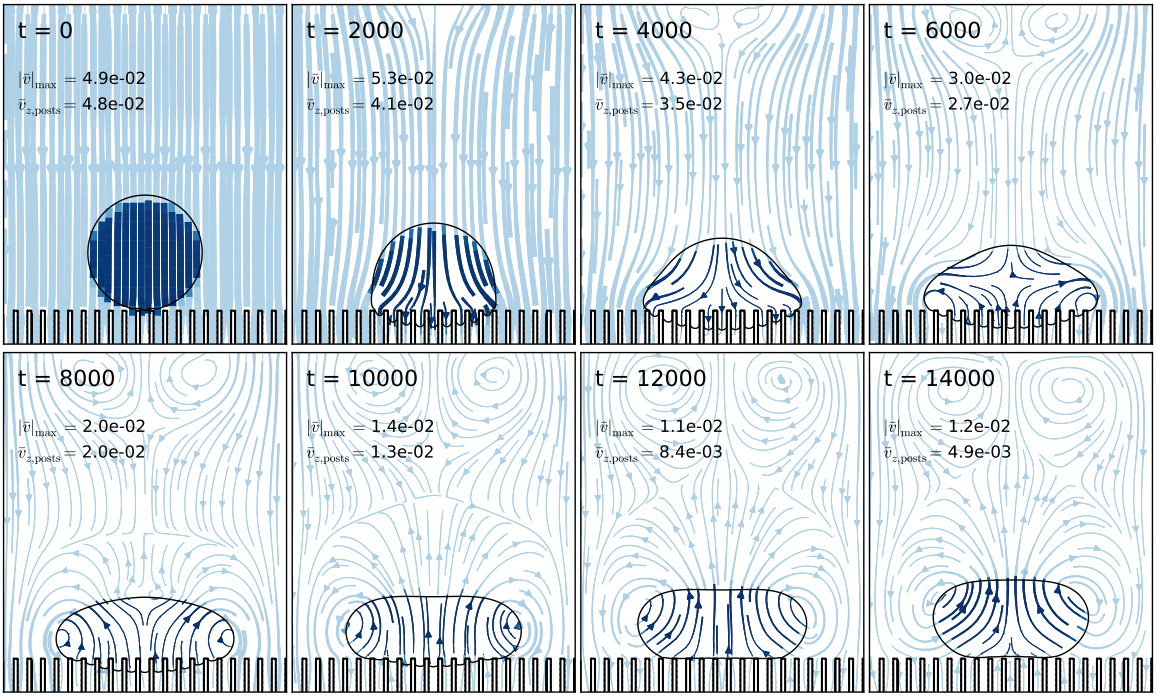


Figure 5.9: Time sequences of the velocity field for $We = 2.81$. The maximum velocity in the system and the maximum velocity of flow between the posts are listed.

which, as one would expect, is larger for higher velocities. It diverges for $r \to w$ $(r > w)$ and $w \to 0$.

In Fig. 5.8 we plot the time development of the dissipation rate for the liquid only, both shear and diffusion contributions. We can observe that indeed within the drop the dissipation between the posts, indicated by a solid line, is much higher than the dissipation happening above the posts in the body of the fluid, indicated by a dashed line. Additionally, we note that for the spreading motion above the posts most of the energy dissipation happens early, when the drop hits the surface. The dissipation during spreading and retraction is negligible.

5.3.4 Effects on $a_\downarrow$, $a_\uparrow$

In Sec. 5.1.1, we found that our measured values for $a_\downarrow$ and $a_\uparrow$ differ significantly, typically $a_\downarrow \approx 5a_\uparrow$. Moreover, for the upwards motion $a_\uparrow$ is much smaller than the calculated value ($a_\uparrow = 9.8 \times 10^{-6}$ for $m_\uparrow = m$), typically by a factor of ≈ 10.

One idea to account for the difference between $a_\downarrow$ and $a_\uparrow$ was to assume that during the

downwards motion only a certain fraction of the drop's mass is decelerated by the capillary force, as part of the liquid is also stopped just by hitting the tops of the posts. Measuring $a_\downarrow$ and $a_\uparrow$ was not possible in experiments, but the time for downwards movement and upwards movement was the same within measuring errors. Therefore, this effect is not likely to be the reason for the high difference between $a_\downarrow$ and $a_\uparrow$.

There are two aspects to the explanation. They follow from Fig. 5.9, where we show the stream lines of the velocity field, for the $y = 4$ layer crossing through the middle of the posts.

Firstly, the stream lines in the gas phase (light blue) show that not only is the liquid drop affected by the imparted capillary force, but also part of the gas phase, as viscous shear leads to part of the gas being pushed around, and dragged along with the drop. This seems to be more prevalent for the upwards motion than for downwards, but quantifying the effect is difficult. As the gas has the same density $\rho = 1$ as the liquid, its inertia is significant and the additional mass will decrease the $a_{\downarrow,\uparrow}$ imparted by F_c.

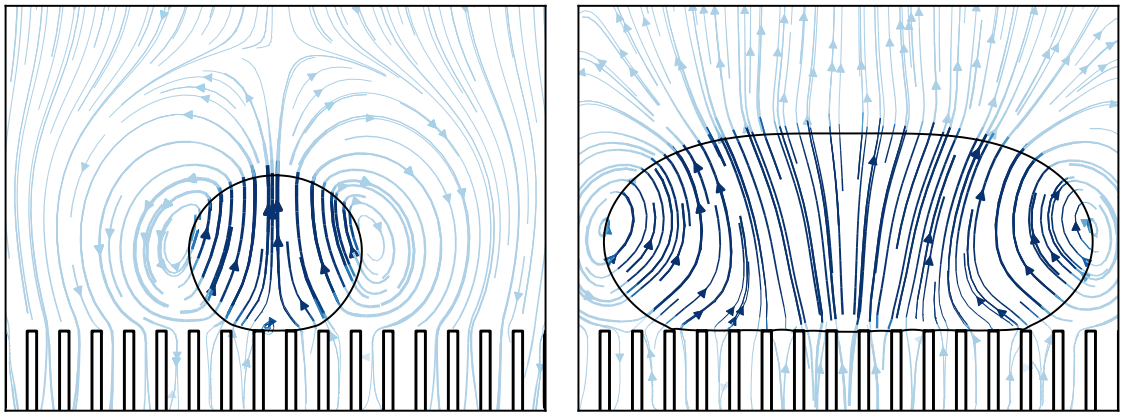
Secondly, there is significant dissipation from squeezing through the posts, which acts as an additional deceleration $a_\eta(t)$. The dissipation of energy decreases the kinetic energy in the entire system as

$$\dot{E}_d = \frac{\mathrm{d}(\frac{m_{g+l}}{2}v^2)}{\mathrm{d}t} = -m_{g+l}v(t)a_\eta(t). \tag{5.26}$$

Equating this with Eqn. (5.25a), and approximating the decelerated mass of both phases as $m_{g+l} \approx L_x L_y L_z$, gives

$$a_\eta(t) \approx \eta 8 v(t) \frac{w+r}{w-r}\frac{h_p}{L_x w^2}. \tag{5.27}$$

For a typical simulation with $\eta_g = 0.1/3$, $\eta_l = 0.5/3$, $\sigma = 0.032$, $\rho = 1$, $w = 24$, $r = 8$, $h_p = 60$, $L_x = 500$, $v_0 = 0.03$, $R_0 = 100$ this estimate gives $a_\eta(t = t_0) \approx 2.8 \times 10^{-6}$, which is not much smaller than the calculated $a_\uparrow = 9.8 \times 10^{-6}$. In addition to the large amount of gas being moved around, which decreases $a_{\downarrow,\uparrow}$, a_η will indeed affect the overall acceleration experienced by the liquid and the gas. The effect decreases with time, as $a_\eta(t) \sim v(t)$ and $v(t)$ gets smaller owing to the dissipation (see $v_z(t)$ between posts,



(a) (b)

Figure 5.10: Velocity field at approximately the time of lift-off, for (a) $R_0 = 60$ and (b) $R_0 = 120$.

given in Fig. 5.9). In fact, from Fig. 5.8, one can see that there are even two separate stages of pronounced energy dissipation in the substrate, they are roughly the imbibition motion downwards and the recoil motion upwards. The boundary of these two imbibition stages, $t_{l_{max}}$, is marked with a triangle symbol on the graph. The downwards motion, characterised by the high imbibition velocity, shows a much larger dissipation rate than the later upwards motion. The order of magnitude of their relative strength is consistent with our observation that $a_\downarrow \approx 5a_\uparrow$.

The two effects described here, an increased mass that is accelerated and an extra acceleration from dissipation, are condensed into $f_{\downarrow,\uparrow}$ which in real terms means introducing an effective mass $f_{\downarrow,\uparrow}m$ to represent the effective acceleration.

5.3.5 Vortical Flow

In the derivation of the energy criterion in Sec. 5.1.2 we assumed that we could use energy conservation to determine the kinetic energy of upwards movement. We argued that vortical motion, whose presence is suggested in [50], is not dominant in our situation, but superseded by the upwards motion of the drop's centre of mass when the drop is being pushed out of the substrate. Here we present the verification of this assumption.

Fig. 5.10 shows the stream lines of the velocity field as the drop is about to detach from the surface. The smaller drop in Fig. 5.10a has mostly finished its retraction motion, so

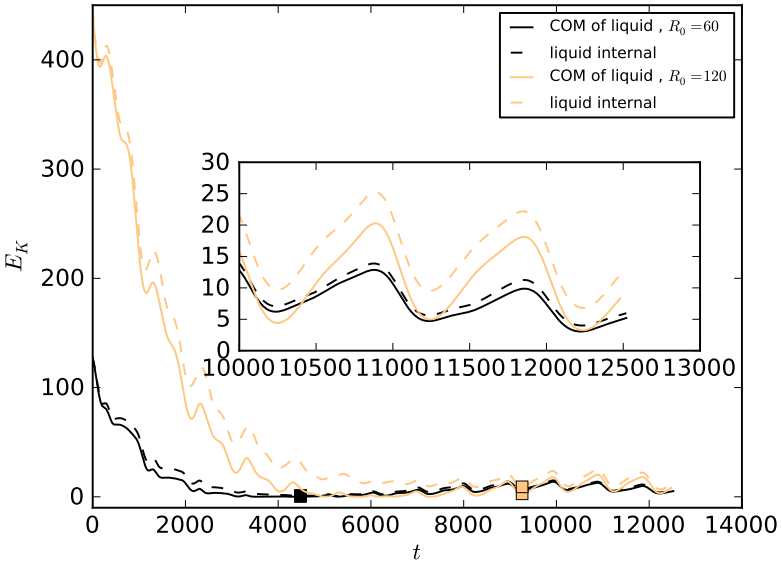


Figure 5.11: Evolution of the kinetic energy of centre-of-mass (COM) motion (solid), and of the internal motion (dashed), for two different drop sizes. The square symbols denote t_{max}, the drop jumps at the end of the plot.

the flow field should point away from the surface. The large drop in Fig. 5.10b, however, has just reached its maximum extension at the moment of lift-off. It does show lateral flow, but overall the major flow contribution is in the z direction.

We can quantify the contribution of sideways flow by comparing the kinetic energy of the centre of mass motion $E_{K,\mathrm{COM}}$, which happens only along the z direction, and the energy density within the drop integrated over the drop's volume. The latter is the 'internal' kinetic energy of the drop $E_{K,\mathrm{int}}$, it accounts for internal flow. These two types of kinetic energy are plotted in Fig. 5.11 for the drops in Fig. 5.10. We observe that despite an intermediate phase where $E_{K,\mathrm{int}} > E_{K,\mathrm{COM}}$, by the time the drop detaches $E_{K,\mathrm{int}} \approx E_{K,\mathrm{COM}}$ holds. The pronounced undulations displayed in the inset are an artefact of the initial conditions where we impose an artificial initial velocity. For the averaged motion $E_{K,\mathrm{int}} \gtrapprox E_{K,\mathrm{COM}}$ applies, but the deviations are indeed not negligible, especially for larger drops.

Therefore, we include this effect of internal flow in the prefactor f_K together with any dissipation losses during the process. In simulations, dissipation in pronounced and there is some internal motion. In experiments, we expect dissipation to be negligible,

yet internal flow, as indicated by the simulation results, cannot be omitted. Therefore application of an f_K is justified for the experiments as well.

5.4 Summary and Outlook

Summary of this chapter In this Chapter and the previous one, we have described the first experimental observation of the pancake effect which presents a significant departure from the conventional pathway of drop impacts as described in the literature to date.

Pancake bouncing was first observed on a complicated porous structure, the MTS substrate, but later shown to be a robust and universal phenomenon. Its universality was suggested by the lattice Boltzmann simulations we performed, and confirmed by drop impact experiments that followed the simulation setup, performed on highly hydrophobic post surfaces.

Guided by the simulation results two criteria were identified which lead to pancake bouncing: On the one hand, the liquid penetration and emptying process must match the time scale of droplet spreading above the posts, this gives the time scale criterion. On the other hand, the droplet must have enough kinetic energy to allow lift-off in a pancake shape, giving an energy criterion. It was verified that these are indeed two independent criteria for which two independent theoretical models could be found.

Based on observations of the imbibition process from simulations, the simple kinematic ansatz was suggested that the wetting and emptying process of the substrate could be treated as simple accelerated motion. This led to a condition on the impact Weber number which depended on the substrate parameters and drop radius. The energy criterion was found to depend only on the Weber number describing the impact. Combining both criteria allowed us to condense the physics of the pancake effect into a single design diagram.

This design diagram allowed us to both explain the experimental results and to predict the physical and substrate parameters needed to obtain pancake bouncing. The diagram

revealed that smaller post spacings or higher drop sizes or post widths must lead to a more impressive pancake effect, which only sets in at higher Weber numbers, though persists over a wider range of Weber numbers. We could also explain that shorter posts have the same effect, as they circumvent the time scale penalty of having too much imbibition. Additionally, matching our diagram with the observations on the MTS surface, we were able to explain why on that substrate the pancake effect is so impressive. The porous nature of the MTS substrate corresponds to a small effective post spacing which in turn leads to a high onset Weber number for the pancake effect, and a large region over which it can be observed. The higher Weber number means in turn that the pancake bouncing takes place when the drop is very extended.

In deriving our theoretical models for the time scale and energy criteria, we had to introduce scaling factors, some of which represented physical quantities and some of which were necessary to account for inherent limitations of the simulations. However, these scaling factors could be justified consistently, along with the other assumptions used in the derivation. In particular, we confirmed that for a bouncing process with significant transient imbibition the time for the drop to reach its maximum spreading is not necessarily best approximated by the crashing time D_0/v_0 as suggested in the literature [50, 54]. We showed that for pancake bouncing, approximating this with a fraction of the drop oscillation period gives better fits to the data.

Limitations of the simulations The biggest limitation in simulating the bouncing process on posts proved to be the density of the gas phase, as the gas' inertia had a big effect on the drop's motion. The gas acted like a cushion and prevented the drop from reaching the surface, unless the gas was started at the same initial velocity as the drop, and unless the post surface was set up without a base. These initial conditions clearly do not reflect the physical situation of a drop impact, and scaling factors had to be introduced to account for them. Moreover, the initial velocity given to both phases resulted in artificial oscillations of the velocity field over time. The outcome of this was pronounced undulations in the measured quantities. For wide posts, this meant that the

data was unreliable because the impact velocity could not be measured with sufficient accuracy.

Due to the base-free geometry of the substrate, necessary because of the inertia problem, viscous dissipation in the gas phase became a limitation too, as the gas squeezed through the post substrate. This resulted in an artificial deceleration, which affected the physical acceleration due to capillary forces from droplet-post interaction and had to be accounted for by a scaling factor.

Post height These limitations of the simulations meant that the effect of the drop hitting the base of the substrate could not be studied. This case was therefore also not included in the model. Yet, it is clear from experiments that the height of the posts has an influence on the outcome of a drop impact experiment. The experiments suggested that the pancake effect is easier to achieve on a substrate with short posts as it allows a wider range of Weber numbers that permit pancake bouncing. However, the effect of the post height is not just the trivial one of setting an upper limit on the imbibition depth. Depending on the height of the posts, there will be coupling of horizontal spreading flow between the posts and vertical imbibition motion, which will affect the ability to jump in a non-trivial manner. A study of the influence of post height would be desirable as it will add to the full understanding of the pancake effect. Yet, only simulations allowing a large difference between the densities of the phases will allow the study the influence of post height on pancake bouncing. A lattice Boltzmann algorithm based on [124] which allows viscosity and density ratios up to 1/1000 will be used for future work on this problem.

Porous structures In their initial experiments on the MTS substrate, our collaborators at the City University of Hong Kong observed that changing the height of the pillars topping the alveolar structure gave different results for the pancake effect. They found that very tall or very short pillars resulted in the pancake effect vanishing, but did not study this in detail. Their initial interpretation was that the pillar height influences the amount of lateral spreading and hence how much vertical momentum is transmitted to the

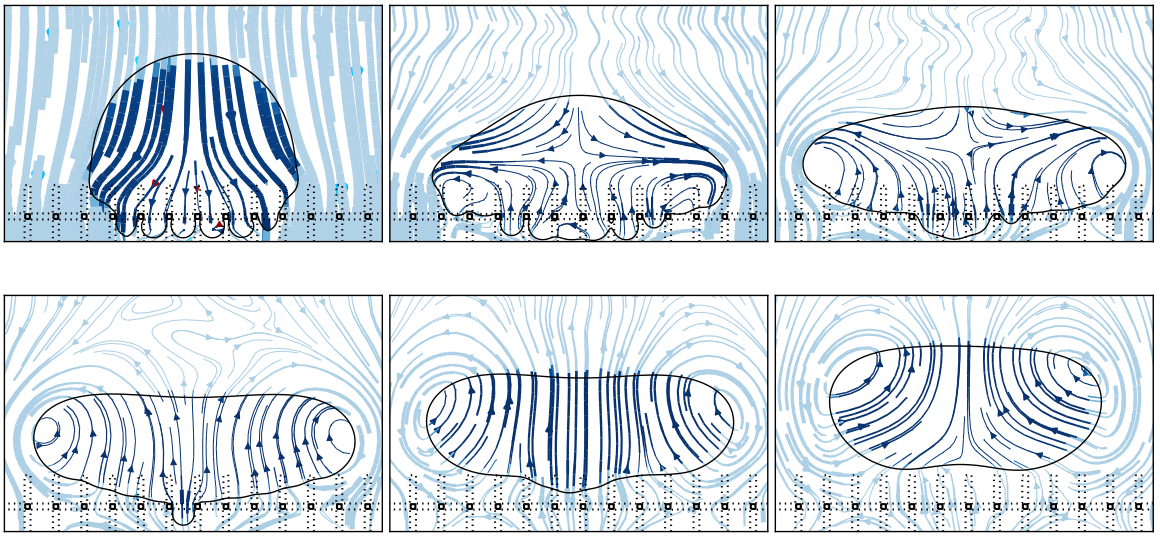


Figure 5.12: Snapshots showing the evolution of the velocity field for a substrate of square cells with $r = 6$, $w_{x,y} = 30$, $h_p = 52$, $\theta_Y = 170$, and $We = 5.66$. The sequence shows the y layer in between the posts (dashed lines) which are connected at $\frac{1}{2}h_p$ (solid lines).

drop. The results for posts presented in this chapter suggest that the pillar height might in fact simply affect the effective pillar spacing: tall posts on top of the structure mean that the imbibing liquid experiences the influence of the small hydrophobic cells later, resulting in a larger w_{eff}. For short posts, or no posts, topping the structure, w_{eff} would in our picture become so small that the onset Weber number for pancake bouncing reaches values where the drop splashes into smaller drops instead of receding and bouncing.

However, we did start to consider structures more complicated than simple posts using simulations and looked briefly into the occurrence of lateral flow. We set up substrates closer to the porous nature of the MTS, by considering rectangular cells. One such example can be seen in Fig. 5.12, a post structure where the posts are connected in the x and y directions by bars of width r at $h_p/2$. The difference to a simple post structure appears to be that the horizontal bars act as an additional barrier, increasing the surface energy of the imbibed fluid. Yet, the flow field does not seem to be influenced much by the horizontal bars.

To check whether posts are necessary to 'channel' the recoiling into upwards motion, we also tried a substrate structure consisting of horizontal bars. An example of this is

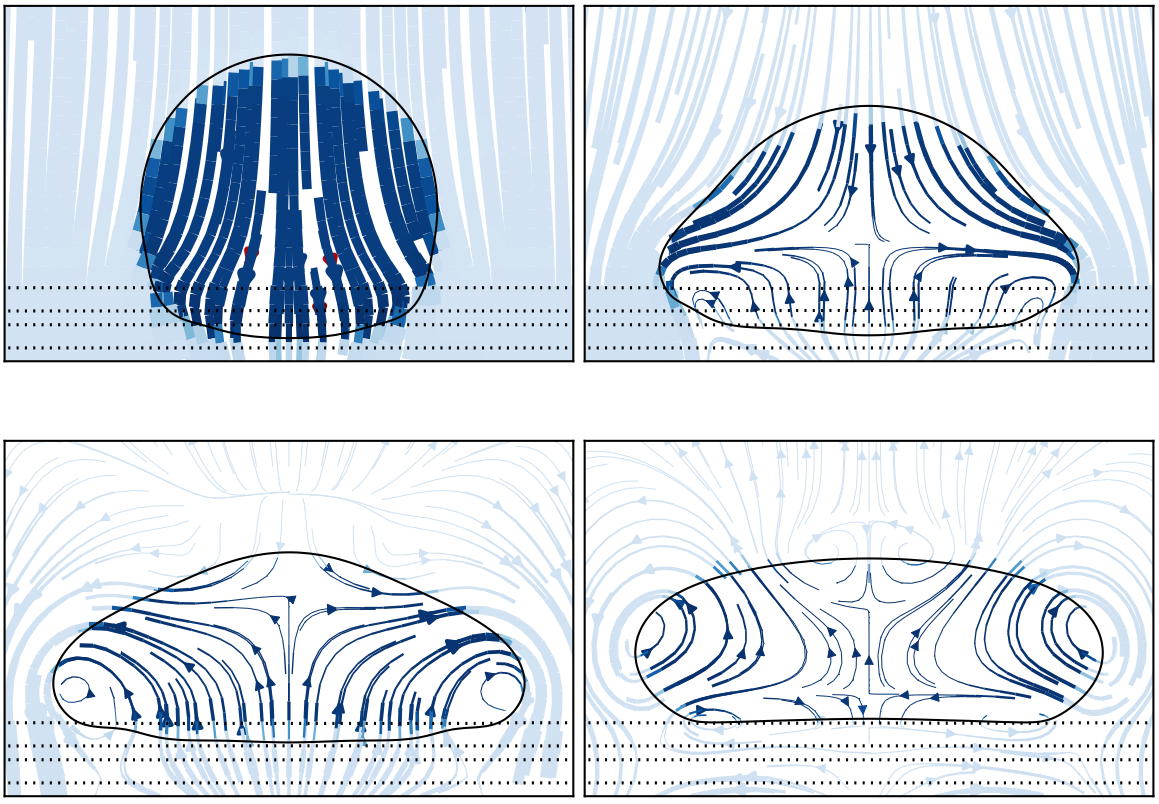


Figure 5.13: Snapshots showing the evolution of the velocity field for substrate of horizontal bars of $\theta_Y = 170°$ at $We = 4.80$. The sequence shows the y layer in between the bars which are indicated as dashed lines.

shown in Fig. 5.13. It can be seen that there is indeed an obvious recoiling motion with upwards flow, despite a lack of posts directing the flow. The drop in Fig. 5.13 does jump in a pancake shape at later time steps which are not shown.

These examples start to show that structures other than posts can be used in the simulations and can show pancake bouncing as well. This underlines that pancake bouncing is indeed a robust and universal phenomenon. Studying different structures and how they affect flow and the pancake quality would help to understand the effect in more detail and how it may be relevant to the practical applications of superhydrophobicity.

Chapter 6

Conclusions

In this thesis we investigated dynamic effects of water droplets on patterned hydrophobic surfaces using lattice Boltzmann simulations. The core of our research was formed by two physical problems: the phenomenon of droplet jumping following coalescence, and the so-called pancake effect, which describes the lift-off of a bouncing drop whilst in a flat, spread-out state. This chapter summarises our findings and concludes the work done.

The lattice Boltzmann binary model used throughout the research leading to this thesis proved very useful to study the two physical effects. We were able to correctly reproduce the general behaviour seen in experiments, and we could study the influence of different hydrodynamic parameters. In addition, the calculation of viscous and diffusive dissipation in the model that was presented in this thesis allowed us to identify sources of energy dissipation during the dynamic processes – a useful tool for future work using the binary algorithm presented here. We encountered certain difficulties related to our lattice Boltzmann binary model: the limited range of viscosities available for the binary fluid and inertial effects arising from the fact that the fluid component representing the surrounding gas had the same unit density as the liquid. Both these points will be remedied by using an algorithm based on [124], as currently being implemented in our group. In future work, it will be interesting to compare the results presented in this thesis with the outcomes of the new algorithm that allows high density and viscosity ratios.

The first physical phenomenon addressed in this thesis was that of coalescence-induced

jumping. Experimentalists had observed that for a range of drop sizes drop coalescence could lead to an out-of-plane jump of the subsequent drop. To study this effect, we first considered the two-dimensional problem of coalescence in free space. Experimental results and theoretical arguments predict a square-root scaling with time for the radius of the liquid bridge between the drops if in the capillary-inertial regime. We were able to confirm that our simulations show a capillarity and inertia driven process, and we confirmed the correct scaling for bridge radii above a certain limit resulting from the finite width of the liquid-gas interface. We then turned our attention to coalescence on a superhydrophobic substrate. When placed on a solid surface, the coalescing droplets experience a breaking of up-down symmetry, and the bulging-out bridge pushes the merged drop away from the surface due to the liquid's inertia. If this surface has a finite intrinsic contact angle the drop will experience a retardation force due to the associated adhesion energy. We show that this retardation is associated with energy dissipation, in addition to strong dissipation accompanying the coalescence process itself. If the contact angle is too low then the retardation becomes too strong, and the merged drop is prevented from jumping off the surface.

Aside from the contact angle, the topology of the surface also affects the drop's ability to jump: Surface features that run parallel to the line connecting the initial drops' centres of mass support jumping, whereas features in the perpendicular direction impede lift-off. The reason behind this is Gibbs' pinning. On solid ridges parallel to the coalescence motion there is no pinning, but on ridges perpendicular to the retraction motion the contact line has to de-pin from every ridge it encounters. We show that this de-pinning is associated with energy dissipation as the contact line detaches from the anterior edge. The energy dissipated in this process can eventually prevent the drop from lifting off the surface. Therefore, on such a surface a much higher intrinsic contact angle is necessary to allow the merged drop to jump. We show that this threshold value is smallest for ridges parallel to the coalescence motion, and highest for ridges perpendicular to this direction. For posts with a rectangular top surface, jumping is easier if the longer side lies parallel to the coalescence motion rather than perpendicular. In both cases the threshold contact

angles for jumping lie between those for ridges parallel and perpendicular to the drop retraction.

The second part of this thesis was concerned with a novel bouncing phenomenon for drop impact on superhydrophobic surfaces. Conventionally, a drop hitting a superhydrophobic surface spreads out into a puddle shape, if the impact velocity is high enough. Then the drop retracts and leaves the surface in a cigar-like shape. For certain substrates, however, a drop impacting on a solid surface can detach from the surface whilst in the puddle shape, a phenomenon termed pancake bouncing. This unusual bouncing mechanism is accompanied by a very short time the drop spends in contact with the surface. The contact time becomes up to five times smaller than in an conventional bouncing event, which makes pancake bouncing potentially relevant to many applications such as printing, thermal management, and anti-icing. On a conventional superhydrophobic surface made of cylindrical or rectangular posts, pancake bouncing is a transient effect. If the impact velocity is too high or too low, for certain surface and drop parameters, then the effect disappears and the drop bounces in the conventional way. In this thesis we identified the underlying physics of the pancake effect, and explained why it appears in a limited range of impact velocities.

Pancake bouncing requires that the impacting fluid can partially penetrate the solid structure. The energy stored as wetting interaction is then rectified into upwards motion as the liquid is pushed out of the solid. Therefore, to observe the effect relatively large topographical features are necessary (posts heights in the mm range and lateral dimensions in the 100 µm range), together with a high intrinsic contact angle. These requirements may be the reason why pancake bouncing has not been reported before. Since usually liquid penetration is not desired, typical superhydrophobic surfaces are engineered with much smaller dimensions, commonly between a few µm and 100 µm.

There are two criteria for pancake bouncing to be observed. Firstly, the time scales for lateral spreading and capillary emptying must match to allow the drop to be in a spread-out state as it tries to lift off the surface. The time scale for spreading is fixed by the drop parameters and scales with the capillary-inertial time scale. However, the time

for capillary emptying depends on the impact velocity, drop parameters, and the surface parameters. This explains the transient nature of the effect. If the impact velocity is too small then the penetrated liquid returns too early, while the drop is still spreading out such that drop's remaining downward momentum prevents jumping. If the impact velocity is too large, the liquid returns too late such that the drop has already retracted.

Secondly, the impact energy must be large enough, otherwise the capillary emptying may have finished at the right time, but the drop's kinetic energy of upwards motion is not enough to overcome surface adhesion. Taking into account the difference in drop surface energy before the impact and at lift-off, and allowing for dissipative effects, we find that there is a threshold Weber number $\gtrapprox 1$ for pancake bouncing. Both the time scale and energy criteria together were condensed into a design diagram which explains the different *We* ranges for pancake bouncing on different surfaces, and how the choice of surface parameters may be used to enhance the effect.

The research presented in this thesis establishes the groundwork for the pancake effect. Recently, our experimental collaborators have shown in a new set of experiments that the effect can be improved by using tapered posts. The slanted sides have the effect that the capillary force pushing the liquid out of the structure becomes proportional to the penetration depth. This turns the process of fluid penetration and capillary emptying into a harmonic process, with the result that the time for emptying the structure should become independent of the impact velocity. As the drop spreading time is independent of the impact velocity already, the criterion of matching time scales is therefore predicted to be independent of the impact velocity. Indeed, experiments show that for tapered posts the pancake effect persists over a much larger range of Weber numbers, up to $We \approx 60$, limited only by the liquid reaching the base of the substrate and introducing a velocity dependence again.

To conclude, the pancake effect is an exciting new amendment to our knowledge of wetting and superhydrophobicity with a lot of interesting aspects yet to study.

References

[1] Young, T. An essay on the cohesion of fluids. *Philosophical Transactions of the Royal Society of London* **95**, 65–87 (1805). 2

[2] Quéré, D. Rough ideas on wetting. *Physica A: Statistical Mechanics and its Applications* **313**, 32–46 (2002). 3

[3] Lafuma, A. & Quéré, D. Superhydrophobic states. *Nature materials* **2**, 457–460 (2003). 3, 5, 6

[4] Onda, T., Shibuichi, S., Satoh, N. & Tsujii, K. Super-water-repellent fractal surfaces. *Langmuir* **12**, 2125–2127 (1996). URL `http://pubs.acs.org/doi/abs/10.1021/la950418o`. 3

[5] Koch, K. & Barthlott, W. Superhydrophobic and superhydrophilic plant surfaces: an inspiration for biomimetic materials. *Phil. Trans. R. Soc. A* **367**, 1487–1509 (2009). 3

[6] Neinhuis, C. & Barthlott, W. Characterization and distribution of water-repellent, self-cleaning plant surfaces. *Ann. Bot.* **79**, 667–677 (1997). 3

[7] Barthlott, W. & Neinhuis, C. Purity of the sacred lotus, or escape from contamination in biological surfaces. *Planta* **202**, 1–8 (1997). 3

[8] Hartley, G. & Brunskill, R. Reflection of water drops from surfaces. *Surface phenomena in chemistry and biology* **214** (1958). 3, 13, 14

[9] Blossey, R. Self-cleaning surfacesâĂŤvirtual realities. *Nature materials* **2**, 301–306 (2003). 4

[10] Bhushan, B. & Jung, Y. C. Wetting, adhesion and friction of superhydrophobic and hydrophilic leaves and fabricated micro/nanopatterned surfaces. *Journal of Physics: Condensed Matter* **20**, 225010 (2008). 4

[11] Carlborg, C. F. & van der Wijngaart, W. Sustained superhydrophobic friction reduction at high liquid pressures and large flows. *Langmuir* **27**, 487–493 (2010). 4

[12] Parker, A. R. & Lawrence, C. R. Water capture by a desert beetle. *Nature* **414**, 33–34 (2001). URL `doi:10.1038/35102108`. 4, 9

[13] Dorrer, C. & Rühe, J. Mimicking the stenocara beetle - dewetting of drops from a patterned superhydrophobic surface. *Langmuir* **24**, 6154–6158 (2008). 4, 9

[14] Dietz, C., Rykaczewski, K., Fedorov, A. & Joshi, Y. Visualization of droplet departure on a superhydrophobic surface and implications to heat transfer enhancement during dropwise condensation. *Applied Physics Letters* **97**, 033104–033104 (2010). 4, 35

[15] Shirtcliffe, N. J. *et al.* The use of high aspect ratio photoresist (su-8) for superhydrophobic pattern prototyping. *Journal of Micromechanics and Microengineering* **14**, 1384 (2004). URL http://stacks.iop.org/0960-1317/14/i=10/a=013. 4

[16] He, B., Patankar, N. A. & Lee, J. Multiple equilibrium droplet shapes and design criterion for rough hydrophobic surfaces. *Langmuir* **19**, 4999–5003 (2003). 4

[17] He, M. *et al.* Hierarchically structured porous aluminum surfaces for high-efficient removal of condensed water. *Soft Matter* **8**, 6680–6683 (2012). 4, 33

[18] Lai, Y. *et al.* Designing superhydrophobic porous nanostructures with tunable water adhesion. *Advanced Materials* **21**, 3799–3803 (2009). 4

[19] Chen, C.-H. *et al.* Dropwise condensation on superhydrophobic surfaces with two-tier roughness. *Appl. Phys. Lett.* **90**, 173108 (2007). 4, 30, 35

[20] Chen, X. *et al.* Nanograssed micropyramidal architectures for continuous dropwise condensation. *Advanced Functional Materials* **21**, 4617–4623 (2011). URL http://dx.doi.org/10.1002/adfm.201101302. 4, 35

[21] Cassie, A. B. D. & Baxter, S. Wettability of porous surfaces. *Trans. Faraday Soc.* **40**, 546–551 (1944). URL doi:10.1039/b904807c. 5

[22] Wenzel, R. N. Resistance of solid surfaces to wetting by water. *Industrial & Engineering Chemistry* **28**, 988–994 (1936). 5

[23] Jung, Y. C. & Bhushan, B. Dynamic effects induced transition of droplets on biomimetic superhydrophobic surfaces. *Langmuir* **25**, 9208–9218 (2009). URL http://pubs.acs.org/doi/abs/10.1021/la900761u. PMID: 19441842. 6

[24] Quéré, D. Non-sticking drops. *Reports on Progress in Physics* **68**, 2495 (2005). URL http://stacks.iop.org/0034-4885/68/i=11/a=R01. 6

[25] Richard, D. & Quéré, D. Viscous drops rolling on a tilted non-wettable solid. *Europhys. Lett.* **48**, 286 (1999). URL doi:10.1209/epl/i1999-00479-1. 6, 35

[26] Richard, D. & Quéré, D. Bouncing water drops. *EPL (Europhysics Letters)* **50**, 769 (2000). URL http://stacks.iop.org/0295-5075/50/i=6/a=769. 6, 12, 14, 82

[27] Patankar, N. A. Transition between superhydrophobic states on rough surfaces. *Langmuir* **20**, 7097–7102 (2004). URL DOI:10.1021/la049329e. 6

[28] Ishino, C., Okumura, K. & Quéré, D. Wetting transitions on rough surfaces. *Europhys. Lett.* **68**, 419 (2004). URL http://stacks.iop.org/0295-5075/68/i=3/a=419. 6

[29] Liu, B. & Lange, F. F. Pressure induced transition between superhydrophobic states: Configuration diagrams and effect of surface feature size. *Journal of colloid and interface science* **298**, 899–909 (2006). 6

[30] Bormashenko, E., Pogreb, R., Whyman, G., Bormashenko, Y. & Erlich, M. Vibration-induced Cassie-Wenzel wetting transition on rough surfaces. *Applied Physics Letters* **90**, 201917 –201917–2 (2007). 6

[31] Kusumaatmaja, H., Blow, M. L., Dupuis, A. & Yeomans, J. M. The collapse transition on superhydrophobic surfaces. *Europhys. Lett.* **81**, 36003 (2008). URL `http://stacks.iop.org/0295-5075/81/i=3/a=36003`. 6

[32] McHale, G., Aqil, S., Shirtcliffe, N. J., Newton, M. I. & Erbil, H. Y. Analysis of droplet evaporation on a superhydrophobic surface. *Langmuir* **21**, 11053–11060 (2005). URL `http://pubs.acs.org/doi/abs/10.1021/la0518795`. 6

[33] de Gennes, P. G. Wetting: statics and dynamics. *Rev. Mod. Phys.* **57**, 827–863 (1985). URL `http://link.aps.org/doi/10.1103/RevModPhys.57.827`. 6

[34] Gibbs, J. W. On the equilibrium of heterogeneous substances, part 2. *Transactions of the Connecticut Academy* **III**, 343–524 (1878). 6

[35] Oliver, J. F., Huh, C. & Mason, S. G. Resistance to spreading of liquids by sharp edges. *Journal of Colloid and Interface Science* **59**, 568 – 581 (1977). URL `http://www.sciencedirect.com/science/article/B6WHR-4CT7CTJ-2T/2/3cd2087d7e33297264a8ec7bf89ae2b8`. 7

[36] De Gennes, P.-G., Brochard-Wyart, F. & Quéré, D. *Capillarity and wetting phenomena: drops, bubbles, pearls, waves* (Springer, 2004). 7

[37] Worthington, A. M. On the forms assumed by drops of liquids falling vertically on a horizontal plate. *Proceedings of the Royal Society of London* **25**, 261–272 (1876). URL `http://rspl.royalsocietypublishing.org/content/25/171-178/261.short`. 9

[38] Worthington, A. M. A second paper on the forms assumed by drops of liquids falling vertically on a horizontal plate. *Proceedings of the Royal Society of London* **25**, 498–503 (1876). URL `http://rspl.royalsocietypublishing.org/content/25/171-178/498.short`. 9

[39] Worthington, A. M. & Cole, R. S. Impact with a liquid surface, studied by the aid of instantaneous photography. *Philosophical Transactions of the Royal Society of London. Series A, Containing Papers of a Mathematical or Physical Character* **189**, pp. 137–148 (1897). URL `http://www.jstor.org/stable/90692`. 9

[40] Reyssat, M., Richard, D., Clanet, C. & Quéré, D. Dynamical superhydrophobicity. *Faraday discussions* **146**, 19–33 (2010). 9

[41] Chandra, S. & Avedisian, C. T. On the collision of a droplet with a solid surface **432**, 13–41 (1991). URL `http://rspa.royalsocietypublishing.org/content/432/1884/13.abstract`. 9, 83

[42] Zhai, L. *et al.* Patterned superhydrophobic surfaces: Toward a synthetic mimic of the namib desert beetle. *NANO LETTERS* **6**, 1213–1217 (2006). 9

[43] Garrod, R. P. *et al.* Mimicking a stenocara beetle's back for microcondensation using plasmachemical patterned superhydrophobic-superhydrophilic surfaces. *Langmuir* **23**, 689–693 (2007). 9

[44] Rioboo, R., Marengo, M. & Tropea, C. Time evolution of liquid drop impact onto solid, dry surfaces. *Experiments in Fluids* **33**, 112–124 (2002). URL `http://dx.doi.org/10.1007/s00348-002-0431-x`. 10, 11, 12

[45] Biance, A.-L., Clanet, C. & Quéré, D. First steps in the spreading of a liquid droplet. *Phys. Rev. E* **69**, 016301 (2004). URL `http://link.aps.org/doi/10.1103/PhysRevE.69.016301`. 11

[46] Rein, M. Phenomena of liquid drop impact on solid and liquid surfaces. *Fluid Dynamics Research* **12**, 61 – 93 (1993). URL `http://www.sciencedirect.com/science/article/pii/016959839390106K`. 12, 13

[47] Yarin, A. Drop impact dynamics: splashing, spreading, receding, bouncingâĂę. *Annu. Rev. Fluid Mech.* **38**, 159–192 (2006). 12

[48] Brown, P. *et al.* Impact of picoliter droplets on superhydrophobic surfaces with ultralow spreading ratios. *Langmuir* **27**, 13897–13903 (2011). 12

[49] Tanner, L. H. The spreading of silicone oil drops on horizontal surfaces. *Journal of Physics D: Applied Physics* **12**, 1473 (1979). URL `http://stacks.iop.org/0022-3727/12/i=9/a=009`. 12

[50] Clanet, C., Béguin, C., Richard, D., Quéré, D. *et al.* Maximal deformation of an impacting drop. *Journal of Fluid Mechanics* **517**, 199–208 (2004). 12, 13, 83, 84, 85, 110, 111, 112, 113, 127, 129, 130, 131, 136, 139

[51] Roisman, I. V., Rioboo, R. & Tropea, C. Normal impact of a liquid drop on a dry surface: model for spreading and receding **458**, 1411–1430 (2002). URL `http://rspa.royalsocietypublishing.org/content/458/2022/1411.abstract`. 13

[52] Planchette, C., Biance, A. & Lorenceau, E. Transition of liquid marble impacts onto solid surfaces. *EPL (Europhysics Letters)* **97**, 14003 (2012). 13

[53] Biance, A.-L., Chevy, F., Clanet, C., Lagubeau, G. & Quéré, D. On the elasticity of an inertial liquid shock. *Journal of Fluid Mechanics* **554**, 47–66 (2006). 13, 14, 81, 83, 84, 85, 118, 130

[54] Schiaffino, S. & Sonin, A. A. Molten droplet deposition and solidification at low weber numbers. *Physics of Fluids* **9**, 3172–3187 (1997). URL `http://link.aip.org/link/?PHF/9/3172/1`. 13, 14, 111, 130, 139

[55] Okumura, K., Chevy, F., Richard, D., Quéré, D. & Clanet, C. Water spring: A model for bouncing drops. *EPL (Europhysics Letters)* **62**, 237 (2003). 13, 81, 82, 118, 130

[56] Courty, S., Lagubeau, G. & Tixier, T. Oscillating droplets by decomposition on the spherical harmonics basis. *Phys. Rev. E* **73**, 045301 (2006). URL `http://link.aps.org/doi/10.1103/PhysRevE.73.045301`. 13, 81, 82, 118

[57] Rein, M. *Drop-surface interactions*. 456 (Springer, 2002). 13

[58] Brunskill, R. Physical factors affecting the retention of spray droplets on leaf surfaces. In *Proceedings of the Third British Weed Control Conference*, vol. 2, 593–603 (1956). 14

[59] Bartolo, D. *et al.* Bouncing or sticky droplets: Impalement transitions on superhydrophobic micropatterned surfaces. *EPL (Europhysics Letters)* **74**, 299 (2006). 14, 85, 86, 87

[60] Puthenveettil, B. A., Senthilkumar, V. K. & Hopfinger, E. J. Motion of drops on inclined surfaces in the inertial regime. *Journal of Fluid Mechanics* **726**, 26–61 (2013). 14

[61] Yao, S.-C. & Cai, K. Y. The dynamics and leidenfrost temperature of drops impacting on a hot surface at small angles. *Experimental Thermal and Fluid Science* **1**, 363–371 (1988). 15

[62] Yeomans, J. Mesoscale simulations: Lattice Boltzmann and particle algorithms. *Physica A: Statistical and Theoretical Physics* **369**, 159–184 (2006). URL `http://www.sciencedirect.com/science/article/B6TVG-4K426BC-1/2/53efb17e079f597ffd3957a8739da873`. 17

[63] Pomeau, B. H. Y. & Frisch, U. Lattice-gas automata for the navier-stokes equation. *Phys. Rev. Lett* **56**, 1505 (1986). 17

[64] Briant, A. J. & Yeomans, J. M. Lattice Boltzmann simulations of contact line motion. ii. binary fluids. *Phys. Rev. E* **69**, 031603 (2004). URL `http://link.aps.org/doi/10.1103/PhysRevE.69.031603`. 17, 19, 20

[65] Kusumaatmaja, H. & Yeomans, J. M. Lattice Boltzmann simulations of wetting and drop dynamics. In *Simulating Complex Systems by Cellular Automata*, 241–274 (Springer, 2010). 18, 19, 20, 21, 22, 25

[66] Briant, A., Wagner, A. & Yeomans, J. Lattice Boltzmann simulations of contact line motion. i. liquid-gas systems. *Physical Review E* **69**, 031602 (2004). 18

[67] Cahn, J. W. Critical point wetting. *The Journal of Chemical Physics* **66**, 3667 (1977). 19

[68] Briant, A. Lattice Boltzmann simulations of contact line motion in a liquid-gas system. *Philosophical Transactions of the Royal Society of London. Series A: Mathematical, Physical and Engineering Sciences* **360**, 485–495 (2002). 20

[69] Succi, S. *The lattice Boltzmann equation: for fluid dynamics and beyond* (Oxford university press, 2001). 21, 23

[70] Bhatnagar, P. L., Gross, E. P. & Krook, M. A model for collision processes in gases. i. small amplitude processes in charged and neutral one-component systems. *Physical review* **94**, 511 (1954). 21

[71] Swift, M. R., Orlandini, E., Osborn, W. & Yeomans, J. Lattice Boltzmann simulations of liquid-gas and binary fluid systems. *Physical Review E* **54**, 5041 (1996). 23

[72] Pooley, C. & Furtado, K. Eliminating spurious velocities in the free-energy lattice Boltzmann method. *Physical Review E* **77**, 046702 (2008). 23, 24, 25

[73] Wagner, A. J. The origin of spurious velocities in lattice Boltzmann. *International Journal of Modern Physics B* **17**, 193–196 (2003). 23

[74] Pooley, C., Kusumaatmaja, H. & Yeomans, J. Contact line dynamics in binary lattice Boltzmann simulations. *Physical Review E* **78**, 056709 (2008). 25, 26

[75] Ladd, A. J. Numerical simulations of particulate suspensions via a discretized Boltzmann equation. part 1. theoretical foundation. *Journal of Fluid Mechanics* **271**, 285–309 (1994). 26

[76] Qian, T., Wang, X.-P. & Sheng, P. A variational approach to moving contact line hydrodynamics. *Journal of Fluid Mechanics* **564**, 146 (2006). 26, 27

[77] Boreyko, J. B. & Chen, C.-H. Self-propelled dropwise condensate on superhydrophobic surfaces. *Phys. Rev. Lett.* **103**, 184501 (2009). URL `http://journals.aps.org/prl/abstract/10.1103/PhysRevLett.103.184501`. 29, 30, 31, 32, 35, 39, 45, 56, 57, 58, 69

[78] Lienhard IV, J. H. & Lienhard V, J. H. *A heat transfer textbook* (Phlogiston Press, Cambridge, 2003), 3 edn. 30

[79] Eggers, J., Lister, J. A. & Stone, H. A. Coalescence of liquid drops. *J. Fluid Mech.* **401**, 293–310 (1999). 32, 36, 37, 38, 49

[80] Richard, D., Clanet, C. & Quéré, D. Contact time of a bouncing drop. *Nature* **417**, 811 (2002). 32, 80, 81, 82, 110, 118, 130

[81] Aarts, D. G. A. L., Lekkerkerker, H. N. W., Guo, H., Wegdam, G. H. & Bonn, D. Hydrodynamics of droplet coalescence. *Phys. Rev. Lett.* **95**, 164503 (2005). URL `http://link.aps.org/doi/10.1103/PhysRevLett.95.164503`. 32, 36, 37, 38, 51

[82] Andrieu, C., Beysens, D. A., Nikolayev, V. S. & Pomeau, Y. Coalescence of sessile drops. *Journal of Fluid Mechanics* **453**, 427–438 (2002). URL `http://dx.doi.org/10.1017/S0022112001007121`. 32, 36, 37, 39

[83] Narhe, R. D., Beysens, D. A. & Pomeau, Y. Dynamic drying in the early-stage coalescence of droplets sitting on a plate. *EPL (Europhysics Letters)* **81**, 46002 (2008). URL `http://stacks.iop.org/0295-5075/81/i=4/a=46002`. 32, 36, 37, 39

[84] Wang, F.-C., Yang, F. & Zhao, Y.-P. Size effect on the coalescence-induced self-propelled droplet. *Applied Physics Letters* **98**, 053112 –053112–3 (2011). 32, 33, 55, 56, 57, 69

[85] Gao, L. & McCarthy, T. J. An attempt to correct the faulty intuition perpetuated by the Wenzel and Cassie "laws". *Langmuir* **25**, 7249–7255 (2009). URL `http://pubs.acs.org/doi/abs/10.1021/la901416m`. PMID: 19518141. 33

[86] Bonn, D., Eggers, J., Indekeu, J., Meunier, J. & Rolley, E. Wetting and spreading. *Rev. Mod. Phys.* **81**, 739–805 (2009). 33

[87] Liu, T., Sun, W., Sun, X. & Ai, H. Mechanism study of condensed drops jumping on super-hydrophobic surfaces. *Colloids and Surfaces A: Physicochemical and Engineering Aspects* (2012). 33, 34, 53, 56, 62, 69

[88] Rose, J. Dropwise condensation theory and experiment: a review. *Proceedings of the Institution of Mechanical Engineers, Part A: Journal of Power and Energy* **216**, 115–128 (2002). 34

[89] Rose, J. & Glicksman, L. Dropwise condensation–the distribution of drop sizes. *International Journal of Heat and Mass Transfer* **16**, 411 – 425 (1973). URL `http://www.sciencedirect.com/science/article/B6V3H-4829PT3-1XS/2/585cb8e5ba624e62709ea2945f9d5d1f`. 34

[90] Graham, C. & Griffith, P. Drop size distributions and heat transfer in dropwise condensation. *International Journal of Heat and Mass Transfer* **16**, 337–346 (1973). 34

[91] Dimitrakopoulos, P. & Higdon, J. On the gravitational displacement of three-dimensional fluid droplets from inclined solid surfaces. *Journal of Fluid Mechanics* **395**, 181–209 (1999). 35

[92] Rykaczewski, K. *et al.* Multimode multidrop serial coalescence effects during condensation on hierarchical superhydrophobic surfaces. *Langmuir* **29**, 881–891 (2013). 35

[93] Miljkovic, N., Enright, R. & Wang, E. N. Effect of droplet morphology on growth dynamics and heat transfer during condensation on superhydrophobic nanostructured surfaces. *Acs Nano* **6**, 1776–1785 (2012). 35

[94] Hopper, R. W. Coalescence of two equal cylinders: Exact results for creeping viscous plane flow driven by capillarity. *Journal of the American Ceramic Society* **67**, C–262–C–264 (1984). URL `http://dx.doi.org/10.1111/j.1151-2916.1984.tb19692.x`. 36

[95] Hopper, R. W. Plane stokes flow driven by capillarity on a free surface. *Journal of Fluid Mechanics* **213**, 349–375 (1990). URL `http://dx.doi.org/10.1017/S002211209000235X`. 36, 37

[96] Hopper, R. W. Coalescence of two viscous cylinders by capillarity: Part i, theory. *Journal of the American Ceramic Society* **76**, 2947–2952 (1993). URL `http://dx.doi.org/10.1111/j.1151-2916.1993.tb06594.x`. 36

[97] Hopper, R. W. Coalescence of two viscous cylinders by capillarity: Part ii, shape evolution. *Journal of the American Ceramic Society* **76**, 2953–2960 (1993). URL http://dx.doi.org/10.1111/j.1151-2916.1993.tb06595.x. 36

[98] Duchemin, L., Eggers, J. & Josserand, C. Inviscid coalescence of drops. *J. Fluid Mech.* **487**, 167–178 (2003). 36, 38, 40, 51

[99] Paulsen, J. D. *et al.* The inexorable resistance of inertia determines the initial regime of drop coalescence. *Proc Natl Acad Sci USA* **109**, 6857–6861 (2012). 36, 37, 38, 51

[100] Jia, X., McLaughlin, J. & Kontomaris, K. Lattice Boltzmann simulations of drop coalescence and chemical mixing. *Physica A: Statistical Mechanics and its Applications* **362**, 62 – 67 (2006). URL http://www.sciencedirect.com/science/article/pii/S0378437105009532. 36

[101] Gross, M., Steinbach, I., Raabe, D. & Varnik, F. Viscous coalescence of droplets: A lattice Boltzmann study. *Physics of Fluids* **25**, 052101 (2013). 36, 38, 45, 47

[102] Paulsen, J. D., Burton, J. C. & Nagel, S. R. Viscous to inertial crossover in liquid drop coalescence. *Phys. Rev. Lett.* **106**, 114501 (2011). URL http://link.aps.org/doi/10.1103/PhysRevLett.106.114501. 36, 37, 38, 40, 51

[103] Menchaca-Rocha, A., Martínez-Dávalos, A., Núñez, R., Popinet, S. & Zaleski, S. Coalescence of liquid drops by surface tension. *Phys. Rev. E* **63**, 046309 (2001). URL http://link.aps.org/doi/10.1103/PhysRevE.63.046309. 36, 38, 51

[104] Burton, J. C. & Taborek, P. Role of dimensionality and axisymmetry in fluid pinch-off and coalescence. *Phys. Rev. Lett.* **98**, 224502 (2007). URL http://link.aps.org/doi/10.1103/PhysRevLett.98.224502. 36, 38, 51

[105] Narhe, R., Beysens, D. & Nikolayev, V. S. Contact line dynamics in drop coalescence and spreading. *Langmuir* **20**, 1213–1221 (2004). URL http://pubs.acs.org/doi/abs/10.1021/la034991g. PMID: 15803699. 36

[106] Narhe, R., Beysens, D. & Nikolayev, V. Dynamics of drop coalescence on a surface: The role of initial conditions and surface properties. *International Journal of Thermophysics* **26**, 1743–1757 (2005). URL http://dx.doi.org/10.1007/s10765-005-8593-4. 10.1007/s10765-005-8593-4. 36, 39

[107] Thoroddsen, S., Takehara, K. & Etoh, T. The coalescence speed of a pendent and a sessile drop. *Journal of Fluid Mechanics* **527**, 85–114 (2005). 37

[108] Thoroddsen, S., Etoh, T., Takehara, K. & Ootsuka, N. On the coalescence speed of bubbles. *Physics of Fluids* **17**, 071703 (2005). 37

[109] Yao, W., Maris, H. J., Pennington, P. & Seidel, G. M. Coalescence of viscous liquid drops. *Phys. Rev. E* **71**, 016309 (2005). URL http://link.aps.org/doi/10.1103/PhysRevE.71.016309. 38, 39, 51

[110] Pomeau, Y. Recent progress in the moving contact line problem: a review. *Comptes Rendus Mécanique* **330**, 207 – 222 (2002). URL http://www.sciencedirect.com/science/article/pii/S1631072102014456. 39

[111] Pomeau, Y. Contact line moving on a solid. *The European Physical Journal Special Topics* **197**, 15–31 (2011). URL http://dx.doi.org/10.1140/epjst/e2011-01432-1. 39

[112] Thompson, P. A. & Robbins, M. O. Simulations of contact-line motion: slip and the dynamic contact angle. *Physical Review Letters* **63**, 766 (1989). 39

[113] Huh, C. & Scriven, L. Hydrodynamic model of steady movement of a solid/liquid/fluid contact line. *Journal of Colloid and Interface Science* **35**, 85–101 (1971). 39

[114] Dussan, V. *et al.* The moving contact line: the slip boundary condition. *Journal of Fluid mechanics* **77**, 665–684 (1976). 39

[115] Eggers, J. Nonlinear dynamics and breakup of free-surface flows. *Rev. Mod. Phys.* **69**, 865–930 (1997). URL http://link.aps.org/doi/10.1103/RevModPhys.69.865. 39

[116] Boreyko, J. B. & Chen, C.-H. Restoring superhydrophobicity of lotus leaves with vibration-induced dewetting. *Phys. Rev. Lett.* **103**, 174502 (2009). 55

[117] Marmur, A. & Bittoun, E. When Wenzel and Cassie are right: Reconciling local and global considerations. *Langmuir* **25**, 1277–1281 (2009). URL http://pubs.acs.org/doi/abs/10.1021/la802667b. 65

[118] Choi, W., Tuteja, A., Mabry, J. M., Cohen, R. E. & McKinley, G. H. A modified Cassie-Baxter relationship to explain contact angle hysteresis and anisotropy on non-wetting textured surfaces. *Journal of Colloid and Interface Science* **339**, 208 – 216 (2009). URL http://www.sciencedirect.com/science/article/B6WHR-4WSRF3X-3/2/c83e4ea1e367ff0b0f421e4ba38ee710. 65

[119] Dorrer, C. & Rühe, J. Advancing and receding motion of droplets on ultrahydrophobic post surfaces. *Langmuir* **22**, 7652–7657 (2006). 67

[120] Extrand, C. W. Model for contact angles and hysteresis on rough and ultraphobic surfaces. *Langmuir* **18**, 7991–7999 (2002). URL http://pubs.acs.org/doi/abs/10.1021/la025769z. 67

[121] Kusumaatmaja, H. & Yeomans, J. Modeling contact angle hysteresis on chemically patterned and superhydrophobic surfaces. *Langmuir* **23**, 6019–6032 (2007). 67

[122] Kusumaatmaja, H., Pooley, C., Girardo, S., Pisignano, D. & Yeomans, J. Capillary filling in patterned channels. *Physical Review E* **77**, 067301 (2008). 67

[123] Patankar, N. A. Hysteresis with regard to Cassie and Wenzel states on superhydrophobic surfaces. *Langmuir* **26**, 7498–7503 (2010). 67

[124] Lee, T. & Liu, L. Lattice Boltzmann simulations of micron-scale drop impact on dry surfaces. *Journal of Computational Physics* **229**, 8045–8063 (2010). 72, 140, 143

[125] Moevius, L., Liu, Y., Wang, Z. & Yeomans, J. Pancake bouncing on superhydrophobic surfaces, to be published (2013). 73

[126] Rayleigh, L. On the capillary phenomena of jets. *Proc. R. Soc. Lond.* **29**, 71–97 (1879). 80

[127] Vincent, F., Goff, A. L., Lagubeau, G. & Quere, D. Bouncing bubbles. *Journal of Adhesion* **83**, 897–906 (2007). URL `http://www.ingentaconnect.com/content/tandf/gadh/2007/00000083/00000010/art00002`. 81, 103, 110, 118, 130

[128] Chevy, F., Chepelianskii, A., Quéré, D. & Raphaël, E. Liquid hertz contact: softness of weakly deformed drops on non-wetting substrates. *arXiv preprint arXiv:1209.5377* (2012). 81, 82

[129] Lamb, H. *Hydrodynamics* (Cambridge University Press, 1993). 81, 103

[130] Merlen, A. & Brunet, P. Impact of drops on non-wetting biomimetic surfaces. *Journal of Bionic Engineering* **6**, 330 – 334 (2009). URL `http://www.sciencedirect.com/science/article/pii/S1672652908601419`. 83, 84

[131] Reyssat, M., Pépin, A., Marty, F., Chen, Y. & Quéré, D. Bouncing transitions on microtextured materials. *EPL (Europhysics Letters)* **74**, 306 (2006). 85, 86

[132] Tsai, P., Pacheco, S., Pirat, C., Lefferts, L. & Lohse, D. Drop impact upon micro- and nanostructured superhydrophobic surfaces. *Langmuir* **25**, 12293–12298 (2009). 86

[133] Hee Kwon, D. & Joon Lee, S. Impact and wetting behaviors of impinging microdroplets on superhydrophobic textured surfaces. *Applied Physics Letters* **100**, 171601–171601 (2012). 86, 87, 88, 89

[134] Jung, Y. C. & Bhushan, B. Dynamic effects of bouncing water droplets on superhydrophobic surfaces. *Langmuir* **24**, 6262–6269 (2008). URL `http://pubs.acs.org/doi/abs/10.1021/la8003504`. PMID: 18479153. 86

[135] Reyssat, M., Yeomans, J. & Quéré, D. Impalement of fakir drops. *EPL (Europhysics Letters)* **81**, 26006 (2008). 86

[136] Patankar, N. A. Consolidation of hydrophobic transition criteria by using an approximate energy minimization approach. *Langmuir* **26**, 8941–8945 (2010). URL `http://pubs.acs.org/doi/abs/10.1021/la9047424`. PMID: 20158175. 86, 87

[137] Kwon, H.-M., Paxson, A. T., Varanasi, K. K. & Patankar, N. A. Rapid deceleration-driven wetting transition during pendant drop deposition on superhydrophobic surfaces. *Phys. Rev. Lett.* **106**, 036102 (2011). URL `http://link.aps.org/doi/10.1103/PhysRevLett.106.036102`. 87, 88

[138] Deng, T. *et al.* Nonwetting of impinging droplets on textured surfaces. *Applied Physics Letters* **94**, 133109 (2009). URL `http://link.aip.org/link/?APL/94/133109/1`. 87, 88

[139] Wood, D. J. & Jones, S. Water-hammer charts for various types of valves. *Journal of the Hydraulics Division* **99**, 167–178 (1973). 87

[140] Engel, O. G. Waterdrop collisions with solid surfaces. *J. Res. NBS* **5**, 281–298 (1955). 87, 88

[141] Cook, S. S. Erosion by water-hammer. *Proceedings of the Royal Society of London. Series A* **119**, 481–488 (1928). 88

[142] Hyväluoma, J. & Timonen, J. Impalement transitions in droplets impacting microstructured superhydrophobic surfaces. *EPL (Europhysics Letters)* **83**, 64002 (2008). 89

[143] Hyväluoma, J. & Timonen, J. Impact states and energy dissipation in bouncing and non-bouncing droplets. *Journal of Statistical Mechanics: Theory and Experiment* **2009**, P06010 (2009). 89